

Investigating the Influence of DBD Plasma Actuators on Skin Friction: Application to Integral Boundary Layer Formulation

S.R. Bal

October 22nd, 2015



Investigating the Influence of DBD Plasma Actuators on Skin Friction: Application to Integral Boundary Layer Formulation

MASTER OF SCIENCE THESIS

For obtaining the degree of Master of Science in Engineering Wind Energy at Technical University of Denmark and in Aerospace Engineering at Delft University of Technology.

S.R. Bal

October 22nd, 2015

European Wind Energy Master - EWEM
DUWIND - Delft University of Technology
Risø - Denmark Technical University



Risø DTU



Copyright © S.R. Bal
All rights reserved.

EUROPEAN WIND ENERGY MASTER - EWEM
OF
ROTOR DESIGN

The undersigned hereby certify that they have read and recommend to the European Wind Energy Master - EWEM for acceptance a thesis entitled **“Investigating the Influence of DBD Plasma Actuators on Skin Friction: Application to Integral Boundary Layer Formulation”** by **S.R. Bal** in partial fulfillment of the requirements for the degree of **Master of Science**.

Dated: October 22nd, 2015

Head of department:

prof.dr. G.J.W. van Bussel
Delft University of Technology, the Netherlands

Supervisor:

ir. R. Balbino Dos Santos Pereira
Delft University of Technology, the Netherlands

Supervisor:

dr. ir. N. Ramos Garcia
Danish Technical University, Denmark

Reader:

dr. ir. B.W. van Oudheusden
Delft University of Technology, the Netherlands

Reader:

dr. M. Kotsonis
Delft University of Technology, the Netherlands

Summary

The main driver of developments in the wind energy sector is not the absolute maximization of energy capture, but the reduction of the Cost of Energy (CoE). More and more research is carried out to investigate control of the air flow to reduce fatigue loads, structural requirements, and apply novel control strategies to ultimately reduce this important CoE.

Plasma actuators have been the subject of an increasing amount of research in recent years in the field of Active Flow Control (AFC). Of particular interest to the present study is the alternating current Dielectric Barrier Discharge (DBD) plasma actuator, which is widely used due to the low mass, low power consumption, fast response time, absence of moving parts and large actuation bandwidth. Successful applications of the technique include postponement and control of flow separation, transition delay by Tollmien-Schlichting wave cancellation, stream-wise vortex generation and the control of dynamic stall on oscillating airfoils.

To fully take advantage of the potential performance increase DBD actuators can offer, its effect should be accounted for as early as possible in the aerodynamic design phase. Previous work at TU Delft incorporated the DBD plasma body force in the integral boundary layer formulations. In the light of discrepancies between the existing model and experimental observations, attention is focused on the skin friction.

An experimental campaign was designed and conducted at the open jet facility to acquire high resolution PIV of the turbulent boundary layer during various states of boundary layer development, for both actuated and non-actuated cases. The velocity fields were post-processed to obtain the variation in skin friction induced by the DBD plasma. Major conclusion from the observations is the fact that the increase in skin friction due to actuation occurs downstream of the actual plasma body force region, and extends for approximately 2.6 body force lengths. A semi-elliptical fit is employed to model the variation in skin friction due to DBD plasma actuation dC_f .

The steps to be taken to implement the dC_f in a numerical boundary layer solver are investigated. The work includes a first approach in Matlab, to pave the way for future

work to include the skin friction correction in rapid-analysis, viscous-inviscid panel codes based on integral boundary layer formulation such as Rfoil.

Contents

Summary	v
List of Figures	xiii
List of Tables	xv
1 Introduction	1
1.1 Project aim	2
1.2 Research questions	3
1.3 Approach	4
1.4 Document outline	4
I Theory	5
2 Dielectric barrier discharge plasma actuators	7
2.1 General overview	7
2.1.1 Working Principle	9
2.1.2 Benefits and Drawbacks	10
2.1.3 Applications	12
2.2 Influence of operational parameters	14
2.2.1 Dielectric material and thickness	15
2.2.2 AC frequency	16
2.2.3 Number of actuators and covered electrode width	16
2.2.4 Electrode gap	17
2.2.5 Effect of external flow	18
2.3 Current state-of-art Modeling of the DBD plasma actuator	19
2.3.1 First principle models	19

2.3.2	Space-time lumped-element circuit model	21
2.3.3	Experimentally derived force distributions	21
2.3.4	Potential flow panel method	24
2.3.5	Synthesis and need for plasma-specific closures	24
3	Integral Boundary Layer Formulation	25
3.1	General overview	25
3.1.1	History	25
3.1.2	Boundary layer flow features	26
3.2	Integral boundary layer equations	28
3.2.1	General flow equations	28
3.2.2	Boundary layer equations	29
3.2.3	Integral boundary layer equations	30
4	Plasma force term	37
4.1	Plasma force coefficients	37
4.1.1	Physical meaning	38
4.2	Plasma force field	38
4.2.1	Characteristics	39
4.2.2	Force field topology	39
4.3	Plasma force coefficients revisited	40
4.4	Energy Interaction Coefficient	41
4.5	Energy interaction coefficient results	43
II	Experimental campaign	45
5	Design of experiment	47
5.1	Resolution investigation required for PIV	47
5.2	Experimental test matrix	49
5.2.1	Front actuator	50
5.2.2	Back actuator	50
5.3	PIV Camera optics	50
6	Experimental setup	53
6.1	Flow facility	53
6.2	Model setup	53
6.3	Airfoil model	55
6.4	Plasma actuator	55
6.5	Particle Image Velocimetry setup	56
6.6	Processing	56

7	Experimental results	61
7.1	Post-processing methodology	61
7.1.1	Finding the wall	61
7.1.2	Shift to boundary layer frame of reference	63
7.1.3	Extracting representative skin friction coefficient	63
7.2	Data quality analysis	66
7.2.1	Angle of attack 0°	67
7.2.2	Angle of attack 7°	69
7.2.3	Angle of attack 10°	69
7.2.4	Angle of attack 13°	69
7.2.5	Conclusion	69
7.3	Discussion of selected datasets	71
III	Modelling and discussion	75
8	Plasma actuated skin friction coefficient variation	77
8.1	Characterization of experimental fit	77
8.1.1	Shape	77
8.1.2	Body force length	77
8.1.3	Modelling parameters	80
8.1.4	Check of spatial distribution	81
8.2	Trends for H , Re_θ and t_θ^p	82
8.3	A13 Cases: Asymptotic value analysis for large H	83
9	Towards numerical implementation	87
9.1	MATLAB integral boundary layer solver	87
9.2	Modifications to the solver	89
9.2.1	Longitudinal skin friction affected region coordinate	89
9.2.2	Normal skin friction affected region coordinate	90
9.2.3	Iteration over H	93
9.3	Outcome of data fit	94
9.3.1	Experimental case	94
10	Conclusions & Recommendations	99
10.1	Conclusions	99
10.2	Recommendations	100

List of Figures

1.1	Cumulative wind power installations in the European Union [GW] [1]. . .	1
1.2	Evolution of rotor size and rated power from 1980 to future projections [1].	2
2.1	Geometrical configuration of DBD actuator describing dielectric barrier thickness t , horizontal gap g and respectively exposed and covered electrode length $l_{e,exp}$, $l_{e,cov}$	9
2.2	Discharge current and voltage with encapsulated grounded electrode over time [2].	9
2.3	Geometrical configuration of DBD actuator [3].	10
2.4	Discharge current and voltage with encapsulated grounded electrode over time [3].	11
2.5	Instantaneous electrical power consumption versus time [4].	12
2.6	Principle of active Tollmien-Schlichting wave cancellation using DBD plasma actuator [5].	13
2.7	Wind turbine airfoil sections used for experimental work of Nelson <i>et al</i> [6].	14
2.8	Measured thrust per unit span versus rms applied voltage for various dielectric materials [7].	15
2.9	Saturation thrust versus dielectric constant for various barrier materials [7].	16
2.10	Actuator thrust versus applied peak-to-peak voltage for various frequencies and waveforms [7].	17
2.11	Maximum induced velocity versus electrode gap length [3].	18
2.12	Measured force difference between actuator on and off setting [8].	19
2.13	The electric circuit model for N parallel networks representing a single DBD plasma actuator [9].	21
2.14	Spatial body force distribution using the reduce (top) and gradient method (bottom) for 12 kV _{pp} and 2 kHz [10].	22
2.15	The velocity field constructed from PIV measurements which is the basis for the subsequent analysis of Maden <i>et al</i> [11].	23

3.1	Development of the boundary layer on a flat plate [12].	26
3.2	Transition of the boundary layer on a flat plate [13].	27
3.3	Visualization of the displacement thickness δ^* . [14].	31
3.4	Normalized velocity $U = U_{local}/U_e$ versus displacement from the wall n for displacement thickness δ^* , momentum thickness θ and kinetic energy thickness θ^* [15].	32
3.5	Normalized velocity profile versus shape factor H [16].	33
4.1	Slice of the numerical C_{EI} closure data set [17]	42
4.2	Influence of Plasma Force Field Thickness [17].	43
4.3	Energy Interaction Coefficient for numerical and experimental results . . .	44
4.4	Evolution of the integral boundary layer for plasma actuator at 0.65 x/c at $U_\infty = 20m/s$ and $\alpha = 7^\circ$	44
5.1	Flow regions in the turbulent boundary layer.	48
5.2	The y^+ distance per captured data point over angle of attack, for various free stream flow velocities and actuator locations.	49
5.3	Range of experimental parameters for front and back actuator regions. . .	51
5.4	Object distance d_o and imaging distance d_i for the CCD camera setup. . .	51
6.1	Exploded view of the dedicated support structure for the present experimental campaign showing splitter plate, airfoil model, circular Plexiglas insert, table and support structure.	54
6.2	Airfoil section of the experimental model with two inserts for plasma actuation around $\frac{x}{c} = 0.25$ and $\frac{x}{c} = 0.65$	55
6.3	Average velocity fields $V_{x,avg}$ and $V_{y,avg}$ for the benchmark run of 450 image pairs with the six points of evaluation marked by '*'.	57
6.4	Offset in local average velocity for $V_{x,avg}$ and $V_{y,avg}$ over accumulating amount of image pairs.	57
6.5	Local average velocity value for $V_{x,avg}$ and $V_{y,avg}$ over accumulating amount of image pairs.	58
6.6	Airfoil model and set-up of the experimental campaign.	59
7.1	Average velocity fields of V_x and V_y in PIV frame of reference (quiver resolution is reduced for illustration purposes).	62
7.2	Standard deviation of V_y with the experimentally found edge.	63
7.3	Airfoil surface as found through experiment (red) and airfoil coordinates.	64
7.4	Average velocity fields of V_x and V_y in the boundary layer frame of reference (quiver resolution is reduced for illustration purposes).	65
7.5	Comparison between the displacement thickness δ^* and momentum thickness θ for actuator off and on.	66
7.6	C_f -ratio of experimental over numerical X/Rfoil value (left) and velocity profile (right) for A0U10 OFF at $x = 9$ mm.	67

7.7	Relative variation in skin friction between plasma on and off dC_f [%] with smoothing spline for A0U10.	68
7.8	Difference in y-coordinate of the location where skin friction is extracted between plasma on and off case for A0U10.	68
7.9	Average velocity fields for A0U16ON and A0U16OFF cases.	70
7.10	Uncertainty in the boundary layer velocity profile for A13 cases.	71
7.11	Relative variation in skin friction coefficient between plasma on and off case for A0U10	72
7.12	Relative variation in skin friction coefficient between plasma on and off case for A7U16	73
7.13	Relative variation in skin friction coefficient between plasma on and off case for A7U22	73
8.1	Relative variation in skin friction coefficient between plasma on and off case and proposed semi-elliptical fit for A0U10.	78
8.2	Relative variation in skin friction coefficient between plasma on and off case and proposed semi-elliptical fit for A7U16.	78
8.3	Relative variation in skin friction coefficient between plasma on and off case and proposed semi-elliptical fit for A7U22	79
8.4	Maximum increase in velocity due to the plasma actuation at every position over the measurement domain for A0U10.	79
8.5	Division of semi-ellipse in quarters used as check on the spatial distribution data-fit.	82
8.6	Relative variation in the momentum and displacement thickness between the plasma ON and OFF case for A0U10.	83
8.7	Trend for semi-major axis b over H , Re_θ and t_θ^p	84
8.8	Trend for mean dC_f in percent over H , Re_θ and t_θ^p	84
8.9	Trend for starting point of the ellipse over H , Re_θ and t_θ^p	85
8.10	Shape factor H versus momentum scaled Reynolds number Re_θ for accepted experimental data sets.	85
8.11	Smoothed relative skin friction coefficient variations for the A13 cases. . .	86
9.1	Dimensions of the weighting function of dC_f perturbed region.	90
9.2	Detailed view of skin friction coefficient C_f versus shape factor H for both the actuated (\circ) and non-actuated ($*$) cases. The dotted lines show the skin friction $C_f(H, Re_\theta)$ as obtained by the X/Rfoil closure for each of the three flow cases.	91
9.3	The standard Swafford-derived C_f , composite $C_{f,plasma}$ and separate left, middle and right regime components for $Re_\theta = 3653$	93
9.4	The offset between $C_{f,plasma}$ and $C_{f,S}$ or equivalently the normal coordinate of the dC_f shadow region	94
9.5	Comparison between computed and experimental skin friction coefficients for the case of A7U16.	96
9.6	Comparison between computed and experimental displacement and momentum thickness for the case of A7U16.	97

List of Tables

7.1	Mean value of skin friction variation	71
8.1	Mean value of skin friction variation	80
8.2	Summary of characteristics of semi-ellipse models for various cases.	81
8.3	Check on semi-elliptical fit for modelling dC_f in space.	81
8.4	Check on semi-elliptical fit for modelling dC_f in space.	82
8.5	Skin friction coefficients of the A13 OFF cases	86

Chapter 1

Introduction

The main driver of developments in the wind energy sector is not the absolute maximization of energy capture, but the reduction of the cost of energy. This economical reality is important for the competitiveness against non-renewable energy sources. The European Union has set a binding target in the 2009 Renewables Directive to achieve 20% final energy consumption coming from renewable sources by 2020 [18]. By tripling its capacity over the past 10 years, wind energy has become the second largest renewable energy source, after hydro-power. The European Wind Energy Association (EWEA) reports a 9.8% increase in total installed capacity in 2014, as can be seen in Figure 1.1 [1]. The EWEA estimates with the current growth trend that wind energy could deliver between 14% and 17% of the EU's electricity by 2020. The increased capacity is not only due to the fact that more turbines are set up, the capacity per turbine increases as well.

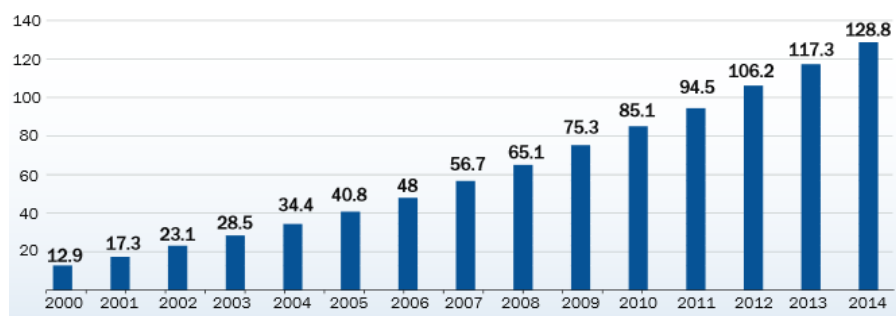


Figure 1.1: Cumulative wind power installations in the European Union [GW] [1].

In the last few decades, the size of wind turbines has kept on increasing (as shown in Figure 1.2). Increasing the rotor radius R increases the area over which energy can be harvested. Power scales by a factor R^2 . However, aerodynamic moments increase by a factor of R^3 , together with weight and fatigue loads. One of the suggested technical developments to ensure that the cost of energy does not increase despite the larger energy capture, is to incorporate advanced control mechanisms should in the design.

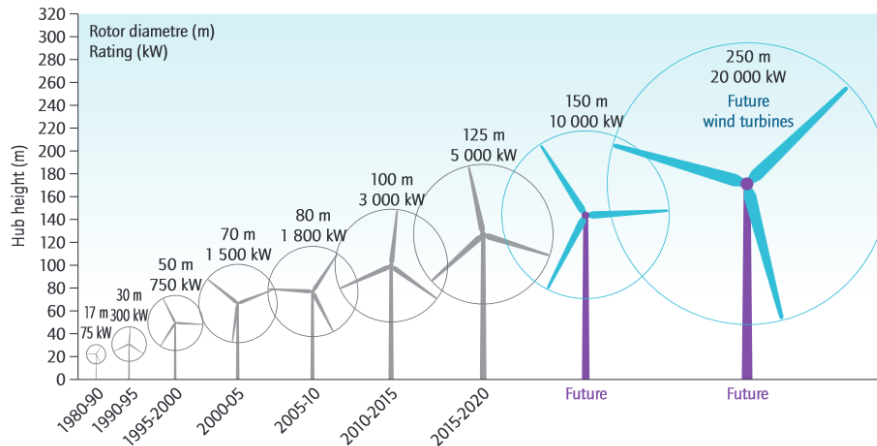


Figure 1.2: Evolution of rotor size and rated power from 1980 to future projections [1].

Two main types of control can be distinguished. Turbines with passive control does not need external power input to do this. Early wind turbines were passively controlled with fixed-pitch rotor blades. With increasing wind speeds, the angle of attack increases. Above certain wind speeds, stalling of the blade caps off the power production. The range of operating conditions is however limited using this control strategy. Another example of passive control is the yaw adjustments on downwind wind turbines, which is regulated by the air flow itself.

The second type of control is active control. This does require an external power supply. In the past, mechanical devices with moving parts were applied to wind turbine blades to increase performance. However, the added weight and complexity reduce reliability. The current standard of wind turbines employs rotors with variable rotor speed and blade pitch control. These mechanisms have proven their merit, but wear out components requiring maintenance. Those techniques are a from of turbine control which manipulate the loads felt by the turbine. More and more research is carried out to investigate control of the airflow itself. Active Flow Control (AFC) systems are applied amongst others as a means of transition/separation control, to aid or replace the pitch mechanism, to reduce noise and alleviate fatigue loads. Plasma actuators, as described e.g. in Moreau’s review [4], have been the subject of an increasing amount of research in recent years in the field of Active Flow Control (AFC). Of particular interest for this thesis is the alternating current Dielectric Barrier Discharge (DBD) plasma actuator.

1.1 Project aim

The alternating current Dielectric Barrier Discharge plasma actuator is widely used due to the low mass, low power consumption, fast response time, absence of moving parts and large actuation bandwidth. Successful applications of the technique include postponement and control of flow separation [19], transition delay by Tollmien-Schlichting wave

cancellation [5] [20], stream-wise vortex generation [21] and the control of dynamic stall on oscillating airfoils [19].

Nelson *et al.* [6] demonstrated the capabilities of plasma actuators controlling the lift over a modified S822 wind turbine airfoil with flow separation ramps near the trailing edge. Although the geometric alterations were not optimized in any way, through actuation the loss in lift compared to the base airfoil could be recovered entirely in the range of $-3^\circ < \alpha < 3^\circ$. A difference in lift coefficient ΔC_l of 0.4 was found between the cases with and without actuation in the specified range, highlighting the potential benefits optimally designed airfoil sections including plasma actuators could have.

The first field test of a plasma aerodynamic controlled wind turbine of 30 kW was conducted at Mie University, Japan in 2012 [22]. Measuring in natural, turbulent wind conditions presents inherent difficulties, since the flow condition cannot be replicated exactly for actuator on and off cases. However, a significant enhancement of torque and power generation was found when the plasma actuators controlling leading edge separation were activated. The improvement persisted even in very turbulent conditions. A follow-up study confirmed the potential of DBD plasma actuators on a commercial scale wind turbine. A 1.75 MW Vestas V-66 equipped with plasma actuators showed an average power enhancement of 14% during the test period. Even for high Reynolds number flow conditions, leading edge separation control by plasma actuators proves to be highly effective.

In the light of the gains to be made by dedicated airfoil design, and the promising results of real-life application of this type of actuator on commercial scale wind turbines, the need for plasma-dedicated airfoil profiles emerges. To fully take advantage of the potential performance increase DBD actuators can offer, it should be incorporated as early as possible in the aerodynamic design phase.

A robust actuator model is required to cope with the wide range in dimensional, geometrical and electrical properties [7] [3]. Actuator model connected with flow solver easily, in a way not prohibitive of design iterations.

For airfoil design optimization purposes, conventional CFD codes and RANS solvers are computationally expensive and time-consuming. For rapid analysis with low computational cost while retaining reasonable accuracy, viscous-inviscid panel codes as found in [23], [24] and [25] remain an attractive option. In a previous study, the DBD plasma actuator body force was incorporated in the integral boundary layer formulation [26]. Although this type of modelling shows promising results, the skin friction C_f closure relation remains unaffected by plasma actuation. The present study investigates the effect DBD plasma actuation has on the skin friction.

1.2 Research questions

Gaining insight in the influence of DBD plasma actuators on the variation of skin friction is a step closer to a rapid analysis tool able to represent plasma actuation accurately to ultimately design airfoils tailored to the active flow control. The following research questions are posed in this thesis report:

- What is the effect on skin friction of DBD plasma actuators in turbulent boundary layer and how can it experimentally be obtained?
- What parameters of influence can be identified for the variation of skin friction, and how do they behave for various boundary layer states?
- How can this effect be modelled in computationally inexpensive methods to help in airfoil design?

1.3 Approach

To fully comprehend the challenges that lie ahead, an extensive review is presented of both the DBD plasma actuator and integral boundary layer formulation. The skin friction coefficient is measured experimentally through post-processing velocity field acquired with particle image velocimetry. Various settings of angle of attack of the airfoil model and flow speeds ensure distinct states of the boundary layer development are measured. The dataset is then used to describe a phenomenological model of the spatial distribution of skin friction variation over the airfoil. Guidelines to use this approach in a flow solver based on integral boundary layer equations are then set out.

1.4 Document outline

The thesis is divided into three main parts. The first part elaborates on the theory on which the thesis is founded and elaborates a bit more in detail about the dielectric barrier discharge plasma actuators (Chapter 2) and the integral boundary layer formulation (Chapter 3). The incorporation of the DBD plasma body force term is shown in Chapter 4. Part II deals with the design, practical setup and results of the experimental campaign in Chapter 5, Chapter 6 and Chapter 7 respectively. The third part comprises of Chapter 8, explaining the phenomenological spatial distribution of the skin friction variation due to actuation, and Chapter 9 where an outlook towards numerical implementation is presented. Conclusions about the project and recommendations for future work are formulated in Chapter 10.

Part I

Theory

Dielectric barrier discharge plasma actuators

2.1 General overview

The interest in active flow control in general is relatively new. The by now classical book of Gad-El-Hak [27] on all types of flow control was published in 2000. A few years later, in 2002, The American Institute of Aeronautics and Astronautics (AIAA) held its first conference dedicated to the subject. Generally speaking, all active flow control systems wish to manipulate the flow to bring about a desired effect. Three main phenomena which can be modified to wield the airflow as desired are the transition from laminar to turbulent state, the detachment of the flow and the turbulence level.

Mechanical devices might be effective in this field, but can add complexity, add weight, require relatively large amount of volume and can influence the aero-elastic response with noise and vibration. Furthermore, moving parts will wear and could break down, or require additional maintenance. Plasma actuators do not suffer from most of these drawbacks which explains why they seem very promising. Moreau [4] has compiled an excellent review of publications on the topic. He defines a plasma actuator as a device which *'consists of using the discharge-induced electric wind within the boundary layer to modify its properties and then actively manipulate the airflow'*. The airflow very close to the wall is accelerated tangentially due to the electric wind and modifies the velocity profile in the boundary layer.

The formation of plasma discharge is based on cascade ionization [4]. A (strong) electric field is formed due to the application of the high voltage on the two electrodes. The free electrons which are formed at the high voltage point are accelerated towards the anode and bring about an electron avalanche. Free electrons collide with neutral molecules which ionize upon impact, leading to more free charged particles drifting. An example, where

A is a neutral particle and A^+ is its positive ion:



The discharge current is the compounding group of electrons drifting from cathode to anode. Its behavior varies according to the applied voltage regime. Electric wind is caused by the collisions between the drifting ions and the neutral particles. Typical discharges used in flow control applications can be excited with either AC or DC voltages of a few to several tens of kV, with frequencies in the range of 50 Hz to 50 kHz. The electrical current can vary between a few μ A to a few mA.

Historically, the first type of actuators used for airflow control with electrical discharges were DC surface corona discharge actuators. Depending on the voltage that is applied, five different corona discharge regimes can be observed. These are, in order of ascending excitation voltage:

- The *spot* regime occurs at the lowest voltage settings and all the discharge is concentrated on some visible spots on the wire. No electric wind can be discerned.
- The *streamer* discharge is characterized by a thin sheet of blue ionized air between the electrodes.
- Typical corona is observed in the *glow* discharge regime. It requires higher voltage/gap ratios than the *streamer* regimes and only a set of luminescent spots around the electrodes are present. It is highly stable and high currents can be formed.
- Increasing the voltage/gap ratio even more, the current becomes concentrated in strands in the *filamentary* regime.
- For even higher voltage/gap ratios, sparks can appear and the discharge becomes highly unstable and problematic to control.

One of the main drawbacks of corona discharge actuators is the fact that the maximum velocity which can be achieved is limited by the glow-to-arc transition. Amongst other parameters, it was noted that the electrical properties highly depend on the dielectric wall surface [28]. Optimizing the geometrical configuration is crucial, and when the dielectric material is placed in between the electrodes, the system is termed a Dielectric Barrier Discharge (DBD) plasma actuator. This arrangement prevents the corona-to-spark transition and the plasma in the electrode gap is produced by a succession of randomly distributed micro-discharges in the stable glow regime.

Although surface corona and dielectric barrier discharge actuators are the most used, other non-thermal discharge actuators also exist. An overview can be found in the review paper of Moreau . In conclusion, the time-averaged velocity which is achievable with plasma actuators is in the order of a few m/s, and reaches its maximum at approximately 0.5 mm from the wall (velocity \approx 8 m/s). For every watt of electrical power that is fed to the actuator, a body force of around 0.15 mN is created by the ion motion [4].

2.1.1 Working Principle

The typical configuration of a DBD plasma actuator is shown in Figure 2.1. One plane electrode is mounted flush on each side of the dielectric material. High voltage is usually applied on the electrode which is exposed to the air and the other one is grounded. When the AC high voltage excitation is applied, a plasma region will form on both sides of the dielectric. The electric wind below the barrier is usually unwanted. To prevent it from forming, the grounded electric is encapsulated in a dielectric as well. The parameters shown in the figure, the exposed electrode length $l_{e,exp}$, the covered electrode length $l_{e,cov}$, the horizontal gap g , the dielectric thickness t and dielectric material, have an effect on the plasma formation.

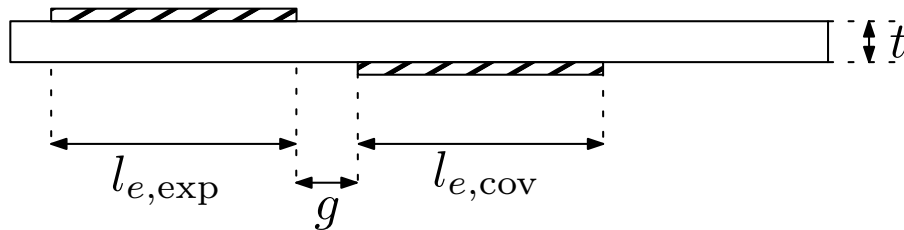


Figure 2.1: Geometrical configuration of DBD actuator describing dielectric barrier thickness t , horizontal gap g and respectively exposed and covered electrode length $l_{e,exp}$, $l_{e,cov}$

The image on the left of Figure 2.2 (from [2]) depicts the situation where a negative value of high voltage is applied to the exposed electrode and free electrons are released. They accelerate towards the electrode on the other side of the dielectric barrier, but as the electrons cannot pass through they accumulate on the surface. The build-up of charges opposes the potential and when the applied voltage is not increased, the plasma generation stops. As the barrier avoids leakage that would result in arc formation, the DBD actuator has desirable self-limiting behaviour. When the potential is reversed, Enloe *et al* [2] state that the charge transfer is limited to the electrons collected on the dielectric material surface. As the particles do not leave the dielectric at the same rate as they left the cathode of the previous half-cycle, less plasma volume is generated. Although the direction of charge transfer varies during the two half-cycles, the body force has the same direction at all times [7].

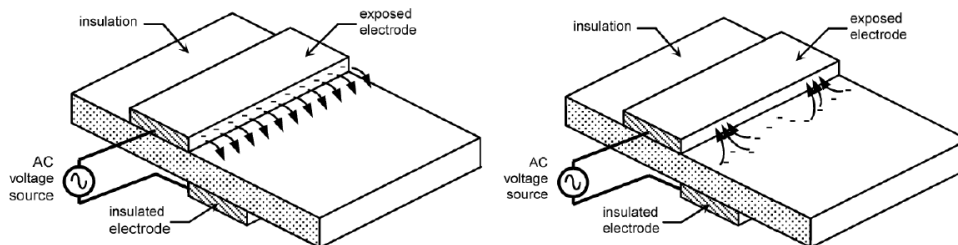


Figure 2.2: Discharge current and voltage with encapsulated grounded electrode over time [2].

Forte *et al* were able to perform simultaneous measurements of the voltage, current and velocity components during DBD actuation [3]. It can be seen that the positive and

negative half-cycles are not (anti-)symmetric. For the specific parameters of Forte's experiment, a horizontal velocity of 3.6 m/s was induced for the negative half-cycle and 'only' 2.4 m/s for the positive stroke. At the relatively low frequency of 700 Hz used, the induced flow seems pulsed at the same frequency as the high voltage. An induced vertical velocity appears during the positive half-cycle, whilst the other half-cycle does not affect this component.

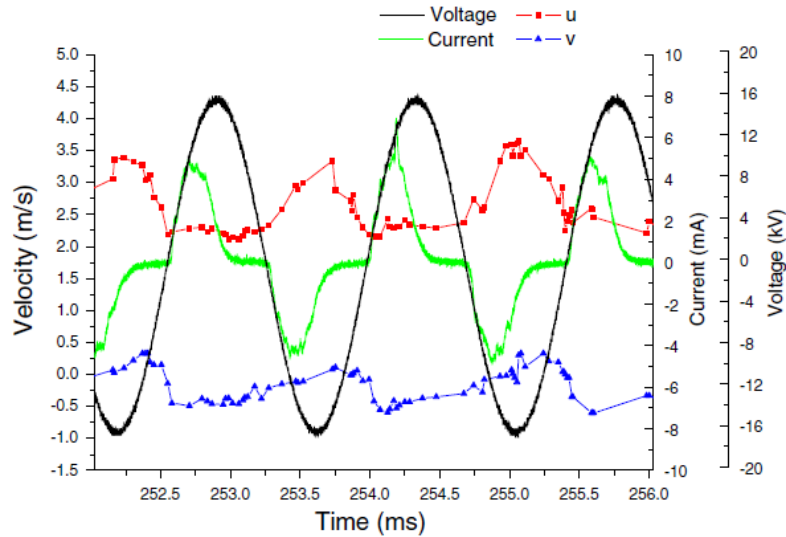


Figure 2.3: Geometrical configuration of DBD actuator [3].

When looking in more detail to the evolution of discharge current with excitation voltage in Figure 2.4, the differences between both half-cycle can be discerned. The plasma is more homogeneous over the negative forward stroke. During the positive backward stroke, the plasma consists of a rapid succession of micro-discharges.

2.1.2 Benefits and Drawbacks

Some advantages and disadvantages have already emerged in the preceding discussion, but these are mentioned once more explicitly. Although the technique shows great promise, it also exhibits several drawbacks which are explained in the following section.

Advantages

- One of the main advantages of the DBD plasma actuator technique is, the absence of moving parts. This enhances reliability and maintenance greatly.
- No middle agent between the conversion of electric energy into kinetic energy is required, which removes losses in this intermediate step.
- Following from the previous point, the response time is very short. This enables high frequency real-time flow control. The DBD actuators have a wide bandwidth and can operate over a wide range of actuation frequencies.

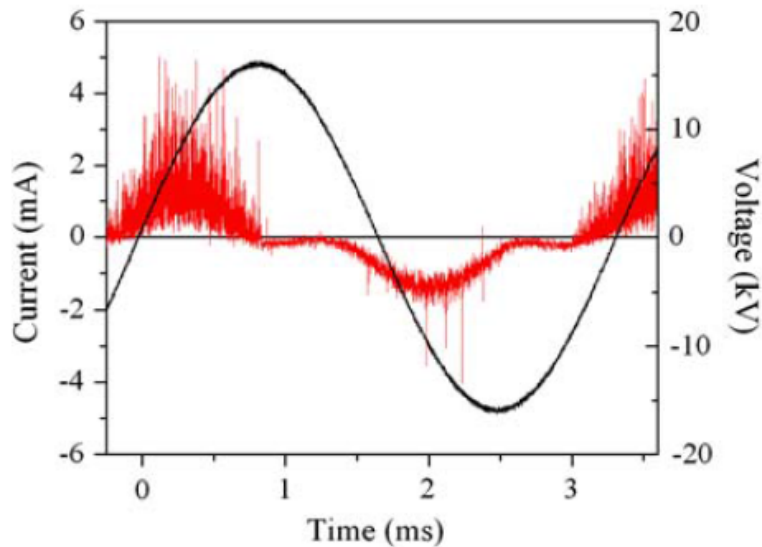


Figure 2.4: Discharge current and voltage with encapsulated grounded electrode over time [3].

- The electrodes and barrier are thin, the complete actuator has a thickness in the order of millimetres [7]. Because they are thin, integration with existing structures should not prove to be difficult. The added weight of the actuator is negligible, and does not incur additional aero-elastic issues due to vibration. No slots or cavities are required which could compromise structural integrity.
- Typically, the DBD plasma actuators have a relatively low power consumption. For continuous operation, in the order of 6 ~ 120 W per linear meter of actuator span is required [19].

Disadvantages

- The widespread combination of polyimide (Kapton) tape as dielectric with copper tape electrodes for DBD actuators exhibits some drawbacks. Because Kapton is a polymer with poor resistance to plasma, the top layer degrades and exposes the adhesive underneath after significant use of the actuator [29]. Increasing the voltage amplitude increases the amount of plasma, but also leads to larger heating of the dielectric material and faster degradation. This in turn reduces the performance due to unstable discharges with electric arcing. The edges of the exposed electrode degrade first. Due to the degradation during use, also the performance varies throughout the actuator's lifetime.
- When installing the DBD actuator, particular attention should be paid to the placement of the exposed electrode. Smoothness of the copper tape is highly desired, as sharp edges or wrinkles can cause a local increase in charge concentration, which in turn can lead to arcing [29]. Manual application is therefore restricted to simple geometries.

- The surface discharges may lead to a modification of the properties of the fluid, such as the density or the viscosity. However, it seems that this effect is negligible for quasi-incompressible flows with flow speeds below 30 m/s [4].
- Although the electric energy is transferred directly into kinetic energy, the conversion efficiency is very low. [30] reports a conversion of actuator power into fluid mechanical power of only a few percent. A large fraction of the input energy is lost in thermal radiation, chemical reaction and emissions such as sound and light.
- Although the time-averaged power consumption itself is relatively low, when taking a look at the instantaneous electrical power over time in Figure 2.5, large fluctuations can be noted. These peaks reach up to 350 W, whilst the time-averaged power only amounts to 16 W [4].

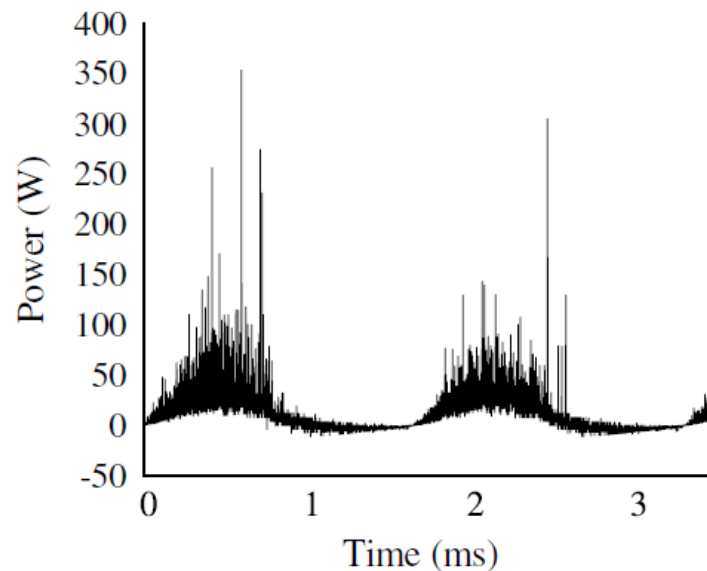


Figure 2.5: Instantaneous electrical power consumption versus time [4].

- One of the original applications of dielectric barrier discharge is to produce ozone. The free-oxygen created by the plasma is abrasive for the dielectric material and will eventually degrade the barrier. This imposes limits to the materials which can be used and can drastically reduce operational life [19].

2.1.3 Applications

A brief overview of the various applications of DBD plasma actuators is given in this section.

The postponement of leading edge separation control was investigated by Corke and Post [19]. Experiments were performed on a NACA 0015. The plasma actuator was placed flush with the surface on the leading edge, with the junction between the electrodes at the exact leading edge. The asymmetric arrangement results in the fact that for any positive angle

of attack, the exposed electrode is on the pressure side of the airfoil, whilst the covered electrode is on the suction side. A favourable velocity increment in the downstream direction of the suction side is generated in this way. During steady operation, the angle of attack at which stall occurs can be delayed from 14° to 18° . During unsteady operation, it can even be increased to 22° . This was achieved using a 10% duty cycle D_c :

$$D_c = 100\% \times \frac{t_{\text{on}}}{t_{\text{on}} + t_{\text{off}}} \quad (2.2)$$

Introduction of periodic disturbances can delay separation, and a duty cycle of 10% as used by Corke also means a power saving of 90% in comparison with steady actuation. Experiments regarding control separation were also performed on gas turbine blades at low Reynolds numbers [19]. The plasma actuator was placed at a chord position of $x/C = 0.67$. Without actuation, separation of the flow was observed from $x/C = 0.72$ onwards. Steady actuation places the point of separation further downstream at $x/C = 0.85$, whilst the flow remains fully attached for periodic excitation.

Another application where the actuator is not engaged continuously is for transition delay by wave cancellation. The skin friction increases with an order of magnitude from laminar to turbulent flow, which exemplifies the gains to be made. A maximum induced velocity is not the main objective in this case, but rather the attainable responsiveness of the flow control system. DBD plasma actuators are ideally suited for this purpose as they are non-intrusive and can react nearly instantaneously. The principle relies on the cancellation of the Tollmien-Schlichting waves which dominate the transition process for small sweep angles. The growth of these instabilities is impeded by artificially imposing a counter-wave. The principle is shown in Figure 2.6 and described by Kotsonis *et al* [5].

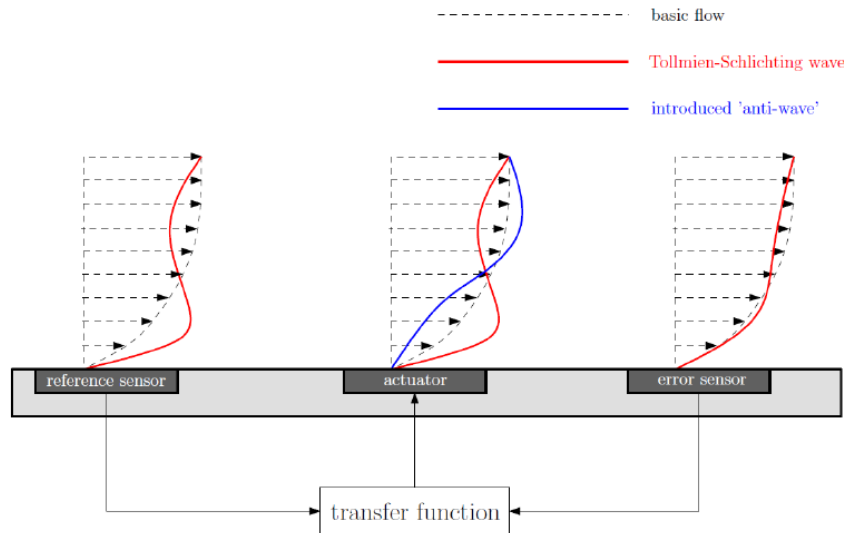


Figure 2.6: Principle of active Tollmien-Schlichting wave cancellation using DBD plasma actuator [5].

A closed-loop system with reference and error sensors, actuators and processors is necessary. The reference sensor picks up the instability and a transfer function processes the

required phase and frequency of the wave to cancel out the laminar boundary layer irregularity. The error sensor provides feedback to the processor about the effective damping. Due to the inherent unstable nature of boundary layers, a complete elimination of the waves is not possible, but studies such as [20] show the value of this application.

To improve the performance of wind turbines, Nelson *et al* [6] also used integrated sensor-actuator-controller modules on the blades. The flow field can be modified by the actuators as if the geometry would be altered, which is called virtual shaping by the authors. The ability to apply flow control in unsteady wind conditions is appealing in terms of load control. Two airfoils were investigated, the S827 and S822 profile shown in Figure 2.7.

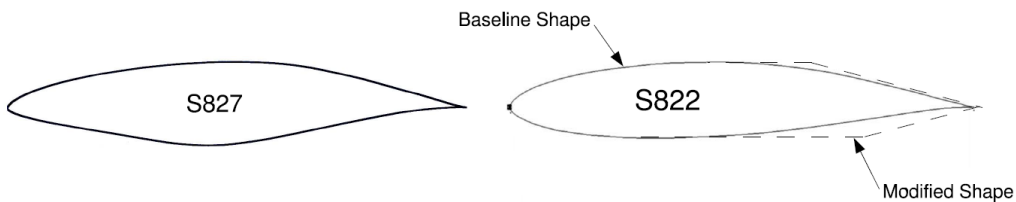


Figure 2.7: Wind turbine airfoil sections used for experimental work of Nelson *et al* [6].

The first of these was used for circulation control and practice the virtual shaping. The effect on the boundary layer with steady operation of an actuator placed at $x/C = 0.78$ proved to be equivalent to an increase in camber of the airfoil. An increase in lift coefficient dC_L of 0.08 was achieved.

The S822 profile was modified by adding two separation ramps. The thought behind this was to willingly induce flow separation, that could then be controlled by plasma actuators. It should be noted that the modifications to the baseline shape were not optimized in any way. The modified shape produced less lift than the baseline shape, but the loss in lift could be recovered entirely by the application of the actuators with a 12.5% duty cycle. In the range of $-3^\circ < \alpha < 3^\circ$, the gain in dC_L was a considerably 0.4. The potential benefits in control for optimally designed wind turbine airfoil sections with plasma actuators therefore seem very promising.

Besides these cases, numerous other examples can be found in literatures, such as the control of dynamic stall on oscillating airfoils [19], streamwise vortex generation [21] and noise control due to vortex shedding on a cylinder [4].

2.2 Influence of operational parameters

To see how the geometrical and electrical characteristics of a DBD plasma actuator influence the body force, various researchers have performed parametric studies. To acquire insight in the effects of these parameters, the study conducted by Thomas *et al* is considered [7]. The main goal of this investigation was to improve and optimize the actuator's

performance for flow control applications at high Reynolds numbers. The conclusions of the study are presented below. The induced thrust was used as the metric to assess the performance of the actuator.

2.2.1 Dielectric material and thickness

A baseline excitation voltage of $17 \text{ kV}_{\text{pp}}$ was used to compare actuators with various dielectric materials and thicknesses. A barrier which is often used for DBD plasmas is 0.15 mm thick Kapton polyimide tape. Kapton has a dielectric constant $\epsilon = 3.9$. The maximum measurable thrust per unit span was measured to be around 0.022 N/m . The other dielectrics which were tested are quartz ($\epsilon = 4.3$), Teflon ($\epsilon = 2.0$), Delrin ($\epsilon = 3.7$), and Macor ceramic ($\epsilon = 6.0$). The thrust curves for actuators with these materials is shown in Figure 2.8.

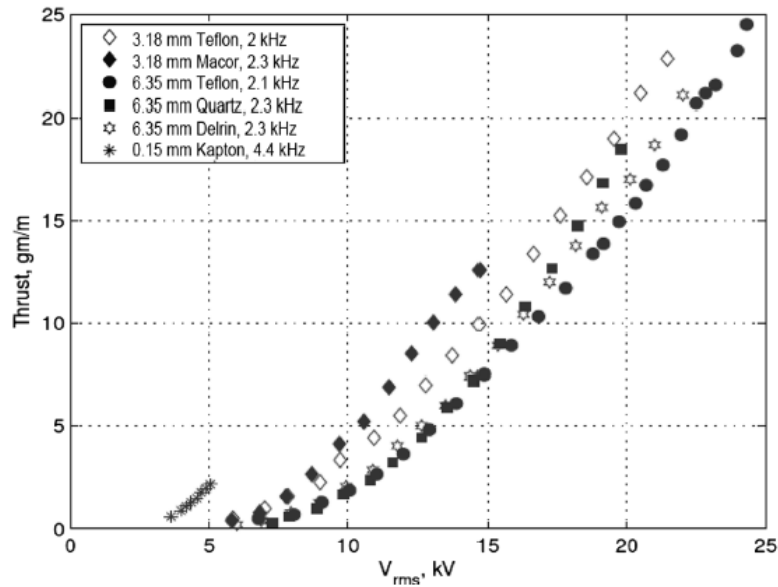


Figure 2.8: Measured thrust per unit span versus rms applied voltage for various dielectric materials [7].

The frequency differs slightly between the specimen, since it was optimized for the given actuator system. When comparing the maximum of the thick Teflon barrier with the standard Kapton, a difference of almost an order of magnitude is noted. The lower dielectric constant of Kapton means that the barrier has less effective capacitance, which reduces the local concentration of field lines. This reduction in current density allows for higher voltages to be applied, without the formation of streamers. The saturation thrust versus dielectric constant is plotted out in Figure 2.9 for the tested materials (excluding Kapton).

When streamers are formed, increasing the power will not yield a larger body force. The additional energy is dissipated and the actuator is called saturated. Comparing the 3.18 mm thick Teflon results for the barrier with a thickness of 6.35 mm , it can be seen that a larger body force can be achieved for the latter. A thicker barrier also contributes to a reduction of current density, allowing for a higher excitation voltage.

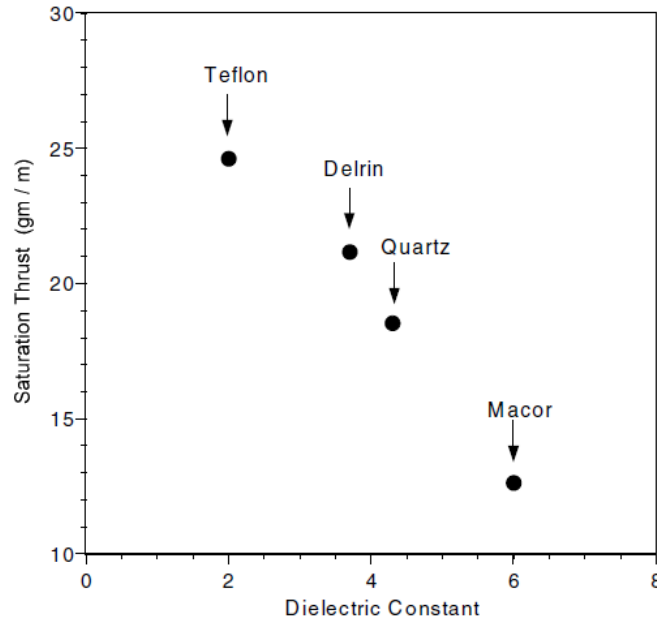


Figure 2.9: Saturation thrust versus dielectric constant for various barrier materials [7].

2.2.2 AC frequency

The investigate the influence of a variation in the frequency of the AC voltage excitation, an actuator with a 6.35 mm thick quartz dielectric barrier was tested. Sinusoidal waves with varied frequencies were applied and the achievable thrust per span and peak-to-peak voltage without streamer-transition is shown in Figure 2.10. A ramp or positive sawtooth waveform is also tested for the 2 kHz case. The achievable maximum thrust is almost double that of its sine wave counterpart. The positive sawtooth prolongs the forward stroke of the actuation cycle, where electrons are emitted from the exposed electrode [2]. When looking at Figure 2.10, it is immediately clear that an actuator operating at a lower frequency can achieve a higher maximum saturation thrust. However, if (for this case) a thrust per span of 0.06 N/m is desired, an actuator performing at 4 kHz requires 10 kV peak-to-peak less than one operating at 1 kHz. This demonstrates the trade-off to be made.

2.2.3 Number of actuators and covered electrode width

Fig 4 shows the measured thrust per unit span versus applied rms voltage for single, double and triple actuator configurations. As could be expected, more actuators produce a higher body force, but the total thrust is not simply the sum of the separate components. From the experiments, the ratios which were found are as follows:

$$\frac{T_{\text{double}}}{T_{\text{single}}} > 1.5 \quad , \quad \frac{T_{\text{triple}}}{T_{\text{single}}} > 2 \quad (2.3)$$

An explanation is sought in the direction of the interaction of the electric fields of each actuator with its surrounding. The ideal placement of the actuators relative to each other

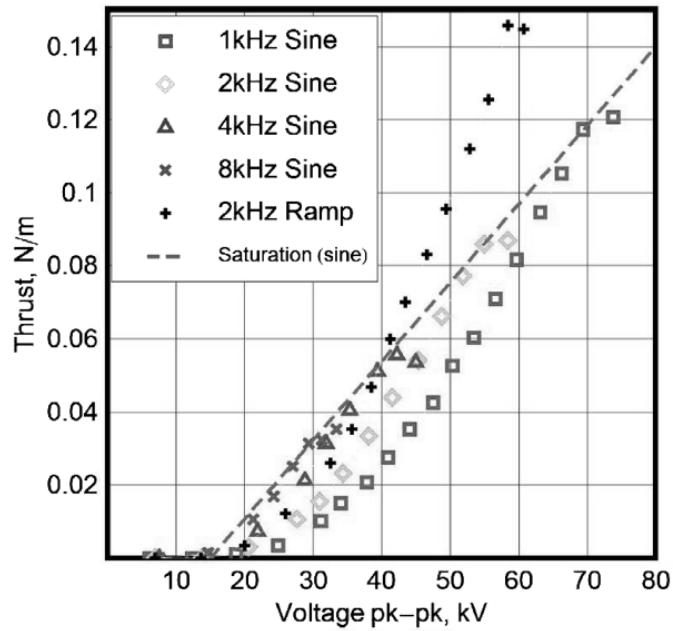


Figure 2.10: Actuator thrust versus applied peak-to-peak voltage for various frequencies and waveforms [7].

remains subject for further study. PIV measurements have shown that a substantial thickening of the wall jet occurs when more actuators are added in series. The same figure also confirms that increasing the length of the covered electrode increases the maximum achievable thrust. The width of the covered electrode should be large enough not to limit the formation of the plasma sheet at the highest applied voltages. If the width of the electrode exceeds the maximum spatial extent of the plasma region, no additional thrust is produced.

2.2.4 Electrode gap

The geometric optimization study performed by Forte *et al* also varied the horizontal gap between the electrodes. The main objective of Forte's study was to increase the induced velocity. For the experiment, an actuator with a 2 mm thick PMMA barrier with two identical 5 mm wide electrodes is used and 20 kV is applied at a frequency of 700 Hz. The resulting induced velocity versus electrode gap is shown in Figure 2.11. The optimal value found in this study is around 5 mm. After that, the induced velocity drops off quickly, as the electric field decreases when the dielectric thickness increases between the electrodes (at the same voltage setting). If the gap length has a negative value, i.e. the electrodes overlap, it is conjectured that two ionic winds with opposite directions are produced. These counteract each other, leading to a lower induced velocity than in the case of a positive gap.

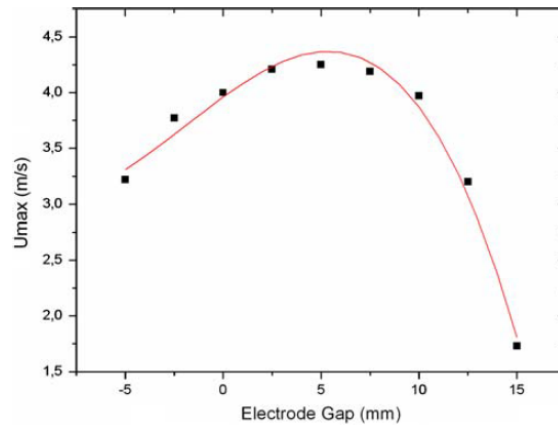


Figure 2.11: Maximum induced velocity versus electrode gap length [3].

2.2.5 Effect of external flow

Most studies which have focused on the performance of DBD actuators, have been performed in quiescent conditions. In the absence of external flow, the "pure" performance of the actuator is evaluated. Most plasma body force models assume decoupled relations between the flow field and the body force. The experimental study by Pereira *et al* [8] investigates the cross-talk effects between the actuator and the external flow. When the external flow reaches velocities in the order of $\mathcal{O}(100\text{m/s})$, the drift velocity of the charged particles becomes comparable to the convective velocity of the neutral air. Intuitively, the independence of the fluid and plasma physics becomes less likely. Light intensity experiments show that the external flow already has an influence for $M = 0.2$. One of the conclusions of the investigation by Pereira *et al* is that the DBD plasma actuator's power consumption does not change with varying the external flow speed (for the operating conditions maintained in the particular study). Furthermore, the light emission for both co- and counter-flow orientation of the actuator was investigated by means of a CCD camera. For the counter-flow forcing, increasing the external flow velocity increases the light emission as well. This effect is observed much less in the co-flow orientation. Figure 2.12 shows the difference in force with and without plasma actuation obtained by a load cell. The change in skin frictions due to actuation is included in this difference $|\Delta F|$. Co-flow forcing increases the skin friction, since the induced velocity profile steepens the gradient near the wall. The opposite is true for the counter-flow case.

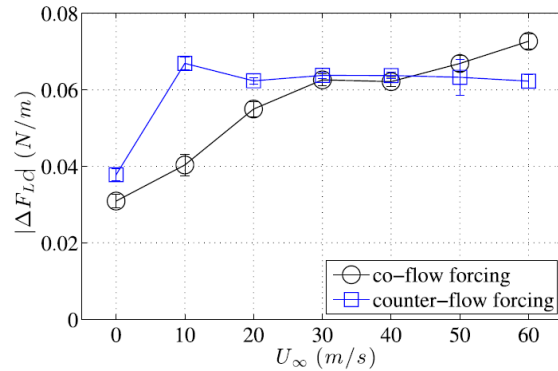


Figure 2.12: Measured force difference between actuator on and off setting [8].

The measured force for quiescent flow is nearly half of that measured for higher velocity flows. The wall parallel jet accompanying the body force induces shear stress at the wall opposing that force. For higher external flow velocities, the boundary layer skin friction dominates the force at the wall. The levelling off can be explained as the actuator being unable to modify the flow skin friction and thus the flow. This is however not certain, as the two outliers for 50 m/s and 60 m/s do not fit this explanation. At 10 m/s, a large difference between the co- and counter-flow orientated force differences can be noted. The flow is laminar without actuation for this case, but the counter-flow actuator induces transition. The body force points in the same direction as the skin friction and the compounded force explains the discrepancy. An important conclusion from this is that current DBD actuators may already be stronger than expected. The actuator's effect on the change in skin friction is not representative in studies under quiescent conditions for flows of higher velocities.

2.3 Current state-of-art Modeling of the DBD plasma actuator

Due to the large influence of a myriad of geometric and physical parameters, numerical modeling is needed to reduce the amount of experiments required. The joint solution of the time-dependent full set of Navier-Stokes equations and transfer equations for charged particles is complex problem to solve [31]. Several approaches to model the effect of DBD plasma actuators have been developed and will be explained in the following sections. Various level of detail is found in the modelling effort, ranging from first principle models which capture the essential physics but are cumbersome to work with, to simple phenomenological which need experimental calibration and come with restricted validity.

2.3.1 First principle models

A fundamental modeling approach is taken by Kuryachii *et al.* [31] to model the discharge in air of a DBD actuator. The discharge is examined at the level of the separate particles.

Electrons, positive nitrogen and oxygen ions, and negative oxygen ions are represented in the diffusion-drift approximation.

In the dielectric layers and the external domain, the Laplace equation is solved (left of Equation 2.4), in the gas phase domain where the plasma occurs, the Poisson equation is solved (right of Equation 2.4) where φ is the electric potential, ε_0 is the dielectric impermeability in vacuum, e is the elementary charge and n is the concentration of positive/negative ions or electrons.

$$\Delta\varphi = 0 \quad , \quad \varepsilon_0\Delta\varphi = e(n_p - n_n - n_e) \quad (2.4)$$

The diffusion-drift approximation has three differential continuity equations, one for each of the type of particles mentioned above. Boundary conditions regarding continuity of potential and electric induction are set. These can be evaluated by assuming an absence of electric field and a given background concentration of positive ions, which allows the continuity equations to be set to zero and be solved for the specific case. For the charged particle fluxes, a different physical model was used found in [32], with its corresponding dependencies. The instantaneous horizontal force can then be found with integration over the plasma region domain S (with the electric field strength E):

$$F_x = \iint_S f_x dx dy \quad , \quad f_x = e(n_p - n_n - n_e)E_x \quad (2.5)$$

Another model grounded in first principles observing the discharge in high detail is that of Likhanskii [?].

Singh and Roy also treat the DBD actuator as a device which delivers heat and momentum input into a small control volume [33]. However, to circumvent expensive and long computations, the electrodynamic force is approximated sufficiently well to couple immediately to the Navier-Stokes equations. Strict first principle modelling would require self-consistent solving of the continuity equations for different particles, the Poisson's equation and the Navier-Stokes equation. The spatial dependence of the electrodynamic force of the plasma actuator is however derived from first principle calculations. Simplifications are however done by neglecting certain species. After solving the governing equations for the remaining species and electric potential, the body force produced by the actuator can be approximated as:

$$\mathbf{F} = F_{x_0}\phi_0^4 \exp(-\{[x-x_0-(y-y_0)]/y\}^2 - \beta_x(y-y_0)^2)\hat{\mathbf{i}} + F_{y_0}\phi_0^4 \exp(-[(x-x_0)/y]^2 - \beta_y(y-y_0)^2)\hat{\mathbf{j}} \quad (2.6)$$

where F_{x_0} and F_{y_0} are the average body force obtained by solving the air-plasma equations, ϕ the potential, x_0 the horizontal location of the midpoint between both electrodes, y_0 the vertical location of the dielectric surface, and the β s are functions of the dielectric material. Nine cases with different operating conditions were investigated for the study. Reasonable agreement regarding the actuator's induced velocity was found between the approximate method and the results of the full set of plasma equations. The latter were used for calibration of the coefficients in the approximate force expression. The fourth order polynomial in potential can be dubbed to be a 'sufficiently well' approximation for this case. Important to note that its relevance is limited. Since the solution is very sensitive to the initial conditions, the obtained results are only valid for the chosen operational parameters of the study at hand.

2.3.2 Space-time lumped-element circuit model

The space-time lumped-element circuit model set up by Orlov does not need experimental calibration to model the details of the ionization process for body force predictions over the range of operating conditions [9]. The dielectric and part of the air where plasma is generated is modelled by N parallel network of resistors and capacitors of which the characteristics vary with distance from the exposed electrode. Each of the networks consist out of an air capacitor, a dielectric capacitor, a plasma resistive element and a zener diode. The latter are added to set a threshold value on the voltage differential required for plasma formation, as well as to switch into different plasma resistance values depending on the current direction. A schematic representation of the model is shown in Figure 2.13.

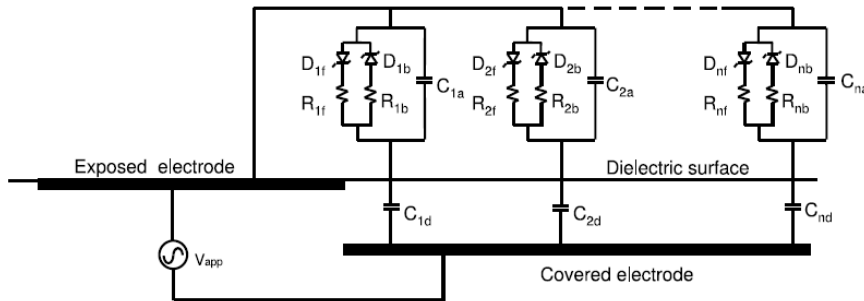


Figure 2.13: The electric circuit model for N parallel networks representing a single DBD plasma actuator [9].

The air capacitor and plasma resistance value depend on the distance from the exposed electrode, the value of the dielectric capacitor relies upon the characteristics of the dielectric material. A differential equation for the time-varying voltage on the surface of the dielectric can be found making use of the above parameters, and an expression for the time-varying current. It was shown that this approach needs in the order of 100 parallel networks to capture the essential physics ($N \approx 10^2$). A validation with experimental results is performed and good agreement is with the model regarding the maximum extent of the plasma and the plasma sweep velocity. The temporal solution of the voltage on the barrier surface serves as a time-dependent boundary condition of the electric potential ϕ , used in the electrostatic equation. The solution of that equation then ultimately leads to the time-dependent body force produced by the plasma actuator. This formulation of the body force can easily be integrated into a Navier-Stokes solver.

2.3.3 Experimentally derived force distributions

A large drawback of conventional experimental studies of DBD actuators is that the measurements of thrust are not the pure actuator effect but also include the shear forces developed between the flow and surface. Also, no spatial distribution of the force field is obtained. Kotsonis *et al.* therefore propose to use high-speed particle image velocimetry (PIV) [10] for a phenomenological model.

Two body force estimation methods are suggested with the two-dimensional incompressible Navier-Stokes equations shown below as a basis.

$$\frac{\partial \mathbf{U}}{\partial t} + \mathbf{U} \cdot \nabla \mathbf{U} - \nu \nabla^2 \mathbf{U} = -\nabla p + \frac{\mathbf{F}}{\rho} \quad (2.7)$$

where \mathbf{F} is the body force, \mathbf{U} is the 2D velocity field, p is the static pressure, ν is the kinematic viscosity and ρ is the density.

The reduced method is basically Newton's second law and is obtained for initial conditions of zero velocity with negligible convective, viscous and pressure gradient terms. All but the first and last term of Equation 2.7 vanish.

The gradient method makes use of all terms of the NS equations which it obtains from the spatio-temporal data of the velocity field found with PIV. The pressure gradient and body force terms are both unknowns. This can be bypassed by assuming that the body force remains quasi-steady over a large amount of HV cycles and that the pressure gradient prior to actuation is zero. Differentiating Equation 2.7 and using the assumptions before integrating again presents an expression for the pressure term to be substituted in the base equation, leaving only the body force term unknown.

Both gradient and reduced methods produce similar results, albeit that the latter has a slightly larger magnitude. Spatial distribution of the body force are shown in Figure 2.14. The semi-elliptical nature of the forcefield can be seen.

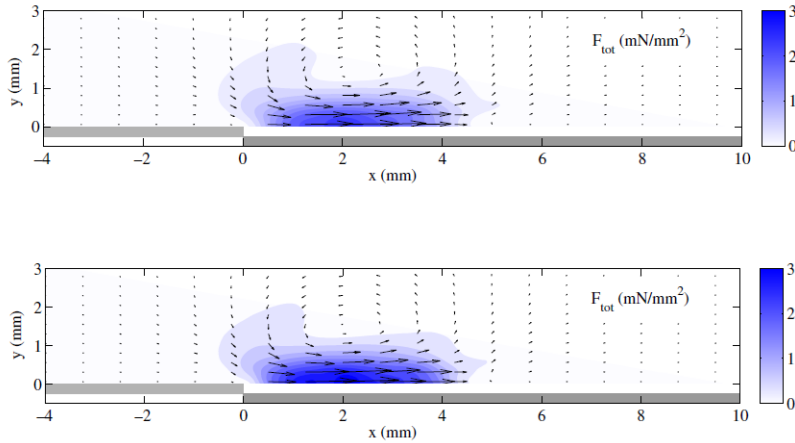


Figure 2.14: Spatial body force distribution using the reduce (top) and gradient method (bottom) for 12 kV_{pp} and 2 kHz [10].

The difference in value can be attributed to reduction of terms in the first method as well as the ambiguity in the selection of the initial acceleration time span. The gradient method has higher accuracy, also due to its relative independence of time span for the force calculation. Both methods were benchmarked with direct thrust measurement with a load cell as well as with a thrust calculation through a momentum balance on the domain of plasma generation. Good agreement is found, although the gradient and reduced methods consistently overestimate the thrust. This was expected, since the conventional

methods also contain the shear stress at the wall.

A further study on the matter by the same authors was done as validation and verification of the proposed techniques [34]. Test cases for continuous and pulse operation over various operating conditions.

Overall, the numerical results match the measurements sufficiently accurately independent from the conditions of the original force measurements in quiescent flow. The case of a non-zero external flow has not been tested yet by the authors. One of the major assumptions of the approximated method is the time-invariance of the body force. It is seen from the experiments that, although high frequency oscillations are not duplicated, the global induced flow field is estimated reasonably well.

Another approach using experimental data obtained by PIV measurements is that of Maden *et al.* [11]. He suggests using the Reynolds Averaged Navier Stokes equations (RANS) since the resolution in time and space of the time-averaged PIV data is not sufficiently high to apply the NS directly. With this approach, the treatment of the additional Reynolds Stress Tensor (RST) is of particular importance. The measurement of the velocity field which is used in the analysis is shown in Figure 2.15.

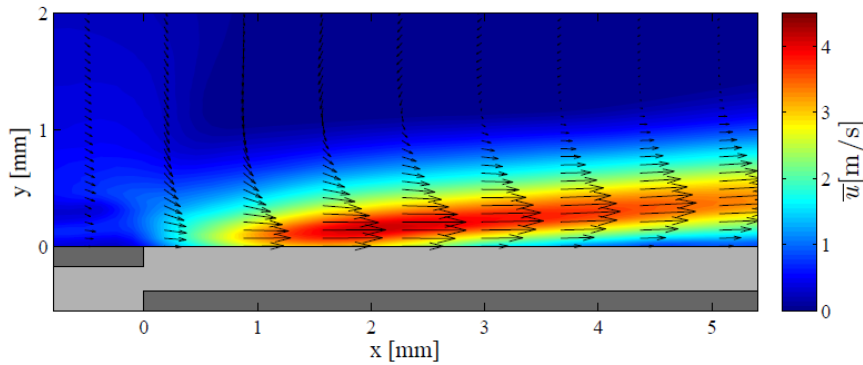


Figure 2.15: The velocity field constructed from PIV measurements which is the basis for the subsequent analysis of Maden *et al* [11].

The derivatives required for the plasma body force calculation are calculated using the experimental velocity data. The RANS equation is rewritten to give the body force term, and a magnitude analysis is performed on the single terms. The contribution of the Reynolds stress term is seen to be significant, which is related to the unsteadiness of the plasma actuators on the time scale of the operating frequency. Using the steady body force density distribution along with the steady RANS, the high velocity fluctuations of the turbulent production associated with the body force cannot be reproduced numerically. The authors suggest using a near-wall second-moment closure model to represent that part of the turbulent production (as found in [35]).

2.3.4 Potential flow panel method

Hall [36] was one of the first to model DBD plasma actuators in panel methods. It was done for potential flow only. Experimental PIV data was used to establish that the plasma actuator's effect mimics that of a doublet in potential flow. The freestream airflow seems to be drawn into the surface in the plasma region and subsequently jetted (horizontally) away from the actuator. This can account for behavior replicating a sink and source respectively. This phenomenological model is accurate up to a first order approximation, but still good agreement is found between experimental and numerical lift coefficient results. The doublet strength is found as an objective function based on the local velocity, which requires experimental calibration.

A large variety of panel methods exist and Hall uses the Smith-Hess method to incorporate the plasma panel. It was chosen because of its good agreement with experimental measurements of airfoil characteristics. Important to remark here is that influence of the plasma actuator is modeled through its incurred change in the momentum of the local flow.

2.3.5 Synthesis and need for plasma-specific closures

What the previously described state-of-the-art overview of DBD models makes clear, is that a wide range of approaches exist. Most plasma body force models assume decoupled relations between the flow field and the body force.

Fundamental models [31] [37], offer great insight in the working of the DBD plasma actuator up to the level of the behavior of the ionized particles. A complex set of differential continuity equations need to be solved, increasing the complexity and computation time. The space-time lumped-element circuit model [9] suffers from the same drawback. These model formulations are more suitable as part of a Navier-Stokes solver. Experimentally derived force distributions show promising results, despite their relatively lower level of physical rigor. The effect of the actuator on the flow velocity (and hence momentum) is used for modeling, instead of through its electrical characteristics. One of the main disadvantages of the method proposed by [10] is the required experimental velocity fields for every type of actuator. An extended validity range for a given experimental calibration is found in the implementation of the actuator in a panel code as demonstrated by [36]. This approach seems promising with the desired coupling of rapid-analysis airfoil codes in mind.

For rapid airfoil analysis with low computational cost while retaining reasonable accuracy, viscous-inviscid panel codes as found in [23] (Xfoil), [24] (Rfoil) and [25] (Quick) remain an attractive option and are widely used in industry. In contrast to the potential flow model of Hall, it is the author's opinion that the influence of the actuator on the boundary layer should be taken into account. This is because the body force region is situated inside the viscous boundary layer. As such, the effect should be better modeled through a modification of the closure relations expressing the relation between various boundary layer integral variables.

The choice is made to therefore include the DBD plasma actuation body force in the Integral Boundary Layer formulation. In this way, the modified viscous-inviscid panel method can be used directly for airfoil optimization.

Integral Boundary Layer Formulation

The integral boundary layer formulation is studied in more detail since it is used in rapid-analysis airfoil design tools. After treating the history and defining the main features of boundary layer flow, the equations themselves are elaborated.

3.1 General overview

3.1.1 History

Prandtl's lecture "ber Flüssigkeitsbewegungen bei sehr kleiner Reibung" ("On fluid flow with very little friction") at the 1904 Mathematical Congress in Heidelberg has had a profound impact on the field of aerodynamics as it is known today [14]. He made a distinction between a very thin layer adjacent to the surface and the rest of the flow, further away from the wall. In the thin boundary layer the role of viscosity is dominant. Conversely, in the part of the flow further away viscosity can be completely neglected. With Prandtl's findings, the d'Alembert paradox could be resolved. The addition of a boundary layer with viscous effects proved to be the answer why a body placed in a flow experiences a force.

The Reynolds number, which is defined as $Re = \rho UL/\mu$ is a measure for the dominance of inertial over viscous forces. It also provides an indication of the thickness of this boundary layer. A high Reynolds number signifies a thin layer, whilst with decreasing the Re the boundary layer grows. Additionally with the definition of the Reynolds number, it is found that the full Navier-Stokes equations can be simplified when assuming a high value of Re . For this case of a thin boundary layer, the flow near the body surface can be represented by the boundary layer equations. These can be solved more easily than the Navier-Stokes set. The outer region is described by the inviscid formulations where viscosity is neglected. The boundary layer equations will be derived in the following sections.

The theory of Prandtl lead to the important no-slip condition at the boundary. The fluid flow is at rest relative to the body at the surface. The flow velocity increases from zero at the wall to the freestream value at the edge of the boundary layer. Large velocity gradients in the direction normal to the wall are present near the surface, which are related to shear stresses due to viscosity [38].

3.1.2 Boundary layer flow features

As an illustration, the development of the boundary layer on a flat plat aligned parallel to the flow is shown in Figure 3.1. Before the flat plate is encountered, the velocity distribution is uniform with a flow velocity equal to the freestream mean velocity, depicted in stage (a). When the fluid passes over the flat plate, the fluid elements in contact with the surface decelerate due to the shear stress from viscosity. The flow becomes retarded as particles are slowed down due to the friction. On the edge of the boundary layer, the faster moving main flow entrains particles as well, resulting in the velocity profile seen in instance (b).

As the flow progresses more downstream, the thickness of the boundary layer increases. Due to for instance the shape of the body, the rising static pressure consequently leads to a reduction in dynamic pressure which entails a decrease of velocity [12]. The situation sketched in stage (c) is that of a zero pressure gradient, the turning point between favourable and adverse pressure gradients. The latter can give rise to separation and reverse flow is encountered in the boundary layer. This is shown in the figure for cases (d) and (e). Separation is detrimental for aerodynamic performance and results in large energy losses. During design, a lot of effort is put into avoiding or delaying separation.

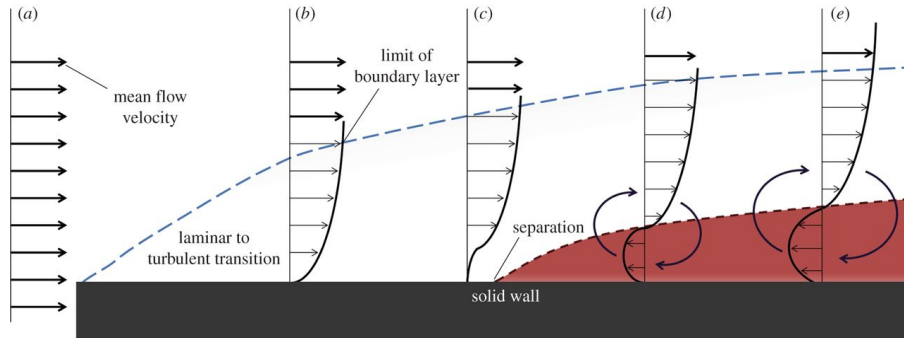


Figure 3.1: Development of the boundary layer on a flat plate [12].

Besides attached and separated flow, a further distinction for attached flow can be made. If the streamlines of the instantaneous flow field are smooth and nearly parallel, the flow can be considered laminar. The boundary layer in that case is relatively thin and exhibits low drag. If the flow around the flat plate is again considered, laminar flow will occur at the beginning of the plate. Downstream of this point, at a location depending on the Reynolds number, instabilities in the flow are amplified and a transition from laminar to turbulent flow occurs.

Transition can be triggered through various mechanisms [15]. Forced transition is caused by a physical object on the surface such as a rivet, panel edge, surface imperfection or trip wire. If the height of this object is comparable to the height of the boundary layer, then external disturbances are very likely to enter and trigger transition.

Natural transition occurs in quiet flow on relatively smooth surfaces with very weak external disturbances. This kind of flow exists in wind tunnels or external flow in flight. Initial disturbances are amplified by natural flow instabilities and increase exponentially downstream. The most common type in quasi-2D flow is a Tollmien-Schlichting wave, which is a sinusoidally oscillating pressure and velocity perturbation inside the boundary layer. Eventually, these disturbances become chaotic, signifying transition to turbulence. Through comparison of the local and initial wave amplitudes, transition of this type can be predicted by what is called e^N methods.

In very noisy surroundings, disturbances from the inviscid flow outside the boundary layer are strong enough to enter it and cause transition if the local conditions allow turbulence to be sustained. This type of transition can be found in turbomachinery.

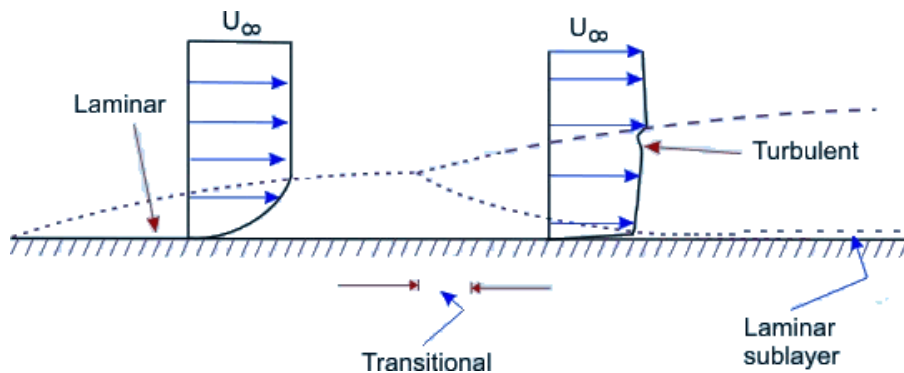


Figure 3.2: Transition of the boundary layer on a flat plate [13].

Turbulent flow is characterized by a much more irregular flow pattern. This is caused by velocity fluctuations (in all directions) which can be orders of magnitude smaller than the mean flow. The streamlines of the mean flow however remain parallel to the surface. The fluctuations results in a larger mixing of the boundary layer with the outer flow. This in turn increases the diffusion rates of quantities such as momentum and vorticity with respect to the laminar case, as well as the boundary layer thickness. This is illustrated in Figure 3.2. The shear stress caused by the additional momentum transfer due to eddies for turbulent flows is larger than the shear stress contribution by the momentum transfer produced by viscosity. This is not valid in a small region near the surface, dubbed the viscous sublayer. The turbulent stresses in that part of the boundary layer are so small that it is sometimes referred to as the laminar sublayer [14] and it is dominated by viscous shear stresses. A transition layer is formed between the viscous sublayer and the outer layer (which is still inside the boundary layer). In general, because the wall shear stress is higher, the total drag of the body is also higher than in laminar flow.

In the case of wind turbines, the leading edge is often contaminated due to degradation caused by precipitation, insects or dust accumulation [39]. As such, transition will likely

occur and the flow will be in turbulent state over a large part of the airfoil. This is why turbulent flow is the main concern of the content of the thesis...

3.2 Integral boundary layer equations

The starting point of what will eventually be the integral boundary layer equations with a term accounting for DBD plasma actuation, is the two-dimensional Navier-Stokes equations. These are too time-consuming and computationally expensive to solve entirely, and order-of-magnitude analysis with additional assumptions regarding flow close to the wall will result in simpler boundary layer equations.

3.2.1 General flow equations

The equations of motion for two-dimensional flow is given by the series of conservation laws shown in Equation 3.1. The Cartesian coordinate system is used with the tangential or parallel (x) and normal (y) direction and respective velocity components (U, V). The kinematic viscosity ν is defined as the ratio between the dynamic viscosity μ and density ρ . P is the pressure and the body force term is denoted by F .

$$\begin{aligned} U \frac{\partial U}{\partial X} + V \frac{\partial U}{\partial Y} &= -\frac{1}{\rho} \frac{\partial P}{\partial X} + \nu \left(\frac{\partial^2 U}{\partial X^2} + \frac{\partial^2 U}{\partial Y^2} \right) + \frac{1}{\rho} F_x \\ U \frac{\partial V}{\partial X} + V \frac{\partial V}{\partial Y} &= -\frac{1}{\rho} \frac{\partial P}{\partial Y} + \nu \left(\frac{\partial^2 V}{\partial X^2} + \frac{\partial^2 V}{\partial Y^2} \right) + \frac{1}{\rho} F_y \\ \frac{\partial U}{\partial X} + \frac{\partial V}{\partial Y} &= 0 \end{aligned} \quad (3.1)$$

The set of Navier-Stokes equations given here represent the balance of momentum and the conservation of mass relation for a steady Newtonian fluid. The creation, transport or destruction of these quantities are equal to the time rate of change

The above equations describe the fluid flow as a continuum. This approach is important to note with respect to the description of the plasma actuation, but also imply that the shear stress on the surface of the control volume is directly dependent on the velocity gradient perpendicular to that surface. The skin friction is characterized as such by Equation 3.2.

$$\tau_w = \mu \left(\frac{\partial U}{\partial Y} \right)_{y=0} \quad (3.2)$$

The momentum exchange through molecular diffusion is assumed constant, implying a fixed value for μ . This assumption is justified for the relatively low speeds which will be considered. In the supersonic flow regime, with large temperature variations, varying viscosity should be accounted for. The capitals used in Equation 3.1 and Equation 3.2 denote the fact that dimensional quantities are used. The body force term at the end of the momentum equations here is a volume force acting along the span of the specified direction, resulting in $\left[\frac{N}{m^2} \right]$ units.

3.2.2 Boundary layer equations

To make the above equations non-dimensional, a set of adimensional quantities is defined. The length scales L and δ are used for the parallel and normal direction respectively. The former is usually the chord length when describing airfoils and not too close from the body flow variations appear in this length scale. The δ is the dimensional boundary layer thickness. Its definition is somewhat more arbitrary, since the edge of the boundary layer can be difficult to determine. Therefore, the height at which the local velocity has reached 95 or 99% of the free stream value can be taken, marked as δ_{95} or δ_{99} . As a scaling for the velocity, the edge velocity U_e is taken, resulting in the following set of adimensional variables:

$$\begin{aligned} x &= \frac{X}{L} & u &= \frac{U}{U_e} & p &= \frac{P}{\rho U_e^2} \\ y &= \frac{Y}{\delta} & v &= \frac{V}{U_e} \frac{L}{\delta} & t &= \frac{U_e T}{L} \end{aligned}$$

It should be noted that the scaling for the normal velocity v is found through dimensional analysis of the continuity equation, which results in $V \sim \frac{U\delta}{L}$ [14]. Feeding in the non-dimensionalizing relations yields the adimensional momentum equations shown in Equation 3.3. Since it is assumed that no shock waves are present, the pressure terms adapts to the other terms in the equation and no special scaling is required. Furthermore, the edge velocity is considered independent of (x, y) and differentiation is taken to be a linear operation. This is reasonable for typical pressure gradients, but only exact for the zero pressure gradient case.

$$\begin{aligned} \left(\frac{U_e^2}{L}\right) u \frac{\partial u}{\partial x} + \left(\frac{U_e^2}{L}\right) v \frac{\partial u}{\partial y} &= -\frac{U_e^2}{L} \frac{\partial p}{\partial x} + \nu \left[\left(\frac{U_e}{L^2}\right) \frac{\partial^2 u}{\partial x^2} + \left(\frac{U_e}{\delta^2}\right) \frac{\partial^2 u}{\partial y^2} \right] + \frac{1}{\rho} F_x \\ \left(\frac{U_e^2 \delta}{L^2}\right) u \frac{\partial v}{\partial x} + \left(\frac{U_e^2 \delta}{L^2}\right) v \frac{\partial v}{\partial y} &= -\frac{U_e^2}{\delta} \frac{\partial p}{\partial y} + \nu \left[\left(\frac{U_e \delta}{L^3}\right) \frac{\partial^2 v}{\partial x^2} + \left(\frac{U_e \delta}{L \delta^2}\right) \frac{\partial^2 v}{\partial y^2} \right] + \frac{1}{\rho} F_y \end{aligned} \quad (3.3)$$

From the x -momentum equation, it can be seen that the convective terms are equally large ($\sim \frac{U_e^2}{L}$). Also, because the longitudinal length scale is much larger than the perpendicular $\delta \ll L$, it can be seen that the diffusive term with the x -derivative is much smaller than the diffusive term derived in y . The largest part of the diffusion term is of comparable order of the convective term, the following order of magnitude analysis can be made:

$$\mathcal{O}\left(\frac{U_e^2}{L}\right) \sim \mathcal{O}\left(\frac{\nu U_e}{\delta^2}\right) \quad \rightarrow \quad \mathcal{O}(\delta) \sim \mathcal{O}\left(\frac{L}{\sqrt{Re}}\right)$$

An approximate relation for the boundary layer thickness is found if instead of the orders the quantities are equated. This expression, together with a reorganized form of the momentum equation to make the Reynolds number apparent can be used to rewrite Equation 3.3 into the following form:

$$\begin{aligned}
Re \left(u \frac{\partial u}{\partial x} + v \frac{\partial u}{\partial y} \right) &= Re \left(-\frac{\partial p}{\partial x} + \frac{\partial^2 u}{\partial y^2} + \frac{L}{\rho U_e^2} F_x \right) + \frac{\partial^2 u}{\partial x^2} \\
u \frac{\partial v}{\partial x} + v \frac{\partial v}{\partial y} &= Re \left(-\frac{\partial p}{\partial y} + \frac{1}{\sqrt{Re}} \frac{L}{\rho U_e^2} F_y \right) + \frac{1}{Re} \frac{\partial^2 v}{\partial x^2} + \frac{\partial^2 v}{\partial y^2}
\end{aligned} \tag{3.4}$$

The body force terms, of which the magnitude remains unknown at this point, are "passively" scaled. The scaling factor is the result of the manipulation performed on the equation. To obtain the final system of Non-dimensional Boundary Layer PDEs, the limit to infinity of the Reynolds number is taken on Equation 3.4 which yields:

$$\begin{aligned}
u \frac{\partial u}{\partial x} + v \frac{\partial u}{\partial y} &= -\frac{\partial p}{\partial x} + \frac{\partial^2 u}{\partial y^2} + \frac{L}{\rho U_e^2} F_x \\
0 &= -\frac{\partial p}{\partial y} + \frac{1}{\sqrt{Re}} \frac{L}{\rho U_e^2} F_y
\end{aligned} \tag{3.5}$$

When taking into account the new-found relation for the boundary layer thickness $\delta = \frac{L}{\sqrt{Re}}$, the Dimensional Boundary Layer PDEs are found to be:

$$\begin{aligned}
U \frac{\partial U}{\partial X} + V \frac{\partial U}{\partial Y} &= -\frac{1}{\rho} \frac{\partial P}{\partial X} + \nu \frac{\partial^2 U}{\partial Y^2} + \frac{1}{\rho} F_x \\
0 &= -\frac{\partial P}{\partial Y} + F_y
\end{aligned}$$

3.2.3 Integral boundary layer equations

The partial differential equations of the boundary layer equations are easier to handle than the complete Navier-Stokes, but can be reduced even more through integration with the definition of new integral variables.

Integral variables

To continue the derivation, the dimensional form will first be considered. Therefore, some dimensional defect integrals and thicknesses will be defined.

- The first of these quantities is the displacement thickness δ_1 which is given by Equation 3.6. It can be seen as the effect the boundary layer has on the potential flow. Due to the presence of the boundary layer, the streamlines are displaced slightly away from the surface. The mass flow is smaller in the inviscid case due to the no-slip condition at the wall. The displacement thickness is the location to

which the boundary has to be shifted for a potential flow to have the same mass flow as the inviscid original flow.

$$\delta_1 = \int_0^\infty \left(1 - \frac{U}{U_e}\right) dY \quad (3.6)$$

The shaded areas in Figure 3.3 have the same area. From this it can be seen that the boundary layer modifies the shape that is experienced by the external flow. It appears to be thicker due to the low velocities near the wall. A nice feature of the displacement thickness is that it avoids the difficulties of the outright boundary layer thickness. The local velocity approaches the free stream value asymptotically. The upper limit in the integral is the point where the integrand becomes negligible.

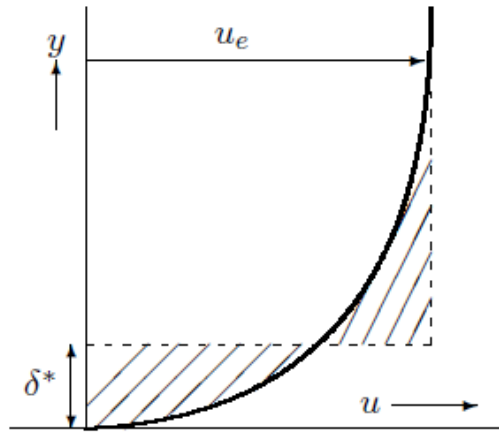


Figure 3.3: Visualization of the displacement thickness δ^* . [14].

- The retardation of the flow not only has consequences for the mass transport, but also the momentum flux. Similar to the displacement thickness, a momentum thickness δ_2 can be defined as given in Equation 3.7. It is the distance over which the boundary needs to be displaced such that an inviscid flow produces the same momentum transport. The quantity is related to the drag, as can be seen in classical far-field profile drag analyses such as performed in [15]. The momentum thickness can also be used to estimate the thickness of the shear layer in separated flow, which is approximately 8 times the length of δ_2 .

$$\delta_2 = \int_0^\infty \frac{U}{U_e} \left(1 - \frac{U}{U_e}\right) dY \quad (3.7)$$

- To complete the set, next to mass flow or momentum also kinetic energy can be considered. The energy thickness δ_3 is shown in Equation 3.8. The kinetic energy

defect is related to the viscous dissipation in the boundary layer, and is related to the profile drag as well.

$$\delta_3 = \int_0^\infty \frac{U}{U_e} \left(1 - \frac{U^2}{U_e^2}\right) dY \quad (3.8)$$

The comparison how these three thicknesses relate is shown in Figure 3.4. Note that the adimensional thicknesses are used, which are δ^* , θ and θ^* for the displacement, momentum and kinetic energy thickness respectively. They are obtained by dividing the quantities by the longitudinal length scale. For airfoil analysis, the chord length L is used.

$$\delta^* = \frac{\delta_1}{L} \quad , \quad \theta = \frac{\delta_2}{L} \quad , \quad \theta^* = \frac{\delta_3}{L} \quad (3.9)$$

Since the local velocity is smaller than the edge velocity, the momentum thickness is smaller than the kinetic energy thickness.

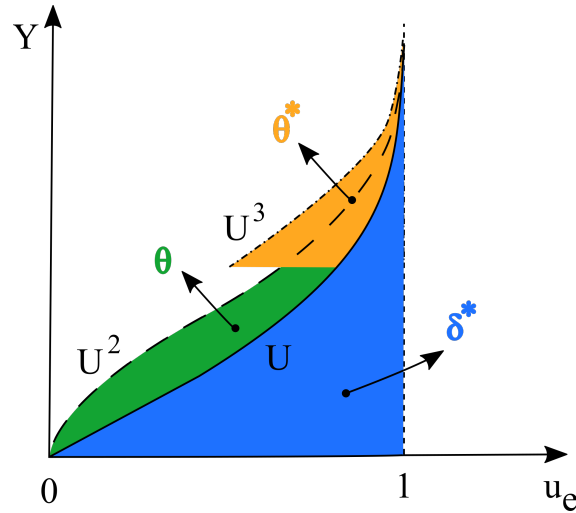


Figure 3.4: Normalized velocity $U = U_{local}/U_e$ versus displacement from the wall n for displacement thickness δ^* , momentum thickness θ and kinetic energy thickness θ^* [15].

- The thicknesses above can be related to each other in shape factors. The most common is H or H_{12} , but also the energy shape factor H^* or H_{32} is used.

$$H_{12} = \frac{\delta_1}{\delta_2} \quad , \quad H_{32} = \frac{\delta_3}{\delta_2} \quad (3.10)$$

The shape factor H depends on the pressure gradient and is a measure for the shape of the velocity profile. A high value of H , signifies a high adverse pressure gradient. This dependence is shown for two values of H in Figure 3.5. From theory such as [16], typical values of this parameter can be found. An $H \approx 1.3 - 1.4$ is typical of turbulent boundary layers, whilst $H = 2.59$ represents the laminar Blasius boundary layer. Over an airfoil with laminar flow, a value of $H \approx 2.2$ is found near the stagnation point for convex velocity profiles, and $H \approx 4$ corresponds to concave velocity profiles near separation.

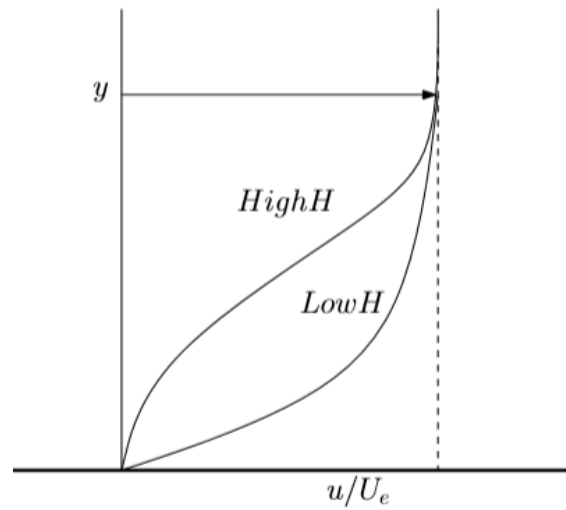


Figure 3.5: Normalized velocity profile versus shape factor H [16].

- The last parameter which is defined is integral across the boundary layer of the rate at which energy is dissipated due to the action of viscosity, D , and its non-dimensional dissipation coefficient C_D . The kinetic energy dissipates into heat by the shear stress τ acting on the flow which deforms at the shear strain rate $\frac{\partial U}{\partial Y}$. The quantity is almost always positive.

$$D = \int_0^\infty \mu \left(\frac{\partial U}{\partial Y} \right)^2 dY \quad , \quad C_D = \frac{D}{\rho U_e^3} \quad (3.11)$$

Integral momentum equation

The starting point of the rest of the derivation of the Integral Boundary Layer Equations follows from Boundary Layer Equations and the mass continuity, derived earlier and rewritten below:

$$U \frac{\partial U}{\partial X} + V \frac{\partial U}{\partial Y} = U_e \frac{dU_e}{dX} + \nu \frac{\partial^2 U}{\partial Y^2} + \frac{1}{\rho} Fx \quad (3.12)$$

$$\frac{\partial U}{\partial X} + \frac{\partial V}{\partial Y} = 0 \quad (3.13)$$

Note however that the pressure term in Equation 3.13 has been reformulated making use of the Euler equation with zero normal velocity, or alternatively from Bernoulli's law (Equation 3.14). The order of magnitude analysis reveals that for thin boundary layers, which occur at high Reynolds numbers, the normal gradient of the pressure should be very small and could be neglected. The pressure is constant through the boundary layer, and the value itself is related to the flow at the edge.

$$\begin{aligned}
P + \frac{1}{2}\rho U^2 = \text{constant} &\quad \rightarrow \quad -\frac{1}{\rho} \frac{dP}{dX} = U \frac{dU}{dX} \\
&\quad \rightarrow \quad -\frac{1}{\rho} \frac{dP_e}{dX} = U_e \frac{dU_e}{dX}
\end{aligned} \tag{3.14}$$

In order to obtain the Integral Momentum Equation, the first step is to multiply the mass continuity of the inner flow and multiply it with the velocity deficit ($U_e - U$). It is subsequently added to Equation 3.12 to yield:

$$-\nu \frac{\partial^2 U}{\partial Y^2} = U_e \frac{dU_e}{dX} - U \frac{dU}{dX} + (U_e - U) \frac{\partial U}{\partial X} - V \frac{\partial U}{\partial Y} + (U_e - U) \frac{\partial V}{\partial Y} + \frac{1}{\rho} F_x \tag{3.15}$$

The integrands in first derivatives in Y and X are then reworked by adding derivatives in these of U_e ($=0$ since $U_e \perp (X, Y)$). This allows the equation to be written in terms which are integrands of the integral quantities defined in the previous section. Mass and momentum can then be integrated along the wall normal coordinate Y.

$$\begin{aligned}
\int_0^\infty \left(-\nu \frac{\partial^2 U}{\partial Y^2} \right) dY &= \int_0^\infty (U_e - U) \frac{\partial U_e}{\partial X} dY + \int_0^\infty \frac{\partial}{\partial X} (U_e U - U^2) dY \\
&\quad + \int_0^\infty \frac{\partial}{\partial Y} (U_e V - UV) dY + \int_0^\infty \left(\frac{1}{\rho} F_x \right) dY
\end{aligned} \tag{3.16}$$

The left-hand side of the equation is evaluated keeping in mind that $\nu \perp Y$ and that shear stress $\mu \frac{\partial U}{\partial Y}$ vanishes outside the boundary layer. The displacement thickness becomes evident in the first term at the right-hand side remembering that $U_e \perp Y$. Since the flow is assumed to not have discontinuities present, the integrals should be smooth and defined. This allows for changing the order of the derivative and integration in the second term, in which the momentum thickness appears. The evaluation of the third integral exploits the no-slip condition and the fact that the velocity deficit goes to zero far away from the wall. No suction is assumed to be present, so the vertical velocity component is neglected. This results in the Integral Momentum Boundary Layer Equation, or the first Von Karman Integral Equation shown in Equation 3.17. The force term accounts for the plasma actuation and will be reworked at a later stage.

$$\frac{\tau_w}{\rho} = \frac{\partial U_e}{\partial X} U_e \delta_1 + \frac{\partial}{\partial X} (U_e^2 \delta_2) + \int_0^\infty \left(\frac{1}{\rho} F_x \right) dY \tag{3.17}$$

Equation 3.17 can be made non-dimensional by dividing both sides by U_e^2 . The adimensional quantities defined earlier become apparent. It should be noted that the suction term is kept for completeness, and made non-dimensional by stating that $U_e \neq U_\infty$. The non-dimensional Integral Momentum Boundary Layer Equation is:

$$\frac{C_f}{2} = (H_{12} + 2) \frac{\theta}{u_e} \frac{\partial u_e}{\partial x} + \frac{\partial \theta}{\partial x} + \int_0^\infty \left(\frac{F_x}{\rho U_e^2} \right) dY \tag{3.18}$$

Integral energy equation

The energy equation departs from the same base equations (Equation 3.12 and Equation 3.13), but the momentum equation is multiplied with $2U$ and the continuity equation by $(U_e^2 - U^2)$. They can be added again since continuity is preserved.

$$-2\nu U \frac{\partial^2 U}{\partial Y^2} = 2UU_e \frac{\partial U_e}{\partial X} - 2U^2 \frac{\partial U}{\partial X} + (U_e^2 - U^2) \frac{\partial U}{\partial X} - 2UV \frac{\partial U}{\partial Y} + (U_e^2 - U^2) \frac{\partial V}{\partial Y} + \frac{2U}{\rho} F_x \quad (3.19)$$

By reworking the first derivatives in X and employing properties of the differentiation, an expression with the δ_3 integrand is obtained. Also the first Y-derivatives are written more compact. The left hand side of the combined equation is reworked using a differentiation identity based on the chain rule on $\frac{\partial}{\partial Y} (U \frac{\partial U}{\partial Y})$. The equation is then integrated from the wall to infinity in the Y coordinate:

$$\int_0^\infty 2\nu \left(\frac{\partial U}{\partial Y} \right)^2 dY - 2\nu \int_0^\infty \frac{\partial}{\partial Y} \left(U \frac{\partial U}{\partial Y} \right) dY = \int_0^\infty \frac{\partial}{\partial X} \left(U_e^3 \left[\frac{U}{U_e} \left(1 - \frac{U^2}{U_e^2} \right) \right] \right) dY + U_e^2 \int_0^\infty \frac{\partial}{\partial Y} \left[V \left(1 - \frac{U^2}{U_e^2} \right) \right] dY + \int_0^\infty \left(\frac{2U}{\rho} F_x \right) dY \quad (3.20)$$

In the first term of the LHS of Equation 3.20, the dissipation rate can be recognized. The second term vanishes due to the no-slip condition at the wall, and the absence of shear stress at $Y \rightarrow \infty$. The energy thickness is recognized in the first RHS term where the order of derivation and integration has again been changed. Use is made of boundary conditions to treat the second term on the RHS. Wall-normal velocities are again considered to be zero. This ultimately yields the Integral Energy Boundary Layer Equation.

$$\frac{2D}{\rho} = \frac{\partial}{\partial X} (U_e^3 \delta_3) + \int_0^\infty \left(\frac{2U}{\rho} F_x \right) dY \quad (3.21)$$

To make the Integral Energy Equation non-dimensional, Equation 3.21 is divided by U_e^3 which easily reveals the dissipation coefficient on the LHS and the suction term on the RHS. The remaining term on the RHS (not the force term) needs more work to be written in H_{32} and U_e derivatives only. The term $\frac{\partial}{\partial X} (U_e^3 \delta_3)$ is troubling in particular. Performing the differentiation to get rid of the exponent, a $\frac{\partial \delta_3}{\partial X}$ -term appears. By working out $\frac{\partial H_{32}}{\partial X} = \frac{\partial}{\partial X} \left(\frac{\delta_3}{\delta_2} \right)$, it can be replaced with a sum of derivatives in H_{32} and δ_2 . To get rid of the $\frac{\partial \delta_2}{\partial X}$ term, a look is taken at the Integral Momentum Equation, which provides a relation between $\frac{\partial \delta_2}{\partial X}$ and $\frac{\partial U_e}{\partial X}$. This is then paired with the expression for $\frac{\partial \delta_3}{\partial X}$ and thereafter introduced in the energy equation. Regrouping and reordering for integration then results in the non-dimensional Integral Energy Boundary Layer Equation:

$$\frac{\partial H_{32}}{\partial x} = \frac{2C_D}{\theta} - \frac{H_{32}}{\theta} \frac{C_f}{2} + (H_{12} - 1) \frac{H_{32}}{u_e} \frac{\partial u_e}{\partial x} + \frac{1}{\theta} \left(H_{32} \int_0^\infty \left(\frac{F_x}{\rho U_e^2} \right) dY - \int_0^\infty \left(\frac{2F_x U}{\rho U_e^2 U_e} \right) dY \right) \quad (3.22)$$

Plasma force term

With the general form of the integral boundary layer equations established in the previous chapter, the attention can be focused. The work in this section relies on what has been done by de Oliveira and Pereira [17]. Plasma-specific force coefficients are defined and elaborated upon. After reconsidering the characteristics of the plasma force field, an additional coefficient for closure is found.

4.1 Plasma force coefficients

From the Von Karman integral momentum equation, it can be found that the plasma body force field term appears as shown in Equation 4.1. It has not been treated up to now.

$$\int_0^\infty \left(\frac{F_x}{\rho U_e^2} \right) dY \quad (4.1)$$

It is dimensionless and can be rewritten using the adimensional quantities derived earlier, while keeping in mind that generally $U_e \neq U_\infty$ since the velocity profile in the boundary layer matches the free-stream value asymptotically.

$$\int_0^\infty \left(\frac{F_x}{\rho U_e^2} \right) dY = \int_0^\infty \left(\frac{1}{\left(\frac{U_e^2}{U_\infty^2}\right)} \frac{\left(\frac{1}{2}\right)}{\left(\frac{1}{2}\right)} \frac{F_x}{\rho U_\infty^2} \right) dY = \frac{1}{2u_e^2} \int_0^\infty \left(\frac{F_x}{\frac{1}{2}\rho U_\infty^2} \right) dY \quad (4.2)$$

The force momentum coefficient C_{FM} can be defined as follows:

$$C_{FM} = \int_0^\infty \left(\frac{F_x}{\frac{1}{2}\rho U_\infty^2} \right) dY \quad \rightarrow \quad \int_0^\infty \left(\frac{F_x}{\rho U_e^2} \right) dY = \frac{C_{FM}}{2u_e^2} \quad (4.3)$$

The non-dimensional Integral Momentum Equation can therefore be written with the new-found coefficient (without losing generality):

$$\frac{C_f}{2} = (H_{12} + 2) \frac{\theta}{u_e} \frac{\partial u_e}{\partial x} + \frac{\partial \theta}{\partial x} - \frac{v_0}{u_e} + \frac{C_{FM}}{2u_e^2} \quad (4.4)$$

Due to the algebraic trick of introducing the Integral Momentum Equation into the Integral Energy Equation to get rid of the $\frac{\partial \delta_2}{\partial X}$ term, the force term appears twice for the Energy Shape Factor equation.

$$H_{32} \int_0^\infty \left(\frac{F_x}{\rho U_e^2} \right) dY - \int_0^\infty \left(\frac{2F_x U}{\rho U_e^2 U_e} \right) dY \quad (4.5)$$

It can be readily seen that the first term is the same as in the momentum equation and can be substituted by the term containing the force moment coefficient C_{FM} . Making use of the adimensional velocities, the second term can be rewritten to define the force energy coefficient C_{FE} .

$$\int_0^\infty \left(\frac{2F_x U}{\rho U_e^2 U_e} \right) dY = \int_0^\infty \left(\frac{1}{\left(\frac{U_e^2}{U_\infty^2} \right) \frac{1}{2} \rho U_\infty^2} \frac{F_x}{\left(\frac{U}{U_\infty} \right)} \right) dY = \frac{1}{u_e^3} \int_0^\infty \left(\frac{F_x}{\frac{1}{2} \rho U_\infty^2} u \right) dY \quad (4.6)$$

$$C_{FE} = \int_0^\infty \left(\frac{F_x}{\frac{1}{2} \rho U_\infty^2} u \right) dY \rightarrow \int_0^\infty \left(\frac{2F_x U}{\rho U_e^2 U_e} \right) dY = \frac{C_{FE}}{u_e^3} \quad (4.7)$$

The Integral Energy Equation can then be written including the plasma coefficients:

$$\frac{\partial H_{32}}{\partial x} = \frac{2C_D}{\theta} - \frac{H_{32} C_f}{\theta} \frac{1}{2} + (H_{12} - 1) \frac{H_{32}}{u_e} \frac{\partial u_e}{\partial x} - \frac{1}{\theta} (H_{32} - 1) \frac{v_0}{u_e} + \frac{1}{\theta} \left(H_{32} \frac{C_{FM}}{2u_e^2} - \frac{C_{FE}}{u_e^3} \right) \quad (4.8)$$

The plasma force terms of the Energy Shape Equation thus become:

$$H_{32} \frac{C_{FM}}{2u_e^2} - \frac{C_{FE}}{u_e^3} \quad (4.9)$$

4.1.1 Physical meaning

The physical meaning of these coefficients is interpreted next. The Force Momentum Coefficient C_{FM} is a local property and independent of the boundary layer state. It relates the plasma force field with the boundary layer momentum deficit. The Force Energy Coefficient is an indication of the influence by the plasma force field on the growth of the boundary layer energy deficit θ^* and depends on both the plasma force field and the velocity profile at the point of actuation. The non-dimensional coefficients lend themselves well to provide a formulation of the integral boundary layer equations which can be evaluated numerically.

4.2 Plasma force field

In the light of the Integral Boundary Layer Equations and the plasma specific terms, another look is taken at the representation of the plasma force field itself. To incorporate this into the Integral Boundary Layer Equations rather than the NS or RANS, a phenomenological approach considering the shape of the body force density field is taken. The plasma field has nearly (semi-)elliptical equivalent force fieldlines [8].

4.2.1 Characteristics

To describe the plasma force field exerted on the flow by a single DBD plasma actuator, the following (dimensional) characteristics will be used:

- The total force exerted by the actuator per unit span F_T^p
- The thickness of the force field T^p
- The length of the force field L^p
- The starting location of the force field X_0^p
- A geometric weighting function describing the force field's shape

Important to note is that the plasma force field shape is a property of the actuator (in a certain operation mode) itself and is reasonably independent of the flow field [8].

The length and starting distance of the force field are made non-dimensional with the longitudinal length scale L . The thickness however is another matter. The energy balance is driven by the ratio of force field thickness over boundary layer thickness. It is a metric quantifying the extent of the boundary layer that is affected by the presence of the plasma force field. The scaling of the thickness is therefore critical.

$$\bar{t}^p = \frac{T^p}{\delta} = \frac{t^p}{\bar{\delta}} \quad \text{with} \quad t^p = \frac{T^p}{L} \quad \text{and} \quad \bar{\delta} = \frac{\delta}{L} \quad (4.10)$$

The variable $\bar{\delta}$ is the non-dimensional boundary layer thickness, while t^p is an intermediate step in the scaling of the thickness in the normal direction, \bar{t}^p . The boundary layer thickness can be expressed in terms of the shape factor H_{12} and the momentum thickness by making use of Head's shape factor H_1 :

$$H_1 = \frac{\bar{\delta} - \delta^*}{\theta} = \frac{\bar{\delta}}{\theta} - H_{12} \quad (4.11)$$

The difficulty of exactly determining the boundary layer thickness δ is circumvented by expressing the adimensional plasma field thickness as follows:

$$\bar{t}^p = \frac{T^p}{\delta_2(H_1 + H_{12})} = \frac{t^p}{\theta(H_1 + H_{12})} \quad (4.12)$$

4.2.2 Force field topology

The total force exerted by the actuator on the flow can be defined more precisely as the integral over the force field length and force field thickness, which is the area of actuation of F_x . The average dimensional density of the plasma force field ϕ^p can be written as Equation 4.13, with all variables independent of (X, Y) .

$$\phi^p = \frac{\int_{X_0^p}^{X_0^p+L^p} \int_0^{T^p} (F_x) dY dX}{\int_{X_0^p}^{X_0^p+L^p} \int_0^{T^p} dY dX} = \frac{F_T^p}{L^p T^p} \quad (4.13)$$

The force field density is expressed in terms of weighting functions for the longitudinal coordinate w^x and normal coordinate w^y , where the isolines of the force field are represented by semi-ellipses. The weighting functions as chosen by [17] are:

$$w_{(x,x_0,a)}^x = \begin{cases} \frac{\pi}{2} \sin\left(\frac{\pi(x-x_0)}{a}\right) & \left(\frac{x-x_0}{a}\right) \in [0, 1] \\ 0 & \text{else} \end{cases} \quad (4.14)$$

$$w_{(y,b)}^y = \begin{cases} \frac{\pi}{2} \sin\left(\pi\left(\frac{y}{2b} + \frac{1}{2}\right)\right) & \left(\frac{y}{b}\right) \in [0, 1] \\ 0 & \text{else} \end{cases} \quad (4.15)$$

These fulfil the condition that they have unit length integrals over a broad class of paths by obeying the following identities:

$$w_{(x,x_0,a)}^x = w_{\left(\frac{x}{c}, \frac{x_0}{c}, \frac{a}{c}\right)}^x \quad \forall y, a, c \in \mathbb{R} \quad (4.16)$$

$$w_{(y,b)}^y = w_{\left(\frac{y}{c}, \frac{b}{c}\right)}^y \quad \forall y, b, c \in \mathbb{R} \quad (4.17)$$

The integral properties are shown for the dimensional case but also hold for when non-dimensional quantities are used.

$$\int_{X_0^p}^{X_0^p+L^p} w_{(X,X_0^p,L^p)}^x dX = L^p \quad \forall L^p, X_0^p \in \mathbb{R} \quad (4.18)$$

$$\int_0^{T^p} w_{(Y,T^p)}^y dX = T^p \quad \forall T^p \in \mathbb{R} \quad (4.19)$$

Combining the average field density and the weighting functions, and making use of distributive property and independence of variables, the total plasma actuator force can be expressed as:

$$\int_{X_0^p}^{X_0^p+L^p} \int_0^{T^p} \phi_x^p w_{(Y,T^p)}^y w_{(X,X_0^p,a)}^x dY dX = \phi_x^p T^p L^p = F_T^p \quad (4.20)$$

From the previous equation, it is clear that the field density can be written as shown in Equation 4.21, a result which can be used to simplify the plasma force coefficients.

$$F_x = \phi_x^p w_{(Y,T^p)}^y w_{(X,X_0^p,a)}^x \quad (4.21)$$

4.3 Plasma force coefficients revisited

It would be convenient to have the force coefficients defined earlier written in terms of the plasma characteristics. Equation 4.21 is introduced in the Plasma Force Momentum coefficient:

$$C_{FM} = \int_0^\infty \left(\frac{F_x}{\frac{1}{2}\rho U_\infty^2} \right) dY = \int_0^\infty \left(\frac{\phi_x^p w_{(Y,T^p)}^y w_{(X,X_0^p,L^p)}^x}{\frac{1}{2}\rho U_\infty^2} \right) dY \quad (4.22)$$

Considering that all terms except the weighing function in the normal direction are independent of Y , these can be taken outside of the integration. Taking into account Equation 4.19 to evaluate the remaining integral yields:

$$C_{FM} = w_{(X, X_0^p, L^p)}^x \left(\frac{\phi_x^p}{\frac{1}{2}\rho U_\infty^2} \right) T^p = w_{(X, X_0^p, L^p)}^x \left(\frac{\phi_x^p T^p}{\frac{1}{2}\rho U_\infty^2} \right) = w_{(x, x_0^p, l^p)}^x C_{\phi_x^p} \quad (4.23)$$

In the previous equation, $C_{\phi_x^p}$ is the average force momentum coefficient and is independent of the spatial coordinates. It is a property of the plasma actuator (unlike the Force Momentum Coefficient) and is defined as:

$$C_{\phi_x^p} = \frac{\phi_x^p T^p}{\frac{1}{2}\rho U_\infty^2} \quad (4.24)$$

The force energy coefficient is more difficult to rework, since also the boundary layer speed profile is of importance. Initially, the same steps as for the momentum counterpart are taken. This results in the following expression:

$$C_{FE} = w_{(X, X_0^p, L^p)}^x C_{\phi_x^p} \int_0^\infty \left(\frac{w_{(Y, T^p)u}^y}{T^p} \right) dY \quad (4.25)$$

The integral term is approached in a way such that a new closure relation can readily be formed to solve later on. With the authors' choice on the use of the Swafford profile family, a scaling of the normal coordinate with momentum thickness arises. This is done with $\eta = \frac{Y}{\delta_2}$, filled into the integral. Rearranging the terms, the Momentum Scaled Plasma Thickness becomes apparent:

$$\int_0^\infty \left(\frac{w_{(Y, T^p)u}^y}{T^p} \right) dY = \int_0^\infty \left(\frac{w_{(\eta, t_\theta^p)u}^y}{\left(\frac{T^p}{L}\right)} \right) d\eta \quad \rightarrow \quad t_\theta^p = \frac{T^p}{\delta_2} = \frac{\left(\frac{T^p}{L}\right)}{\theta} = \frac{t^p}{\theta} \quad (4.26)$$

The integral in Equation 4.26 can be written in terms of adimensional groups. This allows the force energy coefficient to be expressed in a convenient form, where C_{EI} is the Energy Interaction Coefficient:

$$C_{FE} = w_{(X, X_0^p, a)}^x C_{\theta_x^p} \int_0^{t_\theta^p} \left(\frac{w_{(\eta, t_\theta^p)u}^y}{t_\theta^p} \right) d\eta = w_{(X, X_0^p, a)}^x C_{\theta_x^p} C_{EI} \quad (4.27)$$

4.4 Energy Interaction Coefficient

The coefficient appearing in Equation 4.27 is the Energy Interaction Coefficient C_{EI} . The parameter drives the effect of the plasma on the energy of the boundary layer, and hence shape factors. A interesting feature regarding the possibility of a closure relation is the fact that C_{EI} does not depend explicitly on x .

$$C_{EI} = \int_0^{t_\theta^p} \left(\frac{w_{(\eta, t_\theta^p)u}^y}{t_\theta^p} \right) d\eta \quad (4.28)$$

The Energy Interaction Coefficient C_{EI} is the convolution integral of the plasma force field normal weighting function with the boundary layer velocity profile and is a function of H , Re_θ and t_θ^p . The velocity profile of the boundary layer which dominates the integrand can be estimated from experimental data or quasi-analytical profile families (here: Swafford profiles). The latter option is considered first by the de Oliveira and Pereira.

The integral is evaluated over a large range of conditions of the parameters and is used to create a closure in the form of $C_{EI} = f(H, Re_\theta, t_\theta^p)$. To generate the closure dataset, evaluations of the coefficient with 100 equally spaced steps for each of the three variables were performed with the ranges:

- Shape factor H from 1.4 to 8
- Momentum thickness Reynolds number Re_θ from 500 to 5000
- Momentum Scaled Plasma Thickness t_θ^p from 0 to 10

A visualization of the numerical closure data set is shown in Figure 4.1. Figure 4.2 shows the influence of the thickness of the plasma actuation. It can be seen that the thicker the plasma field is, the more the boundary layer energy is affected. Flows with low shape factors, which exhibit faster flow near the wall show larger energy alterations than flows with higher values of H .

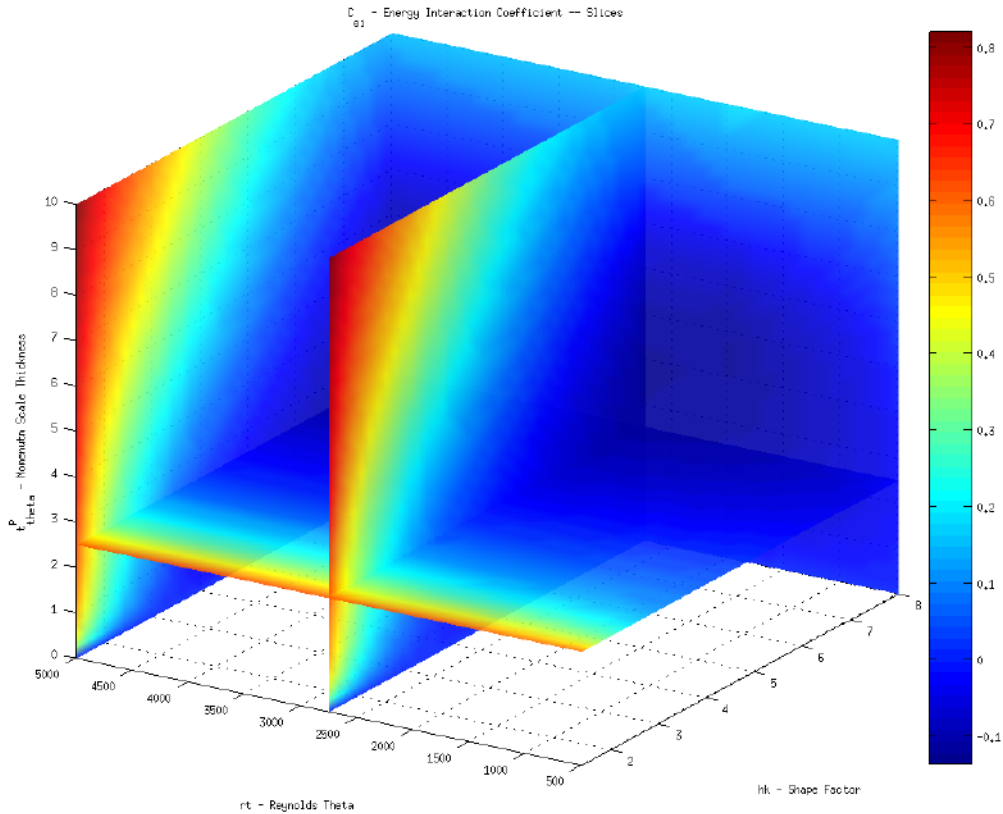


Figure 4.1: Slice of the numerical C_{EI} closure data set [17]

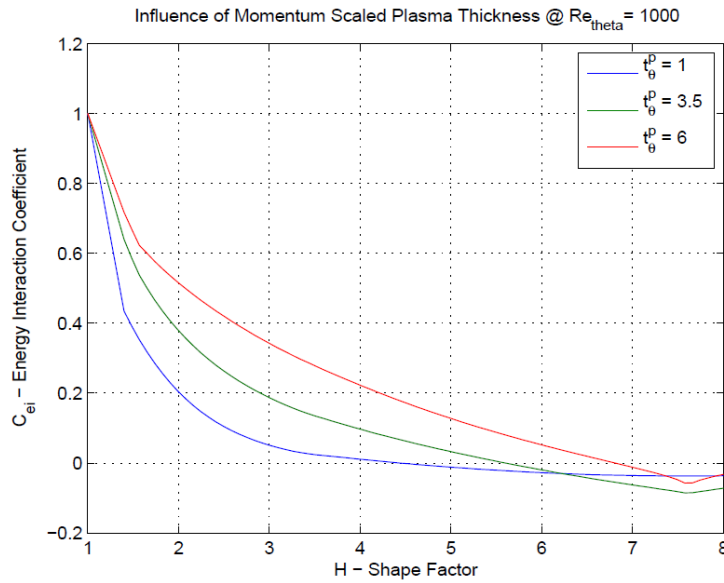


Figure 4.2: Influence of Plasma Force Field Thickness [17].

4.5 Energy interaction coefficient results

An experimental campaign was carried out by the authors of [26] in which the velocity field in proximity of two sets of DBD plasma actuators was captured with particle image velocimetry (PIV) over a range of operating conditions. The exact methodology and set-up can be found in the reference. A slice of the C_{EI} closure data set versus shape factor H is compared with experimentally obtained values in Figure 4.3. In general, the numerical approximation is within reasonable accuracy of the experimental data. However, a distinct offset for higher values of H can be noted, where the flow is closer to separation and the adverse pressure gradient is higher. Energy Interaction Coefficient predictions based on the Swafford profile exhibit negative values for larger shape factors, $H > [3.5, 4.5]$, while experimental estimates appear to remain positive for all measured separated flows. Such a disparity remains unexplained: it could be due to experimental limitations (insufficient resolution of the boundary layer measurements of [26]) or, more interestingly, highlight a region of uncertainty in the Swafford profile model

The evolution of the displacement and momentum thickness for the particular case of a DBD plasma actuator located at $x/c = 0.65$ at a velocity of $U = 20\text{m/s}$ and angle of attack $\alpha = 7^\circ$ is shown in Figure 4.4. The magnitude of the effect the actuator imparts on the flow is computed reasonably well downstream of the actuator, but in close vicinity its behaviour is not captured.

In the light of these discrepancies between the model formulation and the experimental observations of [26], attention is focused on the skin friction coefficient. A dedicated plasma-actuated treatment for the closure relation has not yet been applied, although effect of skin friction on plasma actuated flows has been reported to be significant [8]. A new experimental campaign needs to be conducted to observe the effect of the DBD plasma actuator on the skin friction explicitly.

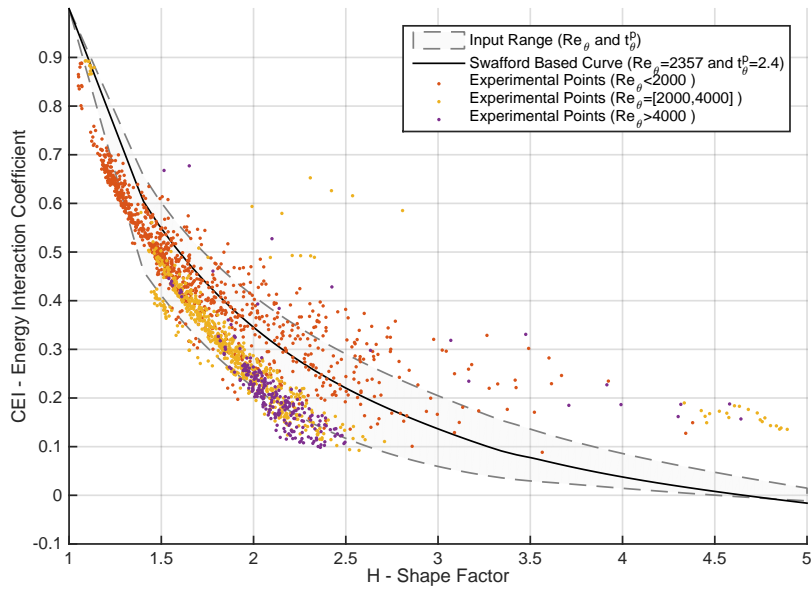


Figure 4.3: Energy Interaction Coefficient for numerical and experimental results

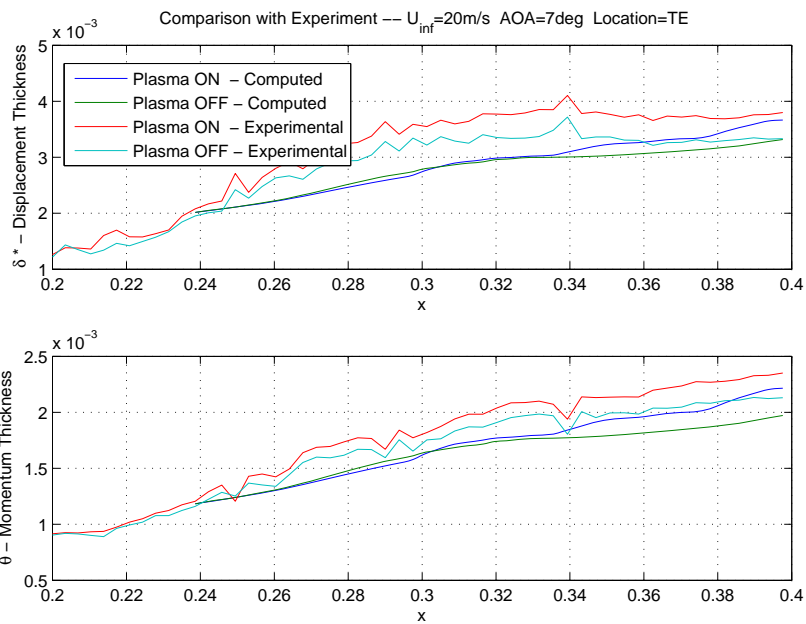


Figure 4.4: Evolution of the integral boundary layer for plasma actuator at $0.65 x/c$ at $U_\infty = 20m/s$ and $\alpha = 7^\circ$.

Part II

Experimental campaign

Design of experiment

The most conventional skin friction laws in turbulent flows rely at least partially on experimental data [40], which is why an experiment is set up in order to collect information about the velocity profiles in the boundary layer. The previous experiment of [26] did not resolve the velocity field near the airfoil surface in sufficient detail to form the basis of an adapted skin friction closure relation, justifying the present experimental campaign. It is aimed to measure the skin friction directly from the velocity profiles by means of detailed Particle Image Velocimetry (PIV) inside the turbulent boundary layer. The variation in skin friction due to DBD plasma actuation can consequently be determined. For the experiment, an existing airfoil model will be used. More details about the model are presented in section 6.2, but important for the following is the fact that two grooves are present to insert the actuators. These are centered around $\frac{x}{c} = 0.25$ and $\frac{x}{c} = 0.65$ and are referred to as front and back actuator location.

5.1 Resolution investigation required for PIV

To be able to extract the skin friction from experimental data, the velocity profiles should be well resolved as close to the wall as possible. A closer look is taken first at the characteristics of the turbulent boundary layer. As can be found in classical literature describing the turbulent boundary layer, Reynolds decomposition dictates a region close to the wall where shear stress τ is constant and equal to the wall shear stress τ_0 . Furthermore, it states that when the shear stress is constant across the depth of the flow, the so-called Law of the Wall is valid, relating the velocity distribution to be:

$$\frac{u}{U_f} = f(y^+) \quad (5.1)$$

In the above equation, use is made of the wall parameters friction velocity U_f and wall-

coordinate y^+ and kinematic viscosity ν :

$$U_f = \sqrt{\frac{\tau_0}{\rho}} \quad y^+ = \frac{y U_f}{\nu} \quad \nu = \frac{\mu}{\rho} \quad (5.2)$$

The total shear stress of a flow close to a smooth wall consists out of two parts: a viscous and turbulent part.

$$\tau = \mu \frac{du}{dy} + (-\rho \overline{u'v'}) \quad (5.3)$$

Very close to the wall, for small y^+ , the contribution of turbulence to the total shear stress is negligible compared to that of viscosity: $(-\rho \overline{u'v'}) \ll \mu \frac{du}{dy}$. Integration of Equation 5.3 and application of the no-slip condition states that the velocity varies linearly with the distance from the wall. Experimental results agree well with this for $y^+ < 5$. Beyond this height, the data begins to deviate from the analytical expression. The region is named *the viscous sublayer*.

For large values of y^+ , the viscous part of the total shear stress is small compared to the turbulent part. The high y^+ values considered are still small compared with the total height of the boundary layer and are still inside the constant stress layer. The viscosity is no longer a driving parameter for the shear stress or velocity variation and is dropped from the equation. The *logarithmic law* is found to be $\bar{u} = U_f(A \ln y^+ + B)$. In literature, A is found to be a universal constant equal to 2.5. The logarithmic law is usually valid from $y^+ = 30 - 70$ to an upper bound which is flow dependent. Usually, this is around $y/\delta \approx 0.1 - 0.2$. In between the viscous sublayer and the logarithmic layer, there is a matching buffer layer extending approximately between $5 < y^+ < 70$. The various layers are illustrated in Figure 7.2. By capturing as much data points in the lowest region of the constant stress layer as possible, the skin friction can be determined as the shear stress there can be assumed to equal the skin friction.

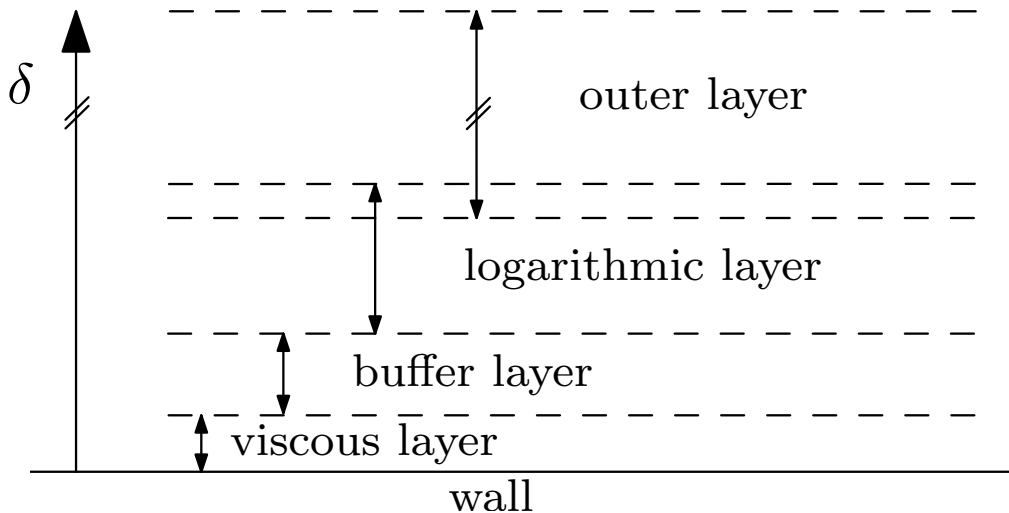


Figure 5.1: Flow regions in the turbulent boundary layer.

In order to discover trends for the variation in skin friction by DBD plasma actuation, a variety of boundary layer conditions is selected. The boundary layer state at the location

of the actuator was estimated using Xfoil over angles of attack ranging from -5° to 15° and for the free stream velocities of 10, 16 and 22 m/s. For each of these conditions, the y^+ per data point which can be acquired is calculated. The results can be seen in Figure 5.2.

For the envisioned PIV set-up, a magnification factor of 1 : 1.5 and final interrogation window size of 8x8 pixels is achievable and forms the basis of the current calculation. To reliably find the skin friction, an interrogation window size of 8x8 pixels is required especially for the higher flow speeds. Doubling the interrogation window size also doubles the distance in y^+ that is captured with each data point.

For all cases of the back actuator however, multiple points are captured within the lowest region of the constant stress layer. This provides confidence that the skin friction can be obtained for the experiment. The turbulent boundary layer has had more chance to develop further downstream. For the current case of flow over an airfoil with pressure gradient, this means an increase in shape factor H and thereby reducing the length of y^+ per data point that can be captured.

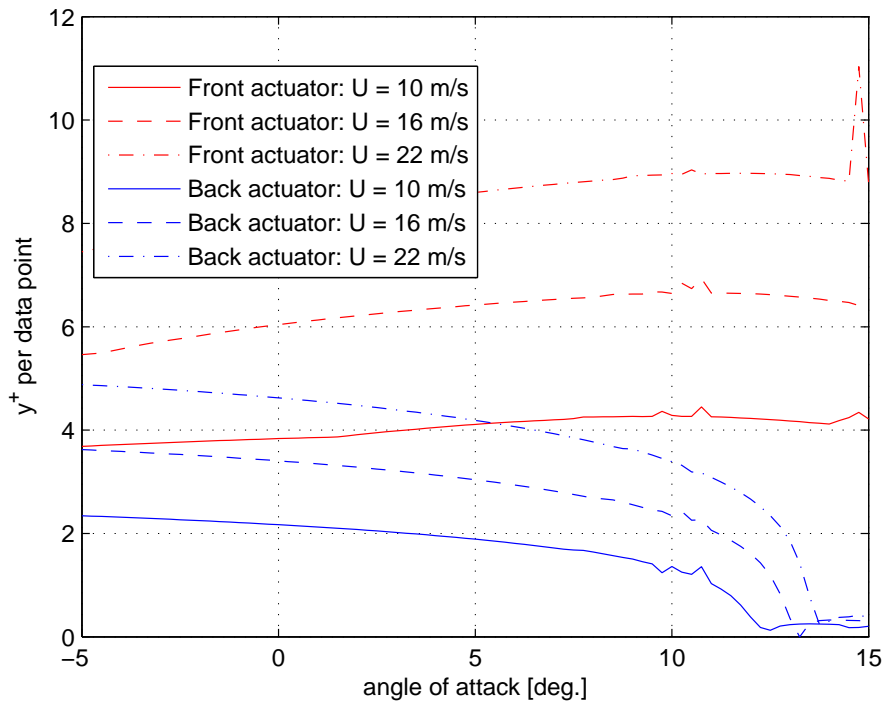


Figure 5.2: The y^+ distance per captured data point over angle of attack, for various free stream flow velocities and actuator locations.

5.2 Experimental test matrix

As mentioned before, the test points are selected to cover a broad variety of boundary layer conditions. The ranges of momentum scaled Reynolds number Re_θ , shape factor

H and momentum scaled plasma thickness t_θ^p for various angles of attack and freestream velocities are calculated in Rfoil. The results can be seen in Figure 5.3. As can be seen, a large scatter in Re_θ can be measured, whereas the variance of t_θ^p is significantly smaller. The shape factor varies from low values around 1.5 for fully attached flow, to rapidly increasing values at larger angles of attack where the flow is separating. The large spectrum of shape factors is particularly interesting with respect to a possible modification to the closure relations of the integral boundary layer formulation.

5.2.1 Front actuator

In the front actuator region, located around $\frac{x}{c} = 0.25$, the shape factor is nearly independent of the angle of attack. Momentum scaled Reynolds number displays moderate variations with angle of attack, but a significant interval (from 300 to 1500) can be covered if the free-stream speed is varied. Significant changes in momentum scaled plasma force field thickness are also observed. Study of this region can contribute to the modeling of plasma-actuated, attached turbulent boundary layers in mild adverse pressure gradients. For this type of flow, classic theoretical approaches are expected to hold and a modified law of wall accounting for plasma actuation might exist in a form similar to the one found by Atilla [41] for turbulent suction. Such a law would be compatible with a Coles wake function and provide a meaningful actuated profile family.

5.2.2 Back actuator

The back actuator region, located around $\frac{x}{c} = 0.65$, covers a wide interval of shape factors, ranging from fully attached to deeply separated flow. Emphasis is placed on separating flow, a range for which closure relations have a determinant role in the discrepancies observed in C_{EI} (Figure 4.3) and skin friction coefficient behavior.

It is determined to measure at angles of attack $\alpha = [0^\circ, 7^\circ, 10^\circ, 13^\circ]$ and flow speeds of $U_\infty = [10\text{m/s}, 16\text{m/s}, 22\text{m/s}]$ to capture the trends in skin friction difference from a fully attached to a fully separated turbulent boundary layer.

5.3 PIV Camera optics

Since Particle Image Velocimetry will be used in the experimental campaign, the sizing of the experimental setup is determined partly by the optics required for the desired imaging.

The magnification ratio of 1 : 1.5 combined with the sensor size of the camera fixes the field-of-view (FOV) to 54x36 mm². The imaging distance d_i and object distance d_o can then be found as (with lens focal length $f = 200\text{mm}$):

$$M = \frac{d_i}{d_o} \approx 0.667$$

$$\frac{1}{f} = \frac{1}{d_i} + \frac{1}{d_o} \quad \rightarrow \quad d_o = 0.5 \quad , \quad d_i = 0.333$$

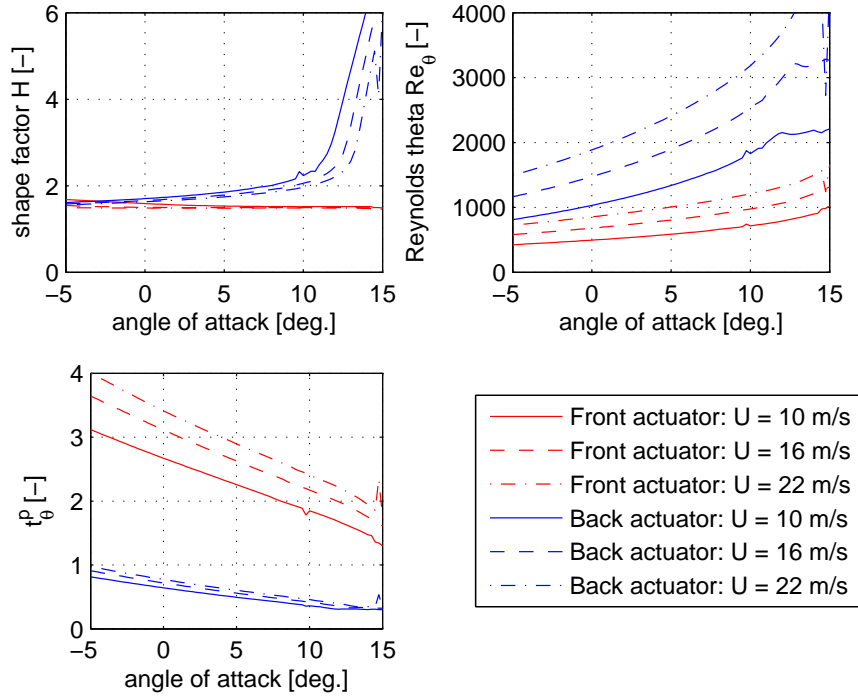


Figure 5.3: Range of experimental parameters for front and back actuator regions.

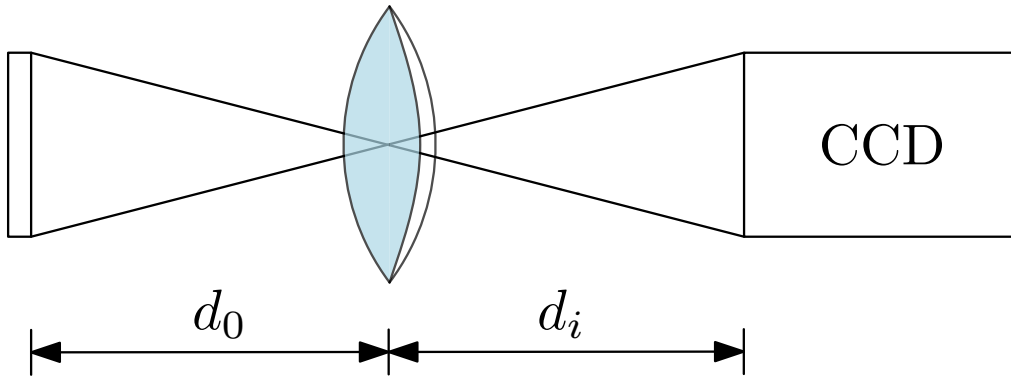


Figure 5.4: Object distance d_o and imaging distance d_i for the CCD camera setup.

The location of the camera in the practical setup is determined by the object distance. The correct imaging distance can be obtained through the use of extension rings between the lens and the camera. Achieving the predetermined magnification is crucial in ultimately finding the skin friction coefficient. Besides the geometrical constraints of the camera, as seen in Figure 5.4, also the relative aperture or f-stop of the camera can be calculated. The $f_{\#}$ is a measure of the amount of light which is allowed to pass through to the sensor. The higher this number, the darker the images are. It is determined through the minimum particle image diameter, which is twice the pixel size. Diffraction limits then require the

f-stop to be (where $\lambda = 532\text{nm}$ is the wavelength of the green laser light):

$$f_{\#} \geq \frac{2 \cdot \text{pixelsize}}{2.44 \lambda (1 + M)} \approx 6.84 \quad (5.4)$$

Experimental setup

Details on the experiment which has been carried out are disclosed below. These cover information about the flow facility, the model which is used and the PIV setup to acquire and process the velocity field data. To conclude, the main characteristics of the tested DBD plasma actuators are elaborated upon.

6.1 Flow facility

The experiments are conducted in the closed-circuit Open Jet Facility (OJF) at the Aerospace Department of TU Delft. The octagonal cross-section of the outlet measures 2.85 m by 2.85 m and releases flow free to expand in a test section of 13.7 m by 6.6 m by 8.2 m. The contraction ratio is 3 : 1. A 500 kW electric motor drives a fan with a 3.5 m diameter, which allows free stream flow velocities in the test section of up to 35 m/s at a turbulence level of 0.24 %. The added heat to the flow is removed through a 350 kW radiator system. For the current experiment, three different free-stream velocities are investigated, namely $U = 10$ m/s, $U = 16$ m/s and $U = 22$ m/s. Initially, the three velocity settings would have been $U = 10$ m/s, $U = 20$ m/s and $U = 30$ m/s, but after preliminary testing, it was noted that wind tunnel did not reach over 28.5 m/s, and the additional heat (despite the cooling system) at those speeds were detrimental for smoke particles.

6.2 Model setup

As the OJF is used, a dedicated support structure needed to be designed. The airfoil model was originally designed to be used in the Low Turbulence Tunnel at TU Delft, in a previous experimental campaign [26]. The construction is required to position the model in the flow as well as leaving enough room to fit the acquisition equipment. An exploded view is shown in Figure 6.1. After the design was made, it was sent to the

DEMO workshop at the Aerospace Engineering Faculty at TU Delft, who produced it. The airfoil model is placed vertically into the flow. The load is carried through a steel support member on a circular base. Rotation of the base allows for variation in the angle of attack. The base is then fixed into position by screwing it to the floor. The table, which was mounted flush with the wind tunnel outlet is made out of wood and does not carry loads. The height is specified to be 90cm to give enough clearance for the lens, camera and traversing system. A circular cut-out is made around the location of the model, and replaced with a Plexiglas disk. As such the camera can be placed below the model, outside of the flow. Care was taken during installation to make sure no scratches or deformations due to concentrated loads developed to reduce the chance of light distortions. A splitter plate is added to the free end of the model to approximate two-dimensional flow. The plate is circular to ensure no change in loading when changing the angle of attack of the model. The matte black paint minimizes reflections. Natural frequencies of the complete system were checked to avoid resonance and vibration issues.

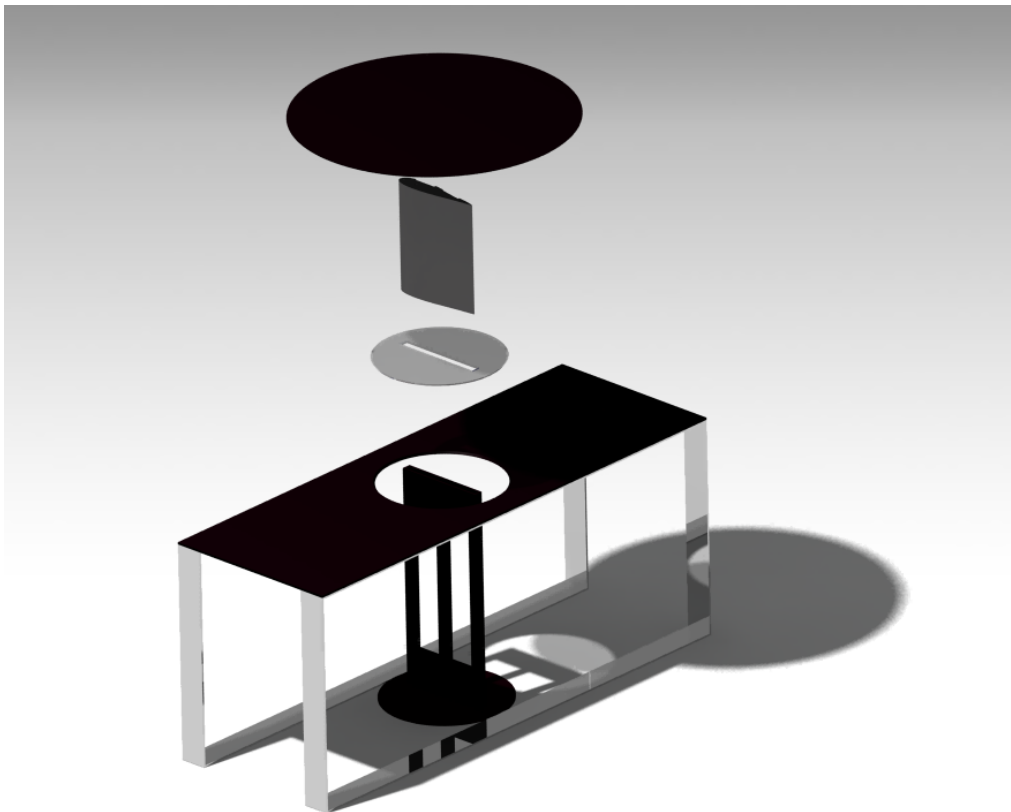


Figure 6.1: Exploded view of the dedicated support structure for the present experimental campaign showing splitter plate, airfoil model, circular Plexiglas insert, table and support structure.

6.3 Airfoil model

The profile of the airfoil model is designed by a multi-objective airfoil optimizer [42]. Although the optimizer was developed for transpiration, plasma effects were included through equivalence of the variation in boundary layer momentum [26]. The resulting airfoil optimized for actuation can be seen in Figure 6.2.

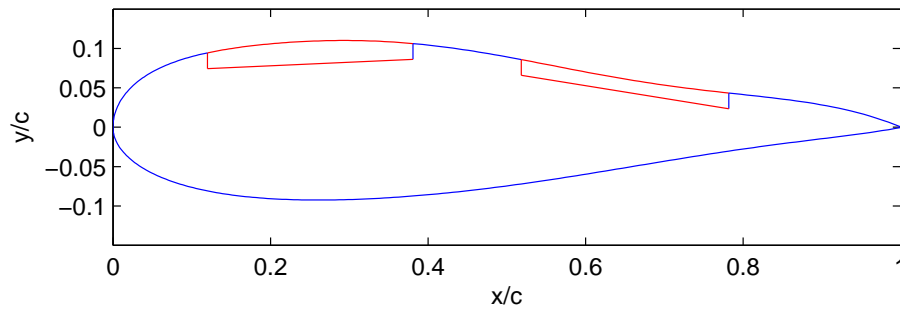


Figure 6.2: Airfoil section of the experimental model with two inserts for plasma actuation around $\frac{x}{c} = 0.25$ and $\frac{x}{c} = 0.65$.

The airfoil design is typical for application in stall controlled horizontal axis wind turbines. The relative thickness is 21 % with aerodynamic performance similar to wind energy airfoils of the same thickness. The chord c of the model used in the experiment is 0.5 m and the span L is 0.6 m, yielding Reynolds numbers between approximately 330,000 and 730,000. Two inserts are present on the suction side which are 130 mm wide in the stream-wise direction and cover the complete span. These are centered around $\frac{x}{c} = 0.25$ and $\frac{x}{c} = 0.65$ and are made out of Plexiglas (Figure 6.2). For the experiment, actuation was applied to the most downstream insert only. Due to circumstances beyond the control of the author, the time in the wind tunnel was cut short. The campaign for the front actuator could therefore not be executed. Zigzag tape was added on the upper surface at $\frac{x}{c} = 0.10$ to trigger transition into turbulent flow.

6.4 Plasma actuator

The DBD plasma actuators are mounted in the co-flow direction on the center of the 3 mm thick Plexiglas inserts at $\frac{x}{c} = 0.65$. The insert acts as the dielectric barrier and both the exposed and covered electrode are made out of self-adhesive copper tape of respectively 10 and 25 mm wide. The width of the grounded electrode is such that the plasma is free to fully develop without dimensional constraints. The copper tape is 60 μm thick, and the electrodes are fixed such that there is no horizontal gap between both present.

To prevent undesirable plasma formation outside the region of interest (above the covered electrode), 50 μm Kapton tape is applied at the outer edges of the electrodes. The actuator is powered by a TREK 20/20C High Voltage amplifier (± 20 kV, ± 20 mA), imposing a 40 kV_{pp} amplitude, 900 Hz square-wave signal.

The mounted airfoil model with the two inserts accommodating one DBD plasma actuator

each is shown in 6.6a. The complete set-up with the PIV laser on the left and high voltage amplifier in the middle is seen in 6.6b.

From past experiments, such as those of Jiawei Si *et al.* who used a setup with 12 kV peak-to-peak with a carrier frequency from 10 kHz to 50 kHz, approximately 5 seconds are needed for the power supply to start and stabilise. Nearly 10 seconds are needed for the flow to become steady, so the plasma actuator operates around 15 seconds before PIV acquisition is done.

6.5 Particle Image Velocimetry setup

The planar PIV measurements are carried out using a Quantel Evergreen laser and 16 Megapixel LaVision Pro LX CCD camera. The sensor resolution of the camera is 4872×3246 pixels with a pixel pitch of $7.4 \mu\text{m}$.

A 200 mm Nikon Macro lens was used along with extension rings (one of 20 mm, one of 36 mm) to obtain a magnification of $1 : 1.5 = 0.67$ at f-stop of 16 during acquisition. The field-of-view which was measured was $54 \times 36 \text{mm}^2$

Light pulse separation times δt were found through the rule of thumb Equation 6.1 and were $20 \mu\text{s}$, 15 and 10 for $U=10,16,22 \text{ m/s}$ respectively.

$$\delta t = \frac{\text{window size} \cdot \text{pixel size}}{4 U_{\infty} M} \quad (6.1)$$

The velocity field at the chordwise location of the plasma actuators are measured mid-span of the airfoil model. Seeding of the flow is performed with smoke of $10 \mu\text{m}$ particles produced by a Safex Twin Fog Generator. Particles are electrically neutral so whatever charge they might undergo, it will be small and averaged out. The charge on the droplets resulting from their shear-dominated formation in the atomizer is at most a few hundred electrons. Dimensional reasoning shows that even for the maximum electric field encountered in the experiments, the aerodynamic force on the droplets dominates.

A benchmark run was performed at $\alpha = 7^\circ$ and $U_{\infty} = 11.2 \text{m/s}$ where 450 image pairs were acquired. Six locations are selected, in various parts of the boundary layer to serve as evaluation points. These points are (5,-22), (5,0), (40,-25), (40,-12), (22.5,-20) and (22.5,-12), and are shown in Figure 6.3. The offset of the cumulative averages to the average over 450 image pairs is shown in Figure 6.4. It can be seen to decrease steadily until around 150 image pairs, from where on the offset is more or less constant. The actual value of the local velocity components is shown in Figure 6.5. For each of the considered configurations, 150 image pairs are captured. The average of these serves as the relevant flow, in order to minimize the effect of phenomena such as turbulence and velocity oscillations due to separation. Since the case at angles of attack of 0° were deemed the most important, 300 image pairs were acquired for these runs.

6.6 Processing

The evaluation of the particle image motion is performed with DaVis 8 LaVision software. The cross-correlating processing starts with 64×64 windows to arrive at interrogation

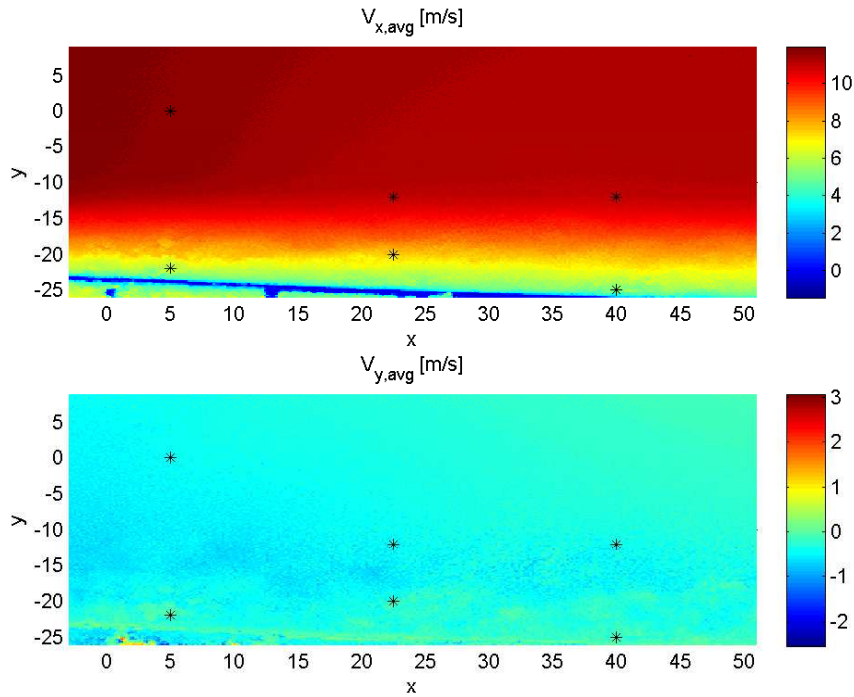


Figure 6.3: Average velocity fields $V_{x,avg}$ and $V_{y,avg}$ for the benchmark run of 450 image pairs with the six points of evaluation marked by ''.*

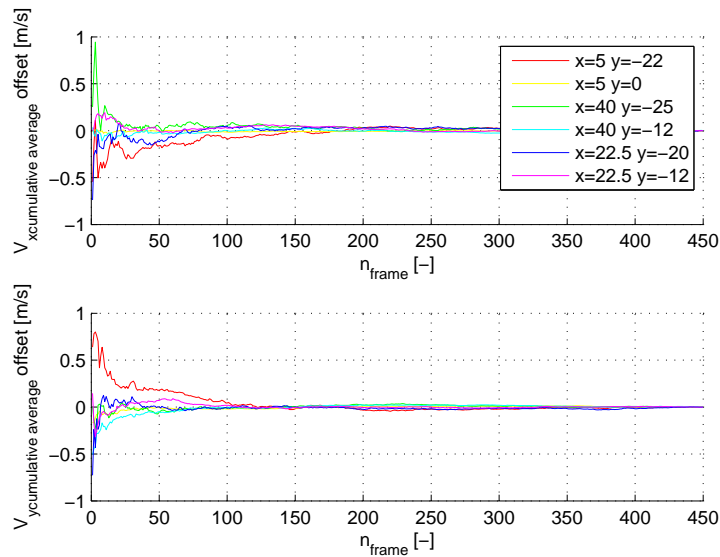


Figure 6.4: Offset in local average velocity for $V_{x,avg}$ and $V_{y,avg}$ over accumulating amount of image pairs.

window sizes of 8×8 after several passes. Aspect ratio in wall normal direction of 3 : 1 and an overlap of 50% is used to obtain higher spatial resolution. Ultimately, the velocity vector grid is given with a resolution of 24 vectors per mm. An analysis was done on the

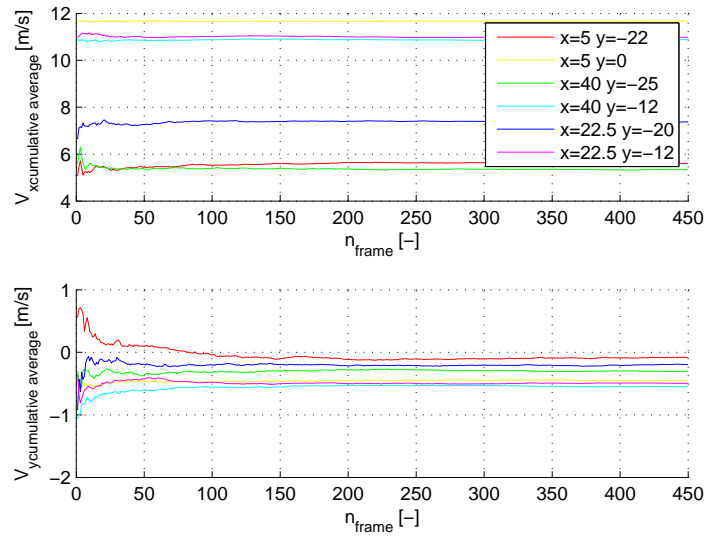


Figure 6.5: Local average velocity value for $V_{x,\text{avg}}$ and $V_{y,\text{avg}}$ over accumulating amount of image pairs.

interrogation window size, by looking at a test case processed with 32×32 , 24×24 , 16×16 , 12×12 and 8×8 windows. Although it was seen that the amount of erroneous vectors in the instantaneous velocity fields increased as interrogation window sizes decreased, the average over the 150 image pairs showed no significant differences. As this is the main concern of the research, a final interrogation window of 8×8 pixels is deemed trustworthy.



(a) Airfoil model with installed DBD plasma actuators used during experimental campaign.



(b) Complete set-up including PIV arrangement, HV amplifier, airfoil model and splitter plate used during experimental campaign.

Figure 6.6: Airfoil model and set-up of the experimental campaign.

Experimental results

The averaged velocity fields outputted by the DaVis software are further post-processed in MATLAB. The methodology to get to the skin friction value is elaborated using the example of the actuator OFF case of A0U10. Afterwards, the complete experimentally obtained set of data is analyzed critically and the satisfactory cases for further modelling are selected. The chapter is concluded by an analysis of the latter datasets to greater extent.

7.1 Post-processing methodology

The post-processing consists of three major steps. From the acquired velocity fields of the PIV software, the location of the wall needs to be determined. Once this is done, the velocity profile at each point can be retrieved in the frame of reference from the local boundary layer. Finally, the skin friction coefficient representative of the experimental case can be extracted.

7.1.1 Finding the wall

From the PIV image cross-correlation, the averaged velocity fields V_x and V_y (seen in Figure 7.1), standard deviations of velocities fields and normal Reynolds stresses fields Re_{xx} and Re_{yy} are obtained. They are given in x - & y -directions in the frame of reference of the camera. It should be noted that the origin of the PIV x -coordinates corresponds to the location of the horizontal gap between the covered and exposed electrode of the actuator. The start of the plasma region can therefore be assumed to be at this point. Negative values of the x -coordinate are therefore associated with the region upstream of the actuation, positive x -coordinates with the downstream region. Despite meticulous installation, the edge of the exposed electrode is seen to introduce a local roughness at $x = 0$. The flow is locally slowed down due to the uncovered edge. This underscores the difficulty of having a flush surface with actuators present.

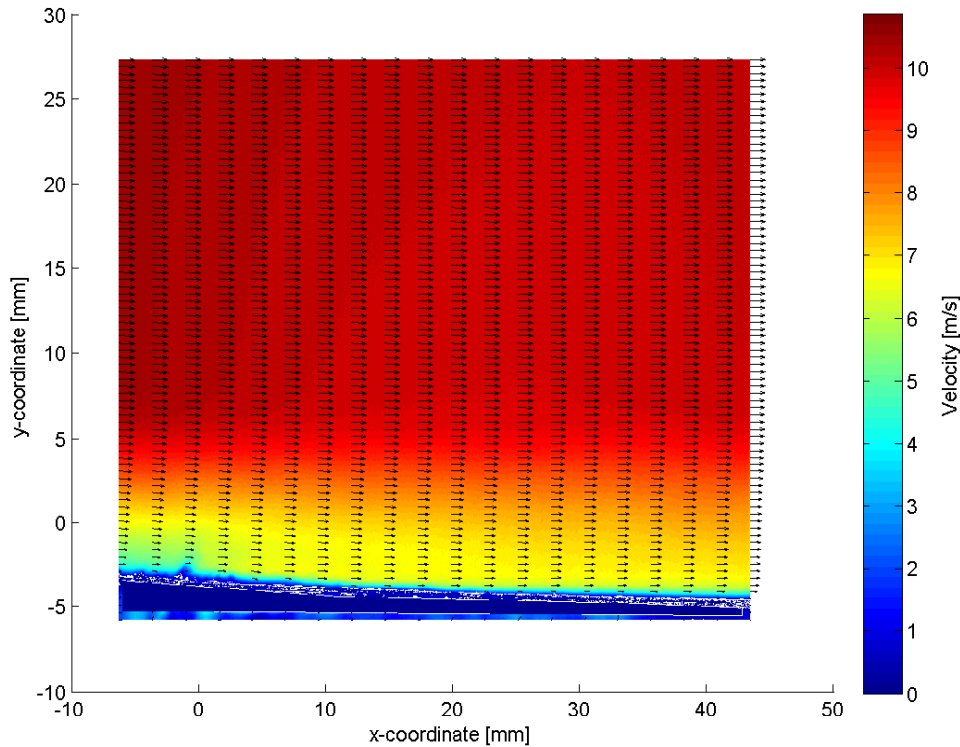


Figure 7.1: Average velocity fields of V_x and V_y in PIV frame of reference (quiver resolution is reduced for illustration purposes).

Before the velocity parallel to the wall can be found, first the wall itself should be found. This is not as simple as it sounds due to the high resolution near the wall. Reflections or impurities on the Plexiglas insert might have obscured the clear edge of the surface, causing the cross-correlation algorithm of DaVis to produce faulty velocity vectors locally.

Finding the wall by the condition that the local velocity should equal zero proved to be unreliable due to the imperfections described above. It was found that setting a threshold value for the standard deviation of V_y gives the most satisfactory results. The wall as extracted from the experimental PIV data is seen as the red line in Figure 7.3.

To obtain the smooth edge, the coordinate file of the airfoil profile is used. Since the location of the 0 in the experimental files corresponds to an $\frac{x}{c}$ -location of 0.65, the extent of the upper surface captured by the PIV can easily be extracted from the coordinates. As the x-axis of the camera was not aligned perfectly with the chord of the airfoil model, the airfoil edge should still be matched to the PIV edge. The experimentally found wall is shown in red on Figure 7.3, and the airfoil (interpolated) airfoil coordinates in blue.

The airfoil edge is translated in x and y as well as rotated until the optimal fit is found. This is done by the `fminsearch` routine in MATLAB, minimizing the root-mean-square of the difference in y . The matched airfoil edge is adopted as the wall edge.

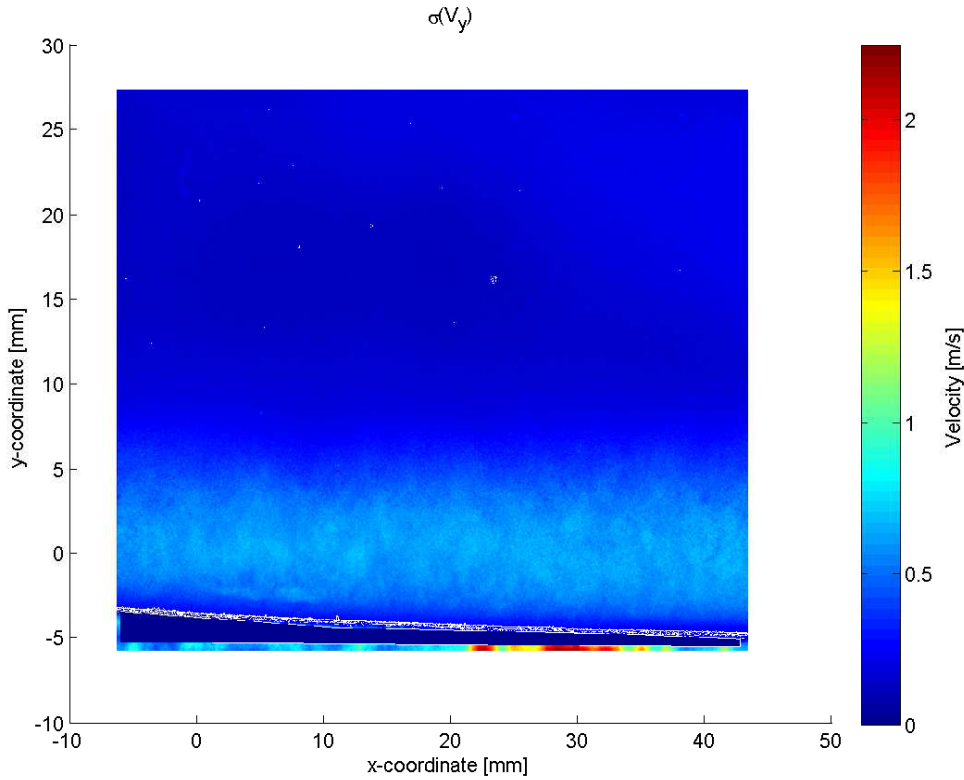


Figure 7.2: Standard deviation of V_y with the experimentally found edge.

7.1.2 Shift to boundary layer frame of reference

After having established the wall, the frame of reference can be recast to a boundary layer point of view. The normal vectors are calculated at each point of the surface. Through interpolation, the velocities in the direction parallel to the surface are obtained. This is shown for the example case in Figure 7.4. The edge velocity U_e , which is a measure for the pressure gradient, is found as the maximum value of the velocity profile at every x -location.

With the velocity field in the correct orientation and the edge velocity determined, the integral boundary layer quantities δ^* and θ can be calculated through trapezoidal integration. As can be seen in Figure 7.5, the influence of the actuator is captured as expected, as the quantities can be seen to decrease from actuator OFF to actuator ON case. The effect is relatively most outspoken in the displacement thickness.

7.1.3 Extracting representative skin friction coefficient

With the velocity profiles in the correct frame of reference, the gradient can be taken to obtain the shear stress profiles. The skin friction coefficient is found through:

$$c_f = \frac{\mu \left. \frac{dU}{dy} \right|_{y=0}}{\frac{1}{2} \rho U_\infty^2} \quad (7.1)$$

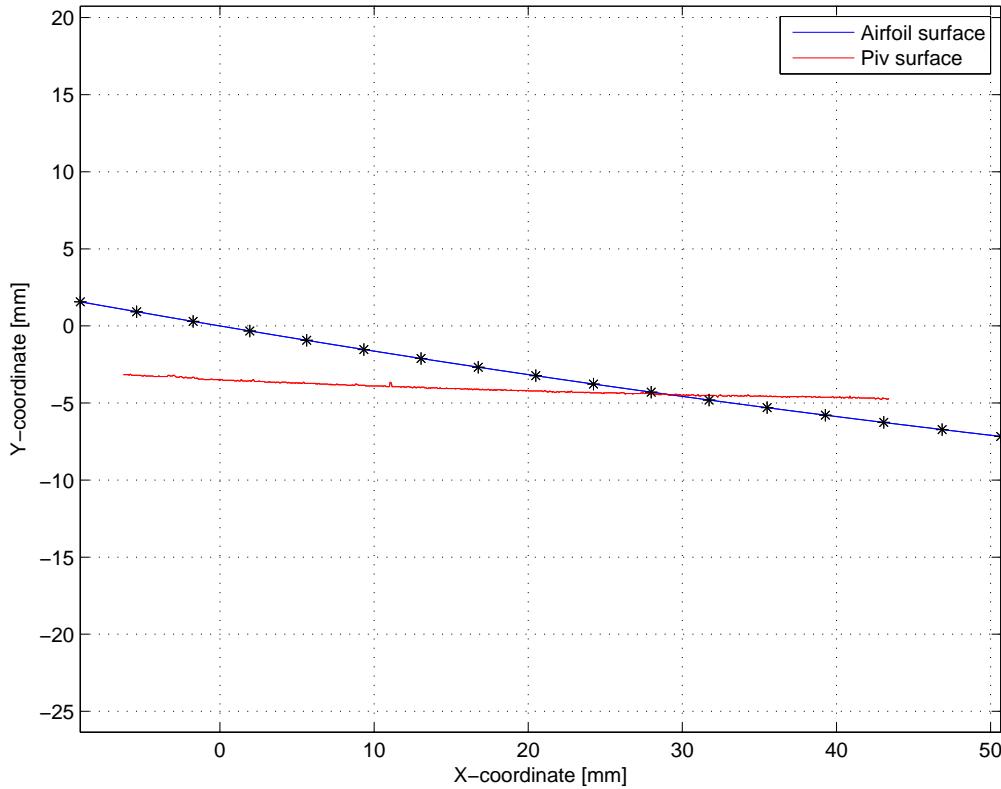


Figure 7.3: Airfoil surface as found through experiment (red) and airfoil coordinates.

The selection of the correct value of $\left. \frac{dU}{dy} \right|_{wall}$ is no trivial task, despite the procedure to find the wall in the previous section. The outlined procedure gives a very good estimate for the true wall location, but it remains an estimate. To ensure that the lowest part of the boundary layer is not discarded, a limited amount of data points below the predicted wall height are included for every profile for the next step. A comparison is made with the value of skin friction coefficient as predicted by Xfoil and Rfoil and the shear stress coefficient over the complete profile, defined as:

$$C_\tau = \frac{\mu \frac{dU}{dy}}{\frac{1}{2} \rho U_\infty^2} \quad (7.2)$$

It is non-dimensional shear stress, as it uses the velocity gradient over the complete profile rather than just at the wall as C_f . The ratios $\frac{C_\tau}{C_{f,Rfoil}}$ and $\frac{C_\tau}{C_{f,Xfoil}}$ should be as close to 1 as possible. With the C_τ in the numerator and the denominator being a constant value, the ratios have the same trend over the profile as the shear stress itself.

An example at $x = 9$ mm for A0U10 OFF is given in Figure 7.6. The largest value within the first half millimeter of where the wall was estimated to be with the procedure explained above is selected (shown in yellow). The gradient of the C_τ of neighbouring points is calculated to determine whether or not the maximum lies in a succession of more or less constant values. If not, the second largest value is taken and the process is repeated. The average over the established constant stress region values is taken to

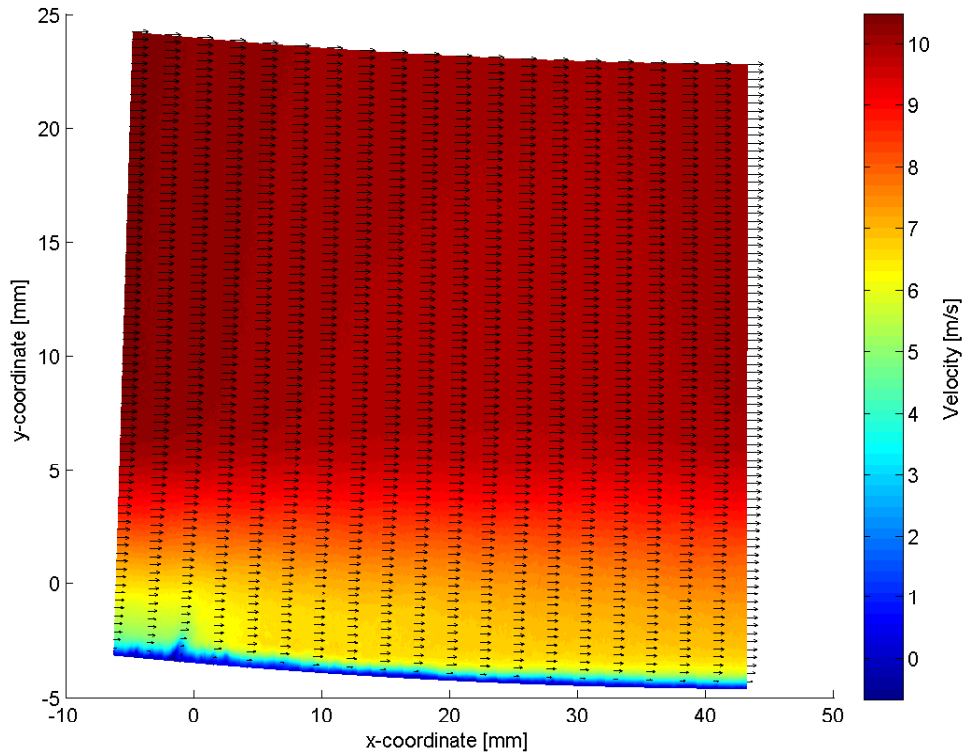


Figure 7.4: Average velocity fields of V_x and V_y in the boundary layer frame of reference (quiver resolution is reduced for illustration purposes).

be the experimentally obtained C_f . Various other strategies were considered, but the combination of the criteria set for vicinity of the wall, value close to theoretical prediction and gradient of C_τ described above was deemed to be the most trustworthy.

If no suitable constant stress layer is found of any kind, the maximum value itself is taken as value for C_f . Generally, it is also the value closest to the one found by Xfoil/Rfoil.

This is done for all x-locations and for both the actuator OFF and ON case. The percentage wise difference in skin friction coefficient between the two cases dC_f for the example case is shown in Figure 7.7. What is immediately apparent is the spikiness of the data. As will be explained in a following section, this is mostly due to the fact that either one of the datasets (for the OFF or the ON case) exhibits anomalies in the velocity profile.

The aberration in the velocity profile is persisted of course when taking the derivative to obtain the skin friction. These inconsistencies might be due to the fact of erroneous vectors at that location, experimental error or failure of the MATLAB script to correctly distill the correct shear stress value. To counteract the last element, the variation in Y between OFF and ON case is investigated, as shown in Figure 7.8. As can be seen, the location differs only very slightly, no more than a few points. The pitch between points is 0.04 mm. Where a significant aberration was encountered, the Y-location of the ON case was used for the OFF case as well, since from examination of the data it was found that generally the data quality of the former was higher than that of the latter.

To make the trend in dC_f more clear, a cubic smoothing spline was added to the data.

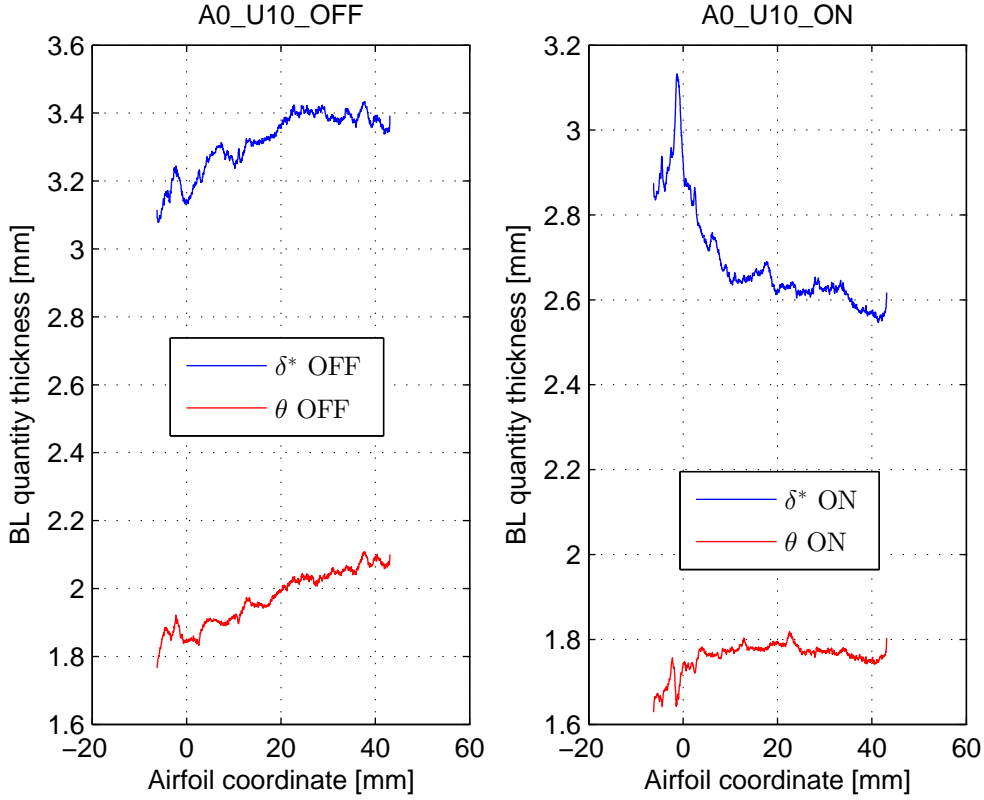


Figure 7.5: Comparison between the displacement thickness δ^* and momentum thickness θ for actuator off and on.

This spline minimizes the function:

$$P \sum_{j=1}^n |Y(:,j) - f(X(j))| + (1 - P) \int |D^2 f|^2 \quad (7.3)$$

where P is the smoothing parameter varying between 0 (least-squares straight line fit) and 1 (variational cubic spline interpolant), $D^2 f$ the second derivative of the smoothing function f . Over any given range of X-coordinates, the difference in integrated area below the experimental and smoothed data is in the order of $\mathcal{O}(10^{-4})$.

7.2 Data quality analysis

Following the procedure described in the previous section for all cases, the quality of the experimental data is investigated. To offer insight on the effect the DBD plasma actuation has on the skin friction, both the velocity data (and thus skin friction) and boundary layer state should be well captured. An overview is given below, ranked by angle of attack setting. Characteristic velocity fields or profiles are highlighted.

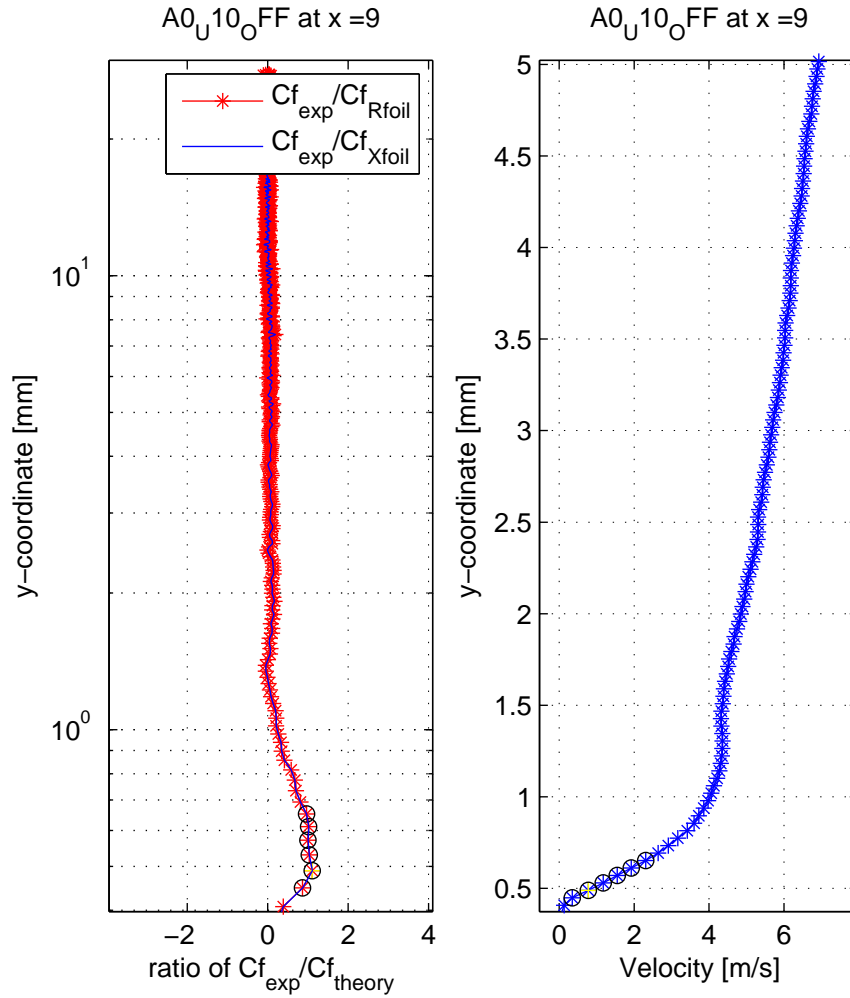


Figure 7.6: C_f -ratio of experimental over numerical X/Rfoil value (left) and velocity profile (right) for A0U10 OFF at $x = 9$ mm.

7.2.1 Angle of attack 0°

As can be seen above, although the dC_f data for A0U10 shows a lot of spikes, the trend is clear and generally no large anomalies are encountered. It is therefore accepted. For the two other cases, no obvious disparities can be found in the averaged velocity fields, coming post-processed from the PIV software. However, when comparing the obtained skin friction coefficients, no positive influence of the actuation can be found. Moreover, the actuation does not seem to have any significant positive effect on C_f , as shown in 7.9a. The ON case for both free stream velocities might not fully be resolved yet, as some graininess in the average velocity field might lead to suspect. When taking a closer look to the velocity profiles however, it can be seen that the additional velocity supplied by the momentum of the plasma force is measured in the profiles. To illustrate, the velocity profile at $x = 16.3$ for the A0U16 case is investigated closer in 7.9b. The positive effect of the actuator on the skin friction is clearly noted for this location in the A0U10 case. Care was taken with the selection of this profile to make sure it represents what

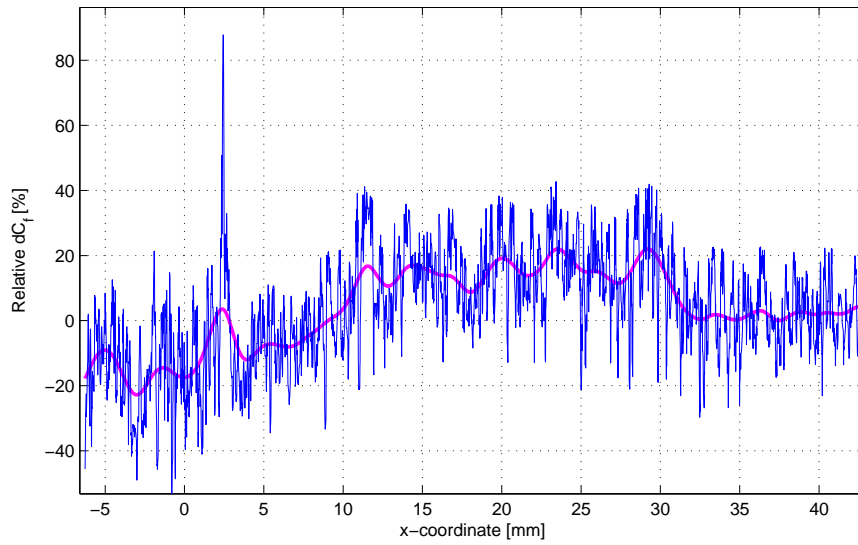


Figure 7.7: Relative variation in skin friction between plasma on and off dC_f [%] with smoothing spline for A0U10.

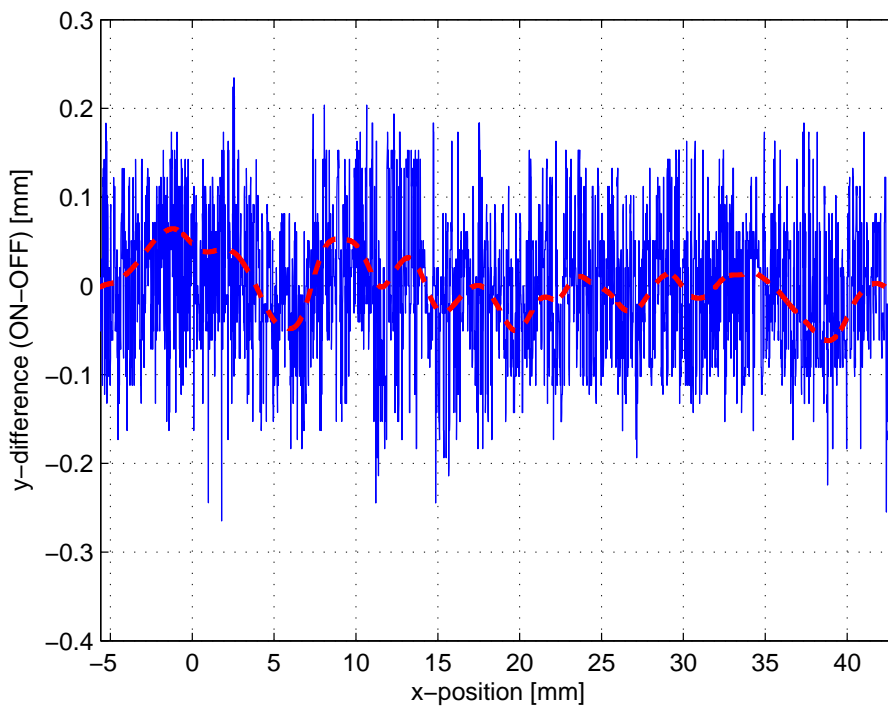


Figure 7.8: Difference in y -coordinate of the location where skin friction is extracted between plasma on and off case for A0U10.

happens for the entire flow, and is not a local outlier. The additional velocity due to the momentum addition by the plasma actuator is clearly seen between 1 mm and 4 mm

in local y -coordinate. Close to the wall however, both velocity profiles nearly coincide, which means the gradients are very similar as well, leading to almost no variation in skin friction. Analogous results are found for the A0U22 flow case. Both flows are fully attached still. One possibility is that an imperfection in the plasma field around the measurement location developed during acquisition (the A0U16 and A0U22 were recorded subsequently) which might cause this behaviour.

A calibration error is ruled out, since the same calibration is used for ON and OFF cases.

7.2.2 Angle of attack 7°

As A7U10 was one of the first cases which was measured, processing was done during the experimental campaign. It was found out that OFF case was insufficiently seeded and needed to be redone. This run was repeated at the end of the campaign. However, also the second set of data has issues regarding seeding quality, which means that no dC_f data could be extracted from this set. The other two free stream velocities A7U16 and A7U22 were accepted.

7.2.3 Angle of attack 10°

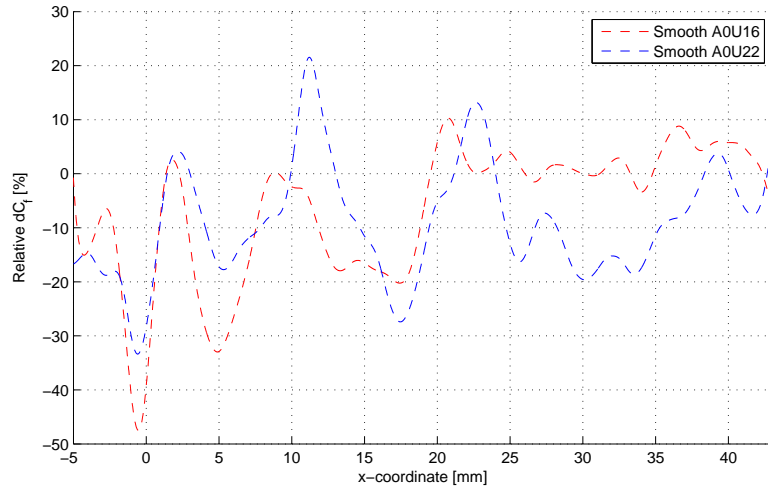
The image pairs of the A10U10 case suffer from poor particle seeding for the ON case, leading to unresolved velocity fields. The A10U16 case shows the influence of the actuation nicely, but due to starting separation, not all of the boundary layer is captured. The same holds true for the A10U22 case, where additional contamination of the lens also degrades the data quality. None of the A10 cases can therefore be retained for the modelling of the skin friction variation between plasma ON and plasma OFF.

7.2.4 Angle of attack 13°

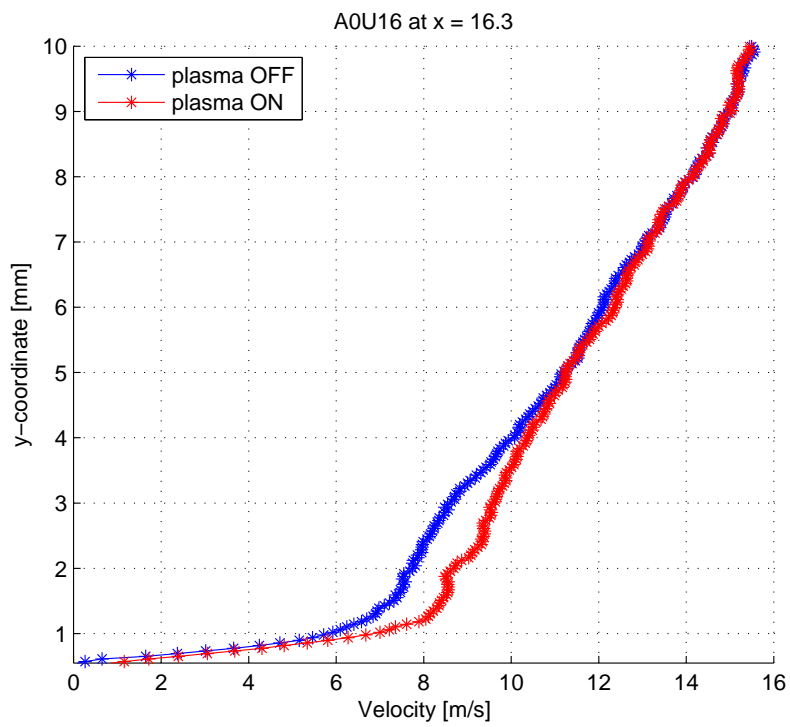
For the cases with an angle of attack of 13° , the flow has fully separated and the airfoil section experiences stall. For all velocities, the free stream is not captured at all. As the free shear layer is not seen, no conclusion can be drawn regarding the boundary layer state. Only a small part of the velocity profile is imaged, and cannot be reliably found. The shape of the separated velocity profile cannot be reliably determined as the inflection point is not captured, as shown in Figure 7.10. During the design of the experiment, the A13 case was selected as the boundary layer was predicted to have just encountered stall. However, use of a too coarse zigzag tape near the leading edge of the airfoil model might have disturbed the flow more than anticipated. Instead of merely triggering turbulence, the artificial roughness energized the boundary layer to grow outside the field of view of the camera.

7.2.5 Conclusion

An overview of the accepted datasets is shown in Table 7.1. As can be seen, only three of the 12 measured cases will be used for the modelling effort. Five cases are excluded



(a)



(b)

Figure 7.9: Average velocity fields for A0U16ON and A0U16OFF cases.

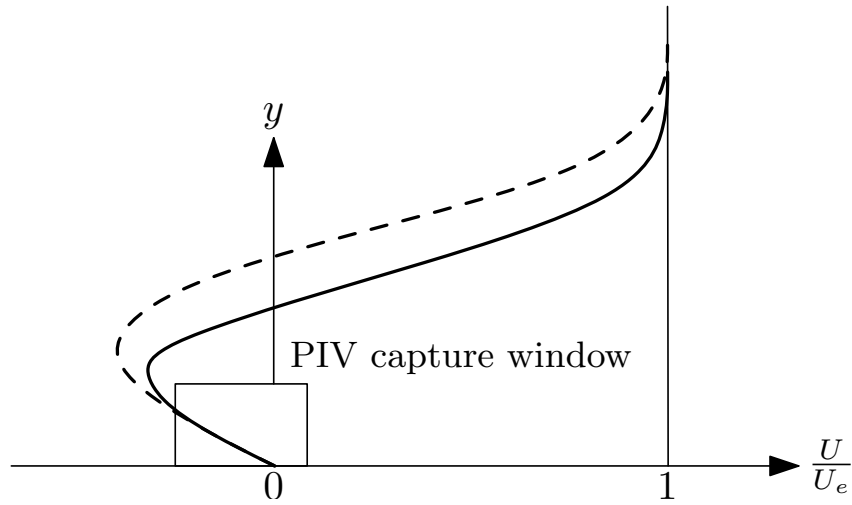


Figure 7.10: Uncertainty in the boundary layer velocity profile for A13 cases.

due to the fact that the high resolution required for the skin friction determination works prohibitive on the extent of the boundary layer that can be captured. This makes a strong case for future experiments to work with multiple camera setups. Although the exact cause of the non-result of cases A0U16 and A0U22 is uncertain, it is chosen not to include these in the modelling effort.

The results of the three accepted cases are shown and commented in the following section.

Table 7.1: Mean value of skin friction variation

	$U_\infty = 10\text{m/s}$	$U_\infty = 16\text{m/s}$	$U_\infty = 22\text{m/s}$
$\alpha = 0^\circ$	A0U10	A0U16	A0U22
$\alpha = 7^\circ$	A7U10	A7U16	A7U22
$\alpha = 10^\circ$	A10U10	A10U16	A10U22
$\alpha = 13^\circ$	A13U10	A13U16	A13U22

7.3 Discussion of selected datasets

One of the most interesting features of the variation in skin friction due to the plasma actuation is the fact that a certain lag can be observed between start of the actuation and start of the region with increased skin friction. Although a velocity difference in the profile is measured over the range where the plasma is formed, it takes some time and space before the effect is felt directly at the wall. The momentum transfer occurs higher up in the boundary layer, and does not instantly penetrate the flow closest to the wall.

What can be seen on the following figures is that ahead of the region where the plasma is formed, the presence of the plasma body force is also already felt in the skin friction coefficient (the flow is measured in the incompressible regime). With plasma actuation, besides the co-flow "push" over the actuation region, ahead of the actuation an in-rush

of flow is noted. This "indirect" effect of the actuation increases the skin friction for the ON case with respect to the OFF case.

Although these datasets will form the basis of the modelling, this does not mean they are flawless. To gain more insight in the measurements, the largest peaks in the dC_f curves are investigated. It should be noted however that due to the way the C_f is obtained (gradients of high resolution velocity PIV data), the data is highly unlikely to be smooth and spikes to a certain extent should be accepted.

The large spike visible at $x = 2.4$ in A0U10 (Figure 7.11) is the combination of an unusually low value of C_f for the OFF case, and a C_f on the high side for the ON case.

Shifting the focus to the A7U16 case (Figure 7.12), a lot more spikes and irregular behaviour can be discerned. When checking the velocity profiles at the peaks of $x = 0.4$, $x = 9.1$, $x = 13.5$, $x = 19.8$, $x = 27.8$, and the troughs at $x = 0$ and $x = 23.2$ it is found that mostly an anomaly in the OFF case data lies at the basis of the particular excess. A possible explanation as to why the OFF case is more difficult to resolve fully could be in the pulse duration of the PIV setup. The pulse duration is the time interval between the two images of the image pairs. One of the challenges observing boundary layers with PIV is the relatively large velocity variation from free stream value to zero at the wall. The pulse duration was determined for the particles in the free stream and higher parts of the boundary layer (so they would not appear as streaks). For the very low velocities near the wall however, this might be too large for reliable image capturing. More fictitious velocity vectors are fabricated during processing are produced as such. For the ON case, where higher velocities are reached near the wall, this is less of an issue.

The high peaks for A7U22 (Figure 7.13) at $x = 7.4$, $x = 23.3$ and $x = 29.1$ can each be attributed unreliable local velocity profile measurements in the set without actuation. Due to the small quantities, a slight aberration in either case can produce a significant relative anomaly.

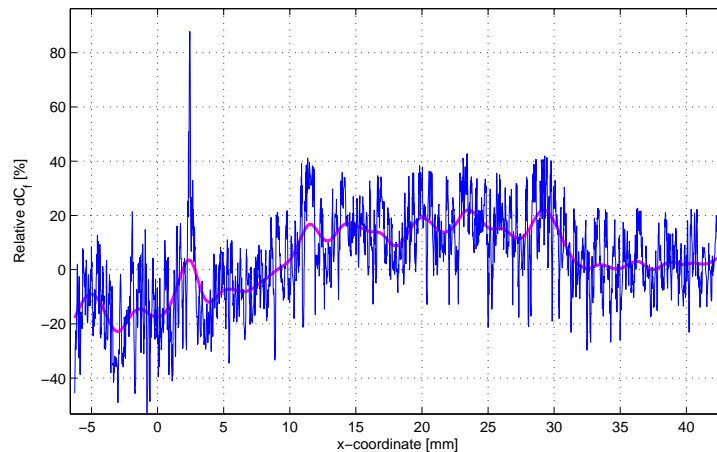


Figure 7.11: Relative variation in skin friction coefficient between plasma on and off case for A0U10

The following Part deals with the modelling of the skin friction perturbation introduced by the DBD plasma actuators from the accepted data points shown in Table 7.1. A data

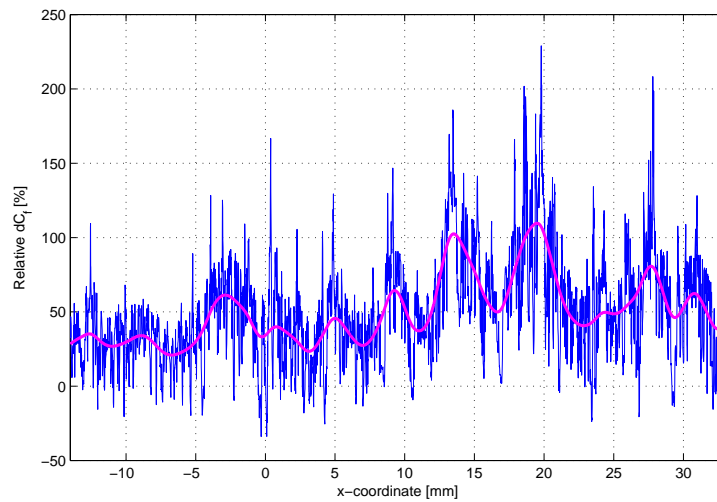


Figure 7.12: Relative variation in skin friction coefficient between plasma on and off case for A7U16

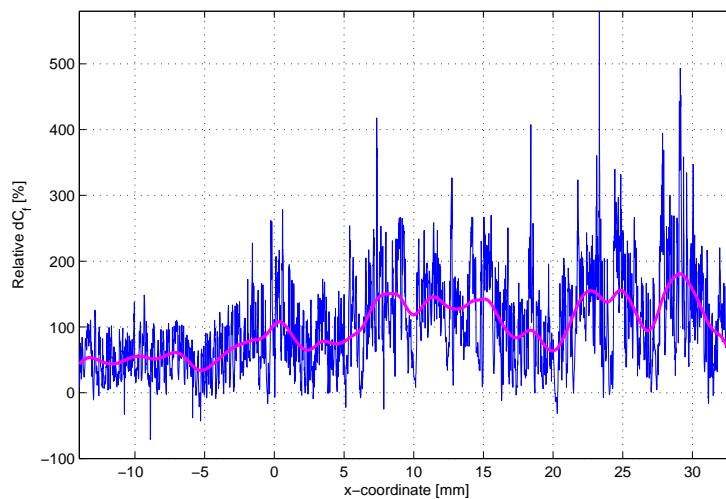


Figure 7.13: Relative variation in skin friction coefficient between plasma on and off case for A7U22

fit for the spatial distribution of this characteristic is suggested, in terms of boundary layer parameters.

Part III

Modelling and discussion

Plasma actuated skin friction coefficient variation

From the post-processed spatial variation in the skin friction coefficient of the accepted experimental cases in the previous chapter, an effort is done to provide a model. With the limited data available, the author is aware that irrefutable conclusions to generalize for all boundary layer states are precarious, though the measured points serve their purpose for this first approximate model of the phenomenon.

8.1 Characterization of experimental fit

To construct the fit to the experimentally found spatial distribution of the variation in skin friction due to actuation, several aspects are considered. First, the shape is determined and a characteristic length is established. Then, the relevant modelling parameters are determined and a check on the chosen fit is performed.

8.1.1 Shape

A semi-elliptical fit is chosen to fit the experimentally obtained dC_f over the chord. Although large fluctuations in the cases of A7 do not make this choice obvious, it is motivated through the fact that the 'cleanest' dataset A0U10 shows this behaviour relatively explicitly. The plasma body force itself is seen to act in this manner, and as such it can be put forward that the momentum addition to the boundary layer occurs semi-elliptical in the downstream direction as well. This penetrates the lowest region of the boundary layer after a certain lag and impacts the skin friction in the same manner.

8.1.2 Body force length

The length scales involved in the modelling are expressed in a relevant length scale. For this characteristic length, the length of the DBD plasma body force region is selected. It is

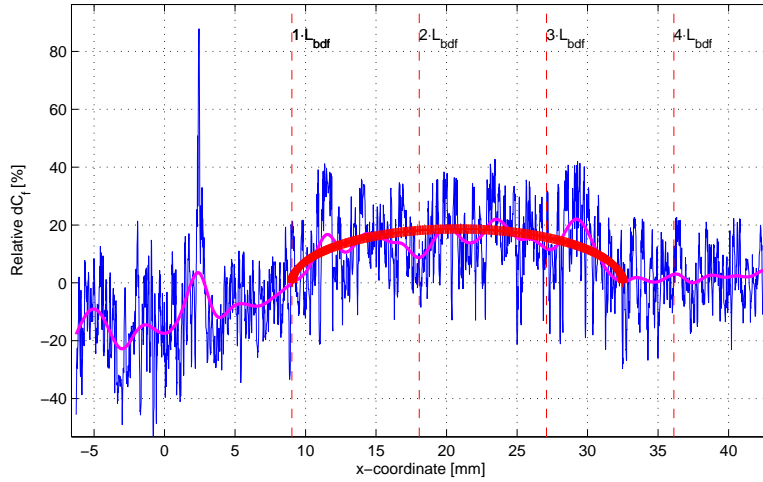


Figure 8.1: Relative variation in skin friction coefficient between plasma on and off case and proposed semi-elliptical fit for A0U10.

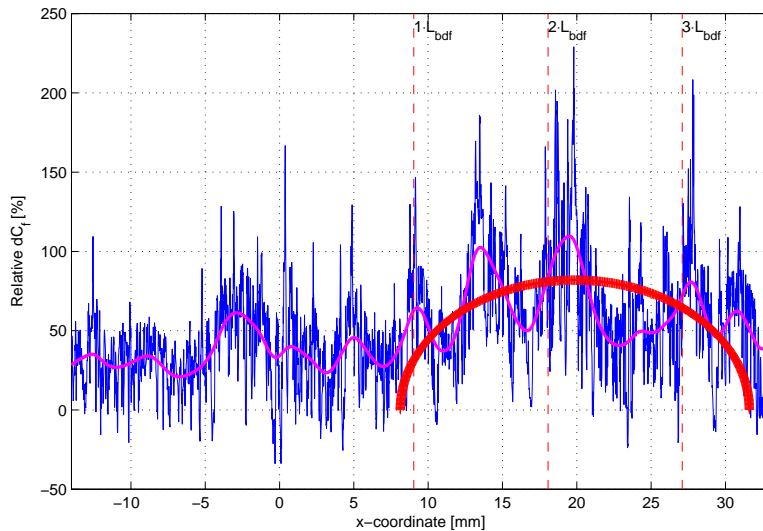


Figure 8.2: Relative variation in skin friction coefficient between plasma on and off case and proposed semi-elliptical fit for A7U16.

defined as the region where momentum is added to the flow by the plasma actuator. This is translated in the experimental data as the location where the difference in flow velocity between the *ON* and *OFF* case is increasing. It can be seen in Figure 8.4, the velocity increases from slightly before the 0 point (which was approximately the horizontal gap between the electrodes). As the covered electrode measured 25 mm, it can clearly be seen that no body force saturation the occurs. The plasma is allowed to develop freely and is not hampered due to material finite length of the covered electrode. A body force length of 9.03 mm is found. As evidenced in [8], the effect of the external incompressible flow on the plasma body force is limited, and as such a constant body force length is assumed

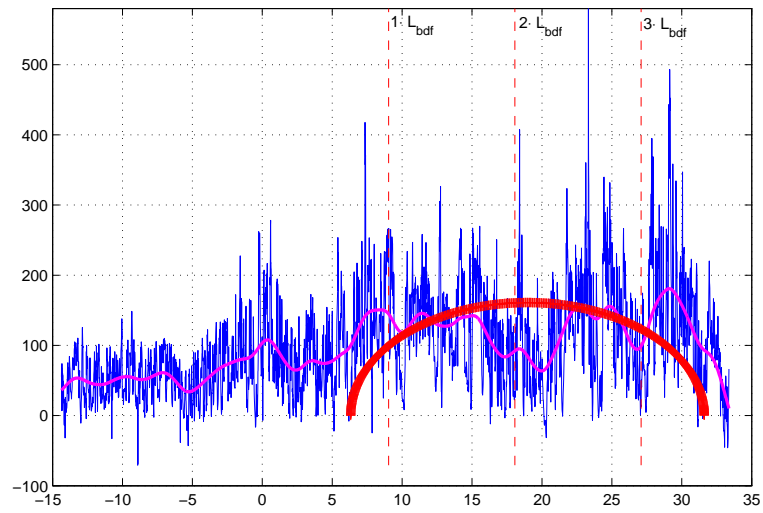


Figure 8.3: Relative variation in skin friction coefficient between plasma on and off case and proposed semi-elliptical fit for A7U22

for the three cases under consideration.

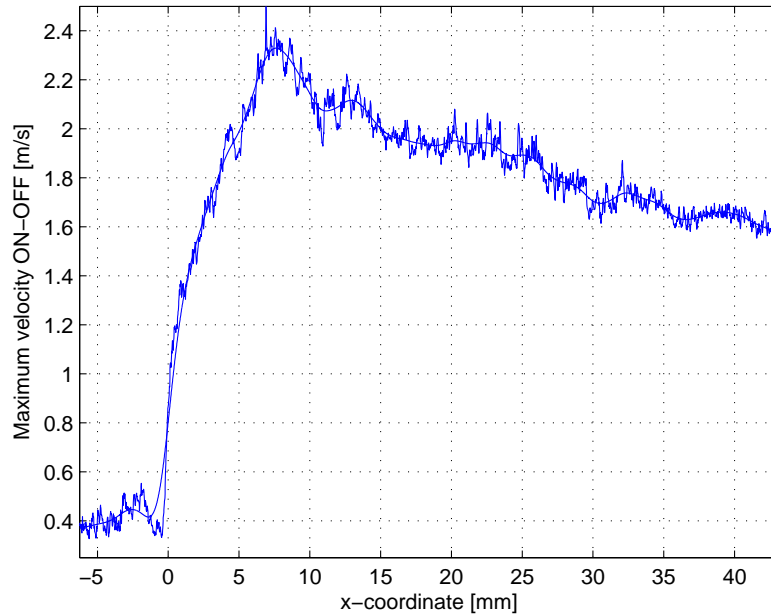


Figure 8.4: Maximum increase in velocity due to the plasma actuation at every position over the measurement domain for A0U10.

8.1.3 Modelling parameters

Determination of the size of the semi-ellipse is performed in a phenomenological way. The location where the expected increase in skin friction coefficient occurs, varies slightly for the cases. However, the length of the affected region for all the cases remains approximately constant. For the various boundary layer state developments that were captured, the region with affected skin friction coefficient is observed to be approximately 2.6 times the body force length L_{bf} . Figure 8.1 shows for instance the A0U10 case, where dC_f can clearly be seen rising after $1L_{bf}$ over this length, before dropping off towards zero, confirming the variation of dC_f ends there. More experimental data downstream should be known for A7U16 and A7U22 cases to be as conclusive. However, the values of dC_f at the end of the semi-ellipse match those at the starting point. Since the body force length is assumed invariant, it is opted to also treat the length of the region where it influences skin friction as constant. The cases of high angle of attack, where the region has moved upstream considerably, show that even for actuation in separated flows, this value is a reasonable approximation. With the limited amount of data points, this seems like a good candidate to keep constant, in order to reduce the amount of unknowns in the modelling effort.

With the length of the dC_f -affected region fixed, the starting point of the semi-ellipse is slightly moved, in order to provide the best capture of the data. This is accepted, as ultimately the resulting value for dC_f given by the model is more important than rigorous geometrical modelling. The coordinates of the semi-ellipse are given by the parametric equations, where a and b are the horizontal (longitudinal) and vertical (normal) semi-major axes respectively. As the longitudinal semi-major axis a is previously determined to be 1.3 times the body force length, the only variable left to define is the normal coordinate b . Use is made of the area of a semi-ellipse $\frac{1}{2}\pi ab$. The integration under the smoothed curve of dC_f was used to establish the (non-physical) area (in [% dC_f mm]) from which the semi-major axis b is derived as $b = \frac{2 \text{Area}}{\pi a}$. The mean dC_f was calculated for the semi-elliptical model, and compared with the one obtained from the smoothed curve and experimental data over the same range of $[x_{centerpoint} - a : x_{centerpoint} + a]$. The results can be seen in Table 8.1. The modelled dC_f values approximate the experimental ones well, which is the main objective of the effort. The mean dC_f was calculated along:

$$\text{mean } dC_f = \frac{1}{2a} \int_{x_{centerpoint}-a}^{x_{centerpoint}+a} dC_f dx \quad (8.1)$$

Table 8.1: Mean value of skin friction variation

	b [%]	mean dC_f model [%]	mean dC_f smooth [%]	mean dC_f experimental [%]
A0U10	17.36	13.64	13.63	13.69
A7U16	81.92	64.34	64.33	64.48
A7U22	161.01	126.46	126.47	126.12

Table 8.2 gives a summary of the defining characteristics for the semi-elliptical modelling of the variation in skin friction coefficient induced by the DBD plasma actuator. The

relative start point is defined as the distance from the start of the plasma region to the start of the skin friction affected region, expressed in body force lengths.

Table 8.2: Summary of characteristics of semi-ellipse models for various cases.

	a [L_{bf}]	b [% dC_f]	relative start point [L_{bf}]
A0U10	1.30	17.36	1.0
A7U16	1.30	81.92	0.9
A7U22	1.30	161.01	0.7

8.1.4 Check of spatial distribution

As an additional check to the semi-elliptical model, a further look is taken at the areas below the curves, and more in detail at the distribution per quarter. This should give an idea of the aptitude of the chosen spatial distribution. For the purpose of this analysis, the area from the centerpoint of the ellipse to half of the semi-major axis $\frac{a}{2}$ is termed L_1 and R_1 for the left and right side, and the outer quarter, from $\frac{a}{2}$ to a is L_2 and R_2 . A visual representation is given in Figure 8.5. A comparison between the experimental and theoretical values is made. This is done for both halves of the ellipse. From theory, it is derived that:

$$L_1 = R_1 = \int_0^{a/2} = (3\sqrt{3} + 2\pi) \frac{ab}{24}$$

$$L_2 = R_2 = \int_{a/2}^a = \left(\frac{\pi}{6} - \frac{\sqrt{3}}{8} \right) ab \quad \text{with} \quad \frac{L_1}{L_2} = \frac{R_1}{R_2} \approx 1.55$$

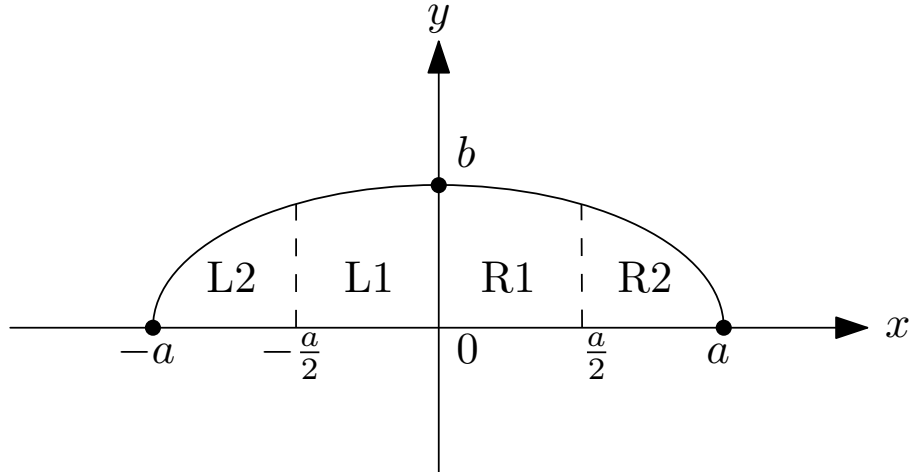
The results for the three cases are given in Table 8.4. For the case of A0U10 and the left half of A7U16, a reasonable match is obtained. A large fluctuation in the dC_f for A7U16 and a dip around the centerpoint of the semi-ellipse for the A7U22 case decreases the area ratios below 1. However, as the results of the analysis for the 'cleanest case' of A0U10 are encouraging, the semi-elliptical representation is kept, along with the arguments stated above.

Table 8.3: Check on semi-elliptical fit for modelling dC_f in space.

	$L_1 + L_2$ [% dC_f mm]	$\left(\frac{L_1}{L_2} \right)_{model}$	$\left(\frac{L_1}{L_2} \right)_{smooth}$	$\left(\frac{L_1}{L_2} \right)_{experimental}$
A0U10	149.08	$\frac{104.18}{66.89} \approx 1.55$	$\frac{83.31}{65.77} \approx 1.27$	$\frac{85.96}{67.47} \approx 1.27$
A7U16	806.28	$\frac{459.97}{259.32} \approx 1.55$	$\frac{461.59}{363.57} \approx 1.27$	$\frac{467.57}{365.53} \approx 1.28$
A7U22	1583.01	$\frac{973.61}{625.10} \approx 1.55$	$\frac{725.92}{857.06} \approx 0.85$	$\frac{744.81}{855.33} \approx 0.87$

Table 8.4: Check on semi-elliptical fit for modelling dC_f in space.

	$R_1 + R_2 [\%dC_f mm]$	$\left(\frac{R_1}{R_2}\right)_{model}$	$\left(\frac{R_1}{R_2}\right)_{smooth}$	$\left(\frac{R_1}{R_2}\right)_{experimental}$
A0U10	171.07	$\frac{104.18}{66.89} \approx 1.55$	$\frac{98.61}{72.46} \approx 1.36$	$\frac{96.4887}{71.7904} \approx 1.34$
A7U16	700.04	$\frac{459.97}{259.32} \approx 1.55$	$\frac{326.53}{358.89} \approx 0.91$	$\frac{313.52}{367.46} \approx 0.85$
A7U22	1614.54	$\frac{973.61}{625.10} \approx 1.55$	$\frac{757.23}{857.23} \approx 0.88$	$\frac{751.87}{837.11} \approx 0.90$

**Figure 8.5:** Division of semi-ellipse in quarters used as check on the spatial distribution data-fit.

8.2 Trends for H , Re_θ and t_θ^p

The trends with respect to the parameters which characterize the boundary layer condition are investigated next. For shape parameter H , momentum scaled Reynolds number and momentum scaled plasma thickness t_θ^p , the tendency is shown for semi-major axis b is shown in Figure 8.7, for mean value of dC_f over the ellipse region in Figure 8.8 and the starting location of the ellipse in Figure 8.9. The same parameters as for that other plasma specific closure, the C_{EI} are chosen. The point of view of the flow is selected. The variations in skin friction are seen as an increase with respect to the corresponding non-actuated flows.

The course of the points is very similar for the measured H and Re_θ values. When plotting the shape factor versus the Re_θ , as shown in Figure 8.10, it becomes clear that the measured boundary layer flows exhibit approximately linear variation in H and Re_θ explaining the similar profile of b , dC_f and semi-ellipse starting point. The values of Re_θ do not differ very much between the actuator ON and OFF case. The variation in shape factor is much more significant. Although plasma actuators are devices adding momentum to the flow, the largest change is felt in the displacement thickness, rather than momentum thickness. The relative change over span is shown in Figure 8.6 for case A0U10, but the trend is the same for all cases. The parameters under investigation here are therefore not expected to be directly dependent on the Re_θ in a way that the dependency on Re_θ can be discerned from the limited data on the trend plots.

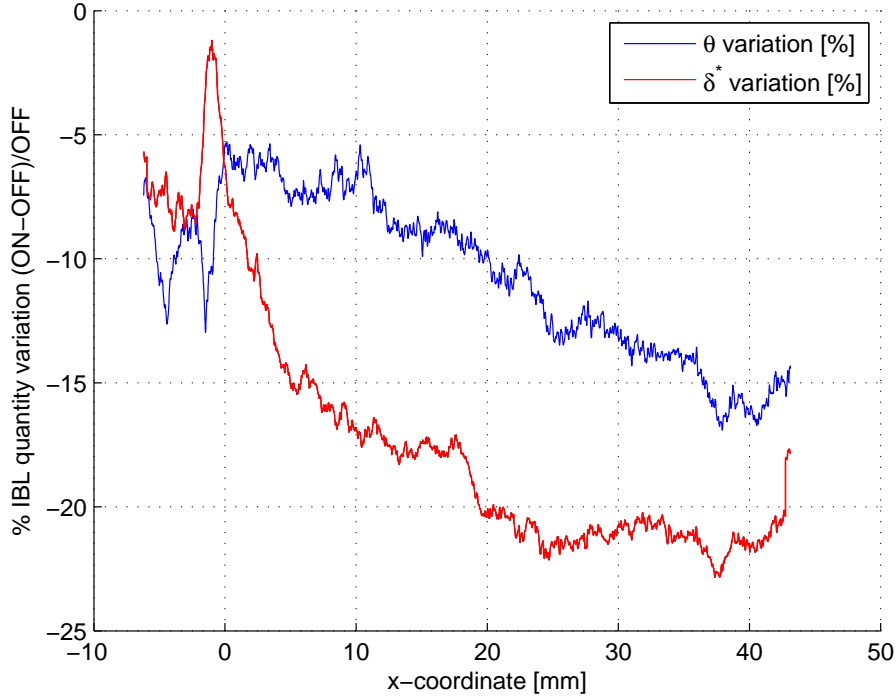


Figure 8.6: Relative variation in the momentum and displacement thickness between the plasma ON and OFF case for A0U10.

Since the thickness of the plasma body force field is assumed independent of the external flow, the quantity t_θ^p is a measure of the inverse of θ . The momentum thickness is approximately equal for A7U16 and A7U22, yielding two data points for almost the same value of t_θ^p .

From literature [24] it is found that full separation is encountered around $H \approx 3.4$ for turbulent boundary layer with the Re_θ values of the investigated flow. Since skin friction is zero in the non-actuated case, the percentage dC_f will tend to infinity first. Actuation reattaches the flow and the skin friction coefficient there will have a finite value. Beyond this value of H , the plasma actuation keeps the flow attached until the momentum added to the flow by the plasma is insufficient to prevent full separation. An experimental point in this region is required for appropriate modelling. The flow cases where separation was present in the actuator off case all still had a small region of attached flow near the wall. As the exact integral boundary layer quantities could not be recovered, the points are not added to the figures in this section. The cases of A13 are however investigated in the next section.

8.3 A13 Cases: Asymptotic value analysis for large H

Due to the fact that the boundary layer is not fully captured, the corresponding boundary layer state of the A13 cases cannot be retrieved exactly. It is therefore not possible to

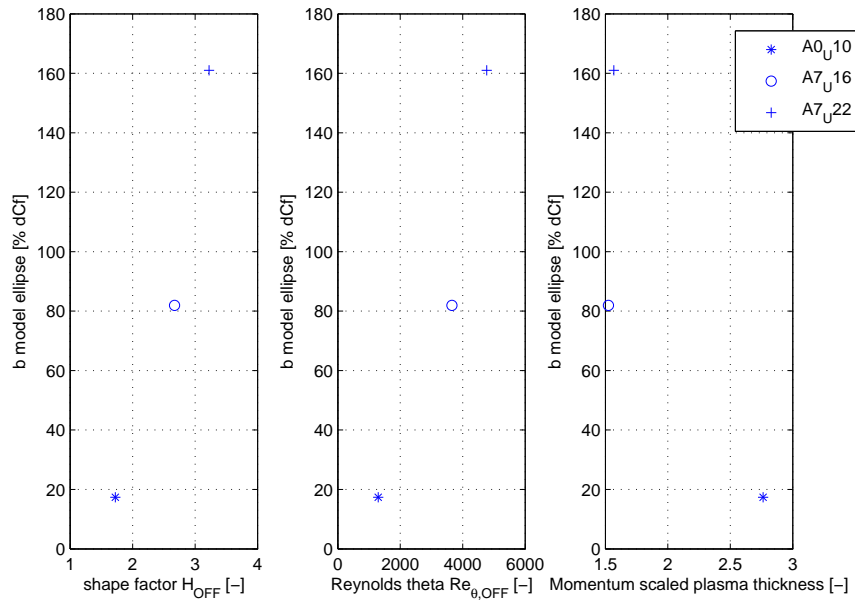


Figure 8.7: Trend for semi-major axis b over H , Re_{θ} and t_{θ}^p

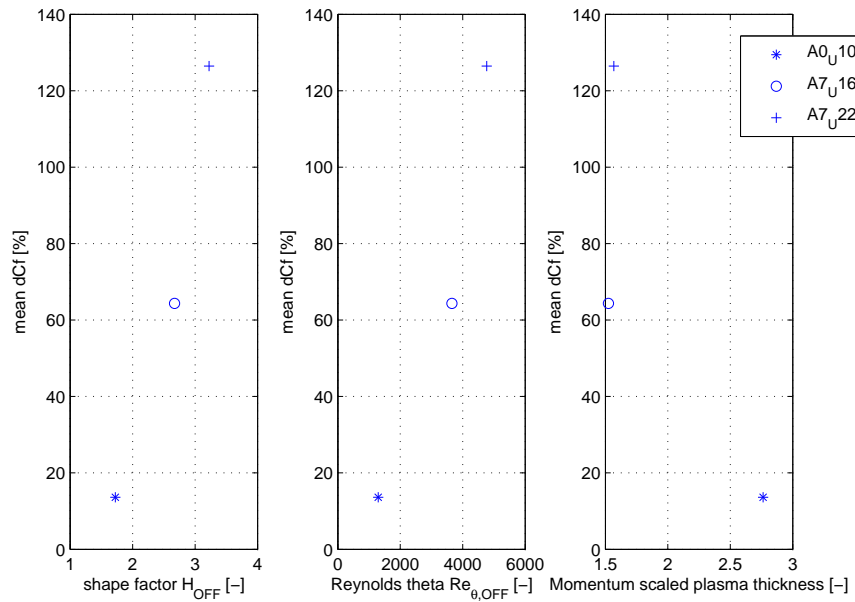


Figure 8.8: Trend for mean dCf in percent over H , Re_{θ} and t_{θ}^p

locate the data points in the curves above, though these cases can still provide valuable insight in the flow. The non-actuated flow is separated and the plasma reattaches the

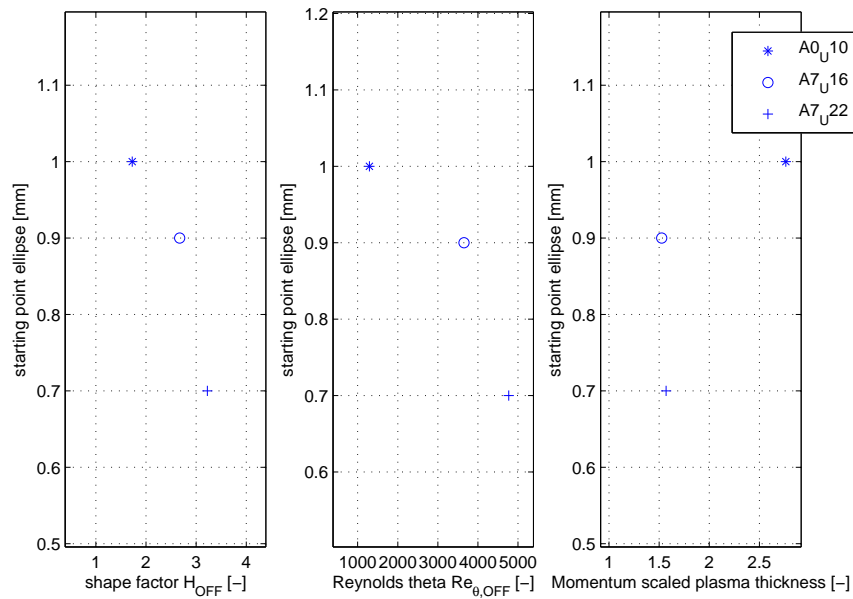


Figure 8.9: Trend for starting point of the ellipse over H , Re_{θ} and t_{θ}^p

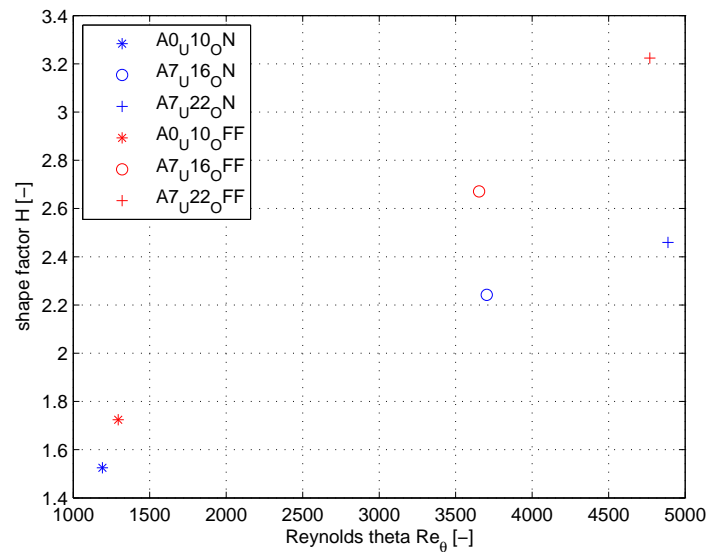


Figure 8.10: Shape factor H versus momentum scaled Reynolds number Re_{θ} for accepted experimental data sets.

flow locally, with a free shear layer above. Looking at the skin friction coefficient over the PIV capture window, it can be seen that the asymptotic value of $-2.1 \cdot 10^{-4}$ predicted by the Swafford velocity profile is approximated reasonably well. The values are tabulated in Table 8.5. It should also be kept in mind that the Swafford profile is also an approximation

itself. Even when the flow is reattached, the semi-elliptical distribution of dC_f can be seen as per Figure 8.11. The variation in dC_f is also almost constant over the three cases. Starting location has moved upstream, to even ahead of the region of actuation. The shape of spatial distribution of dC_f is however relatively retained.

Table 8.5: Skin friction coefficients of the A13 OFF cases

	A13U10 OFF	A16U10 OFF	A13U22 OFF
Skin friction coefficient C_f [-]	$-2.0342 \cdot 10^{-4}$	$-2.8858 \cdot 10^{-4}$	$-2.0412 \cdot 10^{-4}$

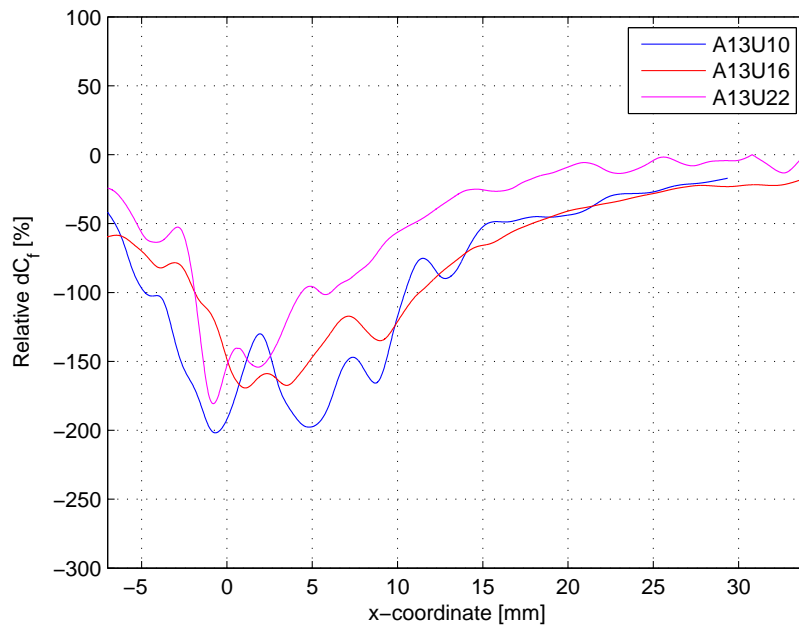


Figure 8.11: Smoothed relative skin friction coefficient variations for the A13 cases.

Towards numerical implementation

This chapter presents the steps that have been taken towards introducing the semi-elliptical model of skin friction perturbation due to the DBD plasma body force into a numerical integral boundary layer solver. The implementation of the model in the current form serves as a first step to get an idea of the effect a modified skin friction relation has on the flow computation. It is by no means a rigorous proposal for the modified closure relation which is required to accurately represent the actuation, and should not be interpreted as such. A much more extensive experimental database would be required for this.

The MATLAB solver courtesy of Gael de Oliveira (TU Delft) was used. Eventually, an improved version of the model could be translated to Rfoil to be used for the design of airfoils dedicated to DBD plasma actuation. First, the baseline solver will be explained. After discussing the adopted modifications, the outcome of the preliminary method is shown.

9.1 Matlab integral boundary layer solver

The MATLAB solver is based on the Integral Boundary Layer formulation as presented in Chapter 3, supplemented with the treatment of the plasma terms elaborated in Chapter 4. The shear lag equation describing the influence of the turbulence history on the dissipation coefficient is added to the momentum and kinetic energy shape equation. They are repeated in Equation 9.1. It should be noted that the compressibility component for the plasma terms is neglected, while it has been added to the pressure gradient terms. This set of three ordinary differential equations is also the one used by Xfoil or Rfoil (minus the plasma-specific terms of course). The terms $\frac{\partial u}{\partial x}$ and M are inputs to the system leaving the set $\{\theta, H^*, C_\tau\}$ as the unknowns.

$$\begin{aligned}
\frac{\partial \theta}{\partial x} &= \frac{C_f}{2} - (H + 2 - M^2) \frac{\theta}{u_e} \frac{\partial u_e}{\partial x} + \frac{C_{FM}}{2u_e^2} \\
\frac{\partial H^*}{\partial x} &= \frac{2C_D}{\theta} - \frac{H^*}{\theta} \frac{C_f}{2} + \left(\frac{2H^{**}}{H^*} H - 1 \right) \frac{H^*}{u_e} \frac{\partial u_e}{\partial x} + \frac{1}{\theta} \left(H^* \frac{C_{FM}}{2u_e^2} - \frac{C_{FE}}{u_e^3} \right) \\
\frac{\partial C_\tau}{\partial \xi} &= \frac{C_\tau K_C}{\delta} \left(C_{\tau EQ}^{1/2} - C_\tau^{1/2} \right)
\end{aligned} \tag{9.1}$$

In order to successfully compute the RHS of the above system of equations, additional closure relations are needed. The closure relations are algebraic relations between intermediate variables and the unknowns. There are relations for various shape factor parameters (kinematic H_k , energy H^* , density H^{**} and Head's H_1), the skin friction coefficient (C_f) and slip speed (u_s), and composite closure relations for the dissipation term ($\frac{2C_D}{H^*}$) and equilibrium shear stress coefficient (C_τ^{EQ}).

All these closures need either $\{\theta, H, C_\tau\}$ or $\{\theta, \delta^*, C_\tau\}$ as input to be solved. The three ODE unknowns are $\{\theta, H^*, C_\tau\}$. Inverting the closure relation for $H^* = f(H, Re_\theta, M)$ might give the required input terms, but it is precarious because the function is not monotonous and strenuous to invert.

An explicit solver will be used, and the problem will be reformulated in the form $\frac{\partial y}{\partial \xi} = f(y, \xi)$. MATLAB has a wide range of built-in explicit ode-solvers, whilst the implicit solvers are not as advanced. While recasting the system into the direct problem for explicit solution, the system is rewritten to use the set of $\{\theta, H, C_\tau\}$ as unknowns.

Instead of inverting the closure relation $H^* = f(H, Re_\theta, M)$, the derivative is taken. This is also done for the Re_θ and H_k in the same way.

$$H^* = f(H_k, Re_\theta, M) \quad \rightarrow \quad dH^* = \frac{\partial H^*}{\partial H_k} dH_k + \frac{\partial H^*}{\partial Re_\theta} dRe_\theta + \frac{\partial H^*}{\partial M} dM \tag{9.2}$$

$$Re_\theta = \frac{U_e \theta}{\nu_e} \quad \rightarrow \quad dRe_\theta = \left(\frac{U_e}{\nu_e} \right) d\theta + \theta \frac{U_e}{\nu_e} \tag{9.3}$$

$$H_k = f(H, M) \quad \rightarrow \quad dH_k = \frac{\partial H_k}{\partial H} dH + \frac{\partial H_k}{\partial M} dM \tag{9.4}$$

By feeding Equation 9.3 and Equation 9.4 into Equation 9.2 and reordering, the differential operator for dH becomes apparent.

$$dH = \frac{-\left(\frac{u_e}{\nu_e}\right) \frac{\partial H^*}{\partial Re_\theta}}{\frac{\partial H^*}{\partial H_k} \frac{\partial H_k}{\partial H}} d\theta + \frac{1}{\frac{\partial H^*}{\partial H_k} \frac{\partial H_k}{\partial H}} dH^* + \frac{-\theta \frac{\partial H^*}{\partial Re_\theta}}{\frac{\partial H^*}{\partial H_k} \frac{\partial H_k}{\partial H}} d\left(\frac{u_e}{\nu_e}\right) + \frac{-\left(\frac{\partial H^*}{\partial H_k} \frac{\partial H_k}{\partial M} + \frac{\partial H^*}{\partial M}\right)}{\frac{\partial H^*}{\partial H_k} \frac{\partial H_k}{\partial H}} dM \tag{9.5}$$

For clarity, the following auxiliary variables are defined:

$$\begin{aligned}
\lambda^\theta &= -\left(\frac{u_e}{\nu_e}\right) \frac{\partial H^*}{\partial Re_\theta}, & \lambda^{H^*} &= 1 \\
\lambda^{(u_e/\nu_e)} &= -\theta \frac{\partial H^*}{\partial Re_\theta}, & \lambda^M &= -\left(\frac{\partial H^*}{\partial H_k} \frac{\partial H_k}{\partial M} + \frac{\partial H^*}{\partial M}\right) \\
\gamma &= \frac{\partial H^*}{\partial H_k} \frac{\partial H_k}{\partial H}
\end{aligned}$$

Equation 9.5 can then be written more compactly, and dividing both sides by dx , it can be expressed in matrix form:

$$\frac{dH}{dx} = \frac{1}{\gamma} \begin{bmatrix} \lambda^\theta & \lambda^{H^*} & 0 & \lambda^{(U_e/\tau_e)} & \lambda^M \end{bmatrix} \begin{bmatrix} \frac{\partial \theta}{\partial x} \\ \frac{\partial H^*}{\partial x} \\ \frac{\partial C_\tau}{\partial x} \\ \partial \left(\frac{u_e}{\nu_e} \right) \\ \frac{\partial M}{\partial x} \end{bmatrix} \quad (9.6)$$

This paves the way for the desired system of equations with the set of unknowns to be $\{\theta, H, C_\tau\}$. The RHS of the system below is the one solved by the MATLAB solver.

$$\begin{bmatrix} \frac{\partial \theta}{\partial x} \\ \frac{\partial H^*}{\partial x} \\ \frac{\partial C_\tau}{\partial x} \end{bmatrix} = \frac{1}{\gamma} \begin{bmatrix} \gamma & 0 & 0 & 0 & 0 \\ \lambda^\theta & \lambda^{H^*} & 0 & \lambda^{(U_e/\tau_e)} & \lambda^M \\ 0 & 0 & \gamma & 0 & 0 \end{bmatrix} \begin{bmatrix} \frac{C_f}{2} - (H + 2 - M^2) \frac{\theta}{u_e} \frac{\partial u_e}{\partial x} + \frac{C_{FM}}{2u_e^2} \\ \frac{2C_D}{\theta} - \frac{H^*}{\theta} \frac{C_f}{2} + \left(\frac{2H^{**}}{H^*} H - 1 \right) \frac{H^*}{u_e} \frac{\partial u_e}{\partial x} + \frac{1}{\theta} \left(H^* \frac{C_{FM}}{2u_e^2} - \frac{C_{FE}}{u_e^3} \right) \\ \frac{C_\tau K_C}{\delta} \left(C_{\tau EQ}^{1/2} - C_\tau^{1/2} \right) \\ \partial \left(\frac{u_e}{\nu_e} \right) \\ \frac{\partial M}{\partial x} \end{bmatrix} \quad (9.7)$$

9.2 Modifications to the solver

The addition of the semi-elliptical skin friction perturbation is done to the model described above. Besides the geometrical region where skin friction is affected, also the value of the disturbance needs to be determined. Both are elaborated upon below. After that, the need for an additional iteration is explained.

9.2.1 Longitudinal skin friction affected region coordinate

In the same vein as what is done for the DBD plasma body force region, a weighting function for the offset in skin friction is set up:

$$w_{dC_f}^x = \begin{cases} \frac{\pi}{2} \sin \left(\frac{\pi(x - (x_0 + l_{x_0, dC_f}))}{l_{dC_f}} \right) & \left(\frac{x - (x_0 + l_{x_0, dC_f})}{l_{dC_f}} \right) \in [0, 1] \\ 0 & \text{else} \end{cases} \quad (9.8)$$

where l_{x_0, dC_f} is the length between the beginning of the body force region and the start of the region where the skin friction is affected, and l_{dC_f} is the length of the latter region itself. The dimensions which are used in the implementation effort are illustrated in Figure 9.1. For the current effort, the l_{dC_f} was assumed constant and equal to 2.6 times the body force length, as mentioned before.

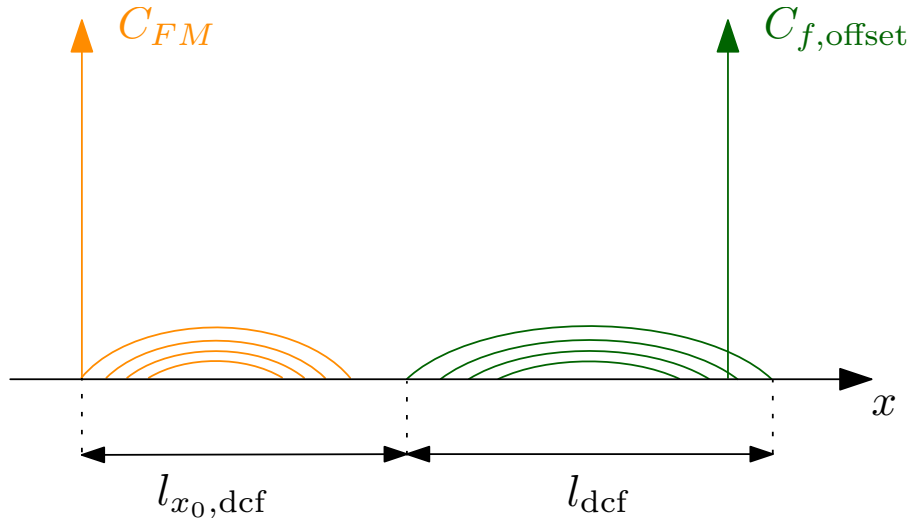


Figure 9.1: Dimensions of the weighting function of dC_f perturbed region.

9.2.2 Normal skin friction affected region coordinate

Obtaining the normal weighting function of the dC_f semi-ellipse is not as straight-forward as for the longitudinal coordinates. To arrive at a suitable value for dC_f , the point of view needs to be changed from the total flow to the local point. An investigation is performed first looking at the absolute value of the skin friction coefficient, rather than the relative disparity between actuator ON and OFF.

Figure 9.2 shows the skin friction coefficient versus the shape factor H for the three accepted data sets in the non-actuated case as '*'. The skin friction coefficient used as the experimental data point is the average over the region over which the skin friction is disturbed in the actuated case. A similar approach is used to impose the value of Re_θ . The trendlines show the $C_f(H, Re_\theta)$ according to the semi-empirical fit established by Swafford for his family of velocity profiles. Equation 9.9 shows this relation is used as the closure relation for skin friction coefficient in both the MATLAB solver and X/Rfoil.

$$C_{f,Swafford} = \frac{0.3 e^{-1.33H}}{\log_{10}(Re_\theta)^{1.74+0.31H}} + 0.00011 \left(\tanh \left(4 - \frac{H}{0.875} \right) - 1 \right) \quad (9.9)$$

Considering the uncertainty which might arise during acquisition and post-processing to experimentally determine the integral boundary layer quantities, the points match what is found through the closure relation very well. This result also reassures confidence in the approach to determine the experimental skin friction.

The same quantities for the actuated case are marked with 'o' in Figure 9.2. The Re_θ does not vary much between actuation ON or OFF, to the extent that the trend lines from the Swafford relation are nearly identical. The experimental points however have shifted left and slightly upwards with respect to the skin friction coefficients retrieved from the non-actuated cases. This result seems counter-intuitive at first, since at a given shape factor H , the actuated cases seem to have a reduced skin friction. The actuation should

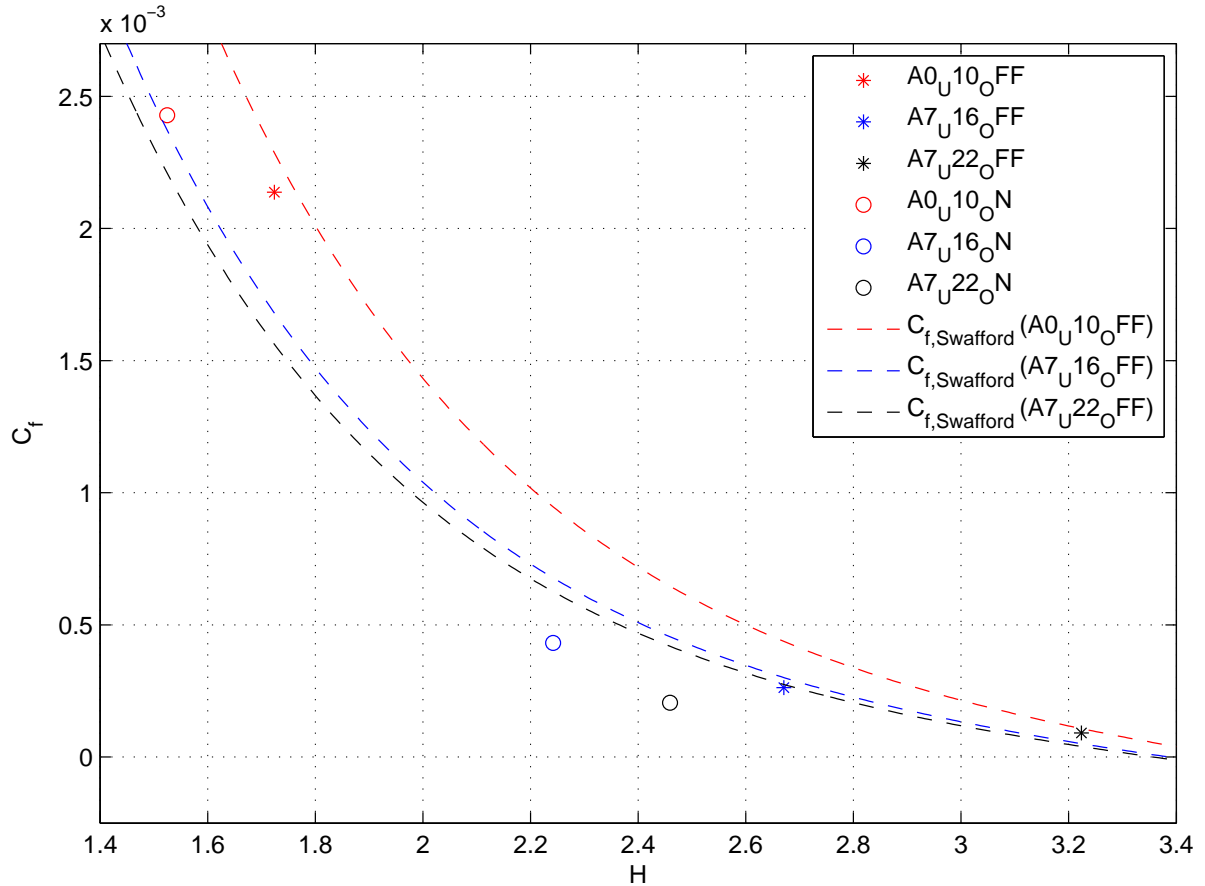


Figure 9.2: Detailed view of skin friction coefficient C_f versus shape factor H for both the actuated (\circ) and non-actuated ($*$) cases. The dotted lines show the skin friction $C_f(H, Re_\theta)$ as obtained by the X/R foil closure for each of the three flow cases.

increase skin friction as it makes the velocity profile more concave close to the wall. It is however misleading to think in these terms, as the boundary layer state is changed significantly by the actuation, and the shape factor does not longer represent the same point of boundary layer development as in the non-actuated state. As the analysis from the case of A13U22 teaches, even in deeply separated flow, the DBD plasma will attach the flow locally. A local positive value for C_f is found, although there is a large free shear layer above the thin attached flow region over the wall. The criterion that separation occurs when $C_f = 0$ no longer holds.

An elegant solution to this problem would be the use of a different velocity profile family on which the closure relations are based, for the actuated case. Amongst others, the $H^* - H$ relation, which shows the behaviour between the kinetic energy thickness and the displacement thickness, would need a new form. As three data points are obviously not sufficient to form new relations on, a more approximate method is employed to fit the actuated skin friction coefficient.

In this approximate model, the $C_f - H$ curve is shifted to the left by a factor Ψ . A larger experimental dataset could provide the basis to form a relation $\Psi(Re_\theta, C_{\phi_x^2})$, relating the

shift to the momentum scaled Reynolds number and average plasma body force coefficient. In the present case, a manual fit is done.

To assure the proper asymptotic behaviour, the shifted curve of $C_{f,plasma}$ is forced for very low and high values of H . The expressions are given in Equation 9.10. In those equations, $C_{f,Swafford}$ is the skin friction as found through Swafford's relation (Equation 9.9).

For highly attached flows, with values of shape factor less than $H_L = 1.2$, the $C_f(H, Re_\theta)$ are not only shifted left, but also downwards. At $H = 1$, the skin friction should tend to infinity. That particular case corresponds to the effective disappearance of the boundary layer, where the velocity profile resembles that of the inviscid case, with $\frac{du}{dy} \rightarrow \infty$. By also shifting the curve down, the same convergence as for the non-actuated curve is kept.

The analysis of the A13 cases show that value of actuated skin friction remains approximately constant after separation occurs for the non-actuated flow. The right bound is set at $H_R = 2.45$ which corresponds to the A7U22 case. The boundary layer could still be fully captured at these flow conditions, meaning that the shape factor could still be determined. The value of skin friction was found to be approximately equal to the one found of the separated cases of A13. In this tentative modelling approach, $C_{f,plasma}(H, Re_\theta)$ is equated with this value after $H_R = 2.45$. It is noted however that at a certain point in the flow, the added momentum by the plasma actuator might not be enough to locally re-attach the flow. This point is neglected in the current approach, since it cannot be determined with the available resources.

$$C_{f,plasma} = \begin{cases} C_{f,Swafford}(H) + [C_{f,Swafford}(H_L + \Psi) - C_{f,Swafford}(H_L)] & \text{for } H < H_L \\ C_{f,Swafford}(H + \Psi) & \text{for } H_L \leq H < H_R \\ C_{f,Swafford}(H_R + \Psi) & \text{for } H \geq H_R \end{cases} \quad (9.10)$$

The original $C_{f,S}$, composite $C_{f,plasma}$ and its separate components are shown in Figure 9.3 for Re_θ , corresponding to the A7U16 case. The experimentally obtained C_f values are replicated in the same convention as the above. The boundaries between the regimes (left, middle and right) are indicated by the vertical red lines. It shows that when the solver encounters the value of $H \approx 2.25$, a lower skin friction will be retrieved as opposed to the non-actuated case. The skin friction matching the H of the experiment is more matching for the actual boundary layer state at that point. With the current approach, an overestimation in skin friction due to the non-actuated Swafford profile is avoided.

The offset between $C_{f,plasma}$ and $C_{f,S}$ gives the measure for the semi-major axis height of the semi-ellipse representing the dC_f due to actuation (b_{dC_f}). The local value of variation in skin friction is then found by multiplying this offset with the longitudinal weighting function $w_{dC_f}^x$. This completes the formulation of the representation of the dC_f region.

An overview of the b_{dC_f} for the measured experimental cases is shown in Figure 9.4. It is mostly negative. The offset is mostly negative for moderate values of shape factors in the plasma actuated, where overestimation of the skin friction is done by the Swafford derived closure. After separation of the non-actuated flow, which occurs around 3.4 for these values of Re_θ according to Equation 9.9, the offset is positive up to the point where the complete skin friction (and not just the offset) becomes positive.

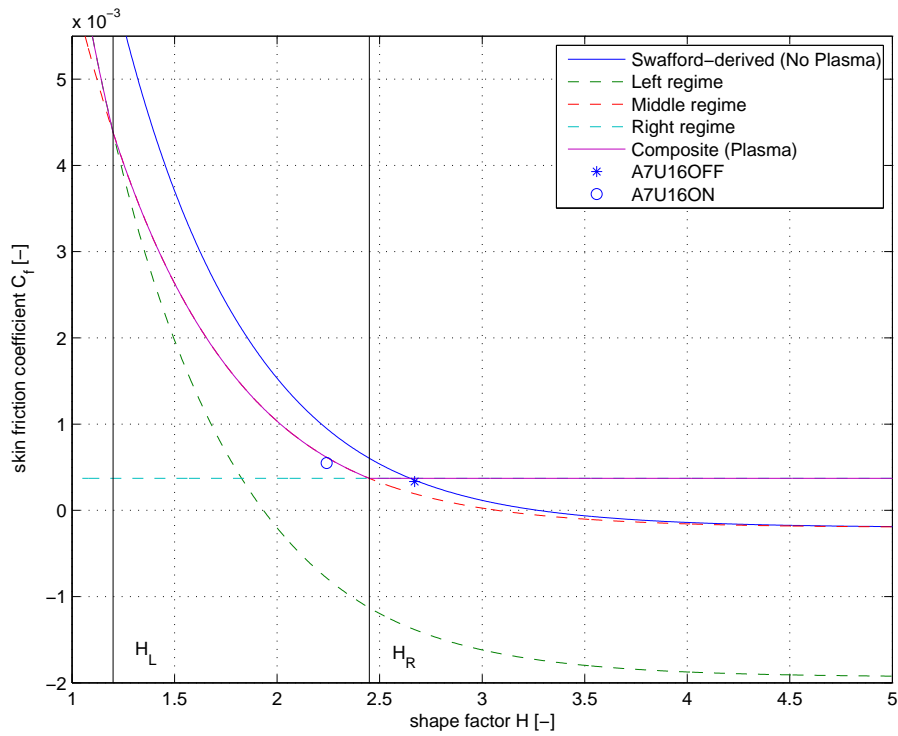


Figure 9.3: The standard Swafford-derived C_f , composite $C_{f,plasma}$ and separate left, middle and right regime components for $Re_\theta = 3653$.

9.2.3 Iteration over H

Although the region of plasma-disturbed skin friction is characterized, there is one more hurdle before the MATLAB tool can be tested. The explicit formulation integrates the equations from a certain startpoint and proceeds downstream. The solver is not able to retrieve the boundary layer state ahead of the local point, which is required for the dC_f -ellipse. The shape factor at the end of the body force region is required to determine the starting point of the affected region, where the latter might start ahead of the former.

To avoid a solution which jumps around, the b_{dC_f} value of the semi-ellipse is selected using a predetermined shape factor. As such, an initial guess for this value should be an input to the integration and updated through iterations. A relaxation factor β of 0.2 converges the shape factor to within 0.01% under the chosen maximum limit of 20 iterations. Considering the future work implementation in a code as Rfoil, this iteration can be incorporated in the viscous-inviscid coupling iteration which is inherent to the solver.

$$H^{n+1} = (1 - \beta)H^{n-1} + \beta H^n \quad (9.11)$$

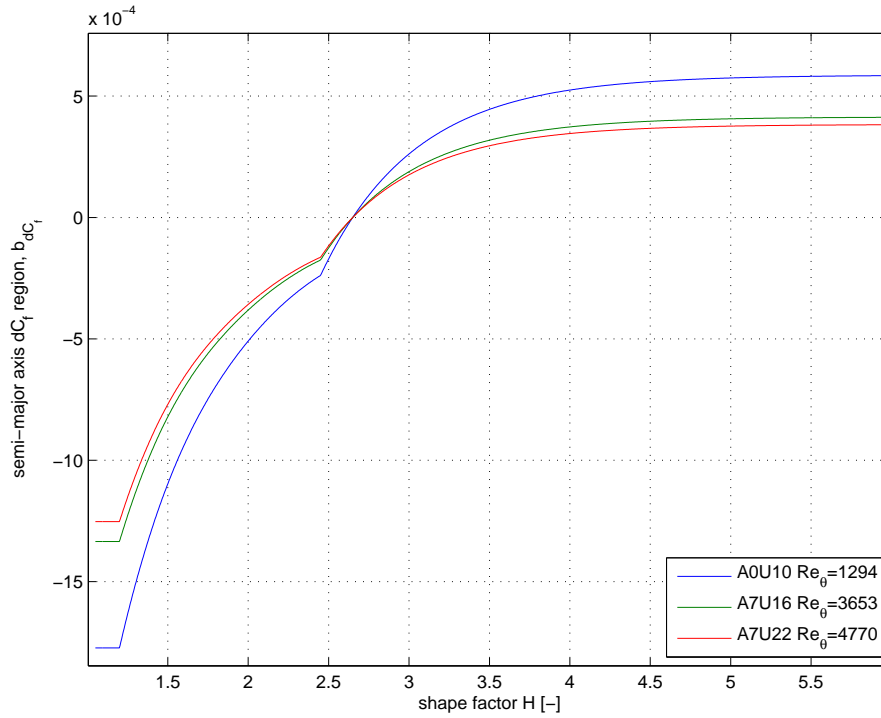


Figure 9.4: The offset between $C_{f,plasma}$ and $C_{f,S}$ or equivalently the normal coordinate of the dC_f shadow region

9.3 Outcome of data fit

As stated before, the implementation of the dC_f relation is a datafit rather than a proposal for a modified closure relation which would require a larger set of experimental data. The outcome provides heuristical insight nonetheless. A comparison is made between the baseline solver without plasma terms, with plasma terms, and with plasma terms with C_f correction.

9.3.1 Experimental case

The integral boundary layer equations are solved for the conditions of the experimental work. For the illustration below, the case of A7U16 is highlighted. The MATLAB solver is used to calculate the skin friction coefficient for the case without plasma, with plasma but no correction and with plasma with correction. These are compared with experimental data and can be seen in Figure 9.5. Actuation is applied at a location of $\frac{x}{c} = 0.65$ with a body force region length of approximately $\frac{x}{c} = 0.02$.

The computed values of C_f can be seen to keep on increasing, whereas the experimental data shows a more constant trend. The value of C_f downstream of the actuated region returns to almost equal the value before actuation. The current formulation does not modify the shear-lag equation meaning that the history of the skin friction offset are not adequately persisted in the rest of the flow downstream. Also the method of introducing the force momentum density of the body force in the IBL is cause of a disparity between

the experimental and computed value. By a making use of the Swafford velocity profiles in the C_{EI} , the actuation is felt immediately at the wall. The experimental results reported a lag between the start of the body force region and the start of the region where skin friction was affected by it. Afterwards, the plasma induced variation at the wall should be convected away to return to the non-actuated value further downstream. The added momentum does not remain in the lowest part of the boundary layer after all, though the present formulation of the solver with plasma gives that impression. To fully be able to evaluate the skin friction correction, the shear-lag equation should actually first be modified as well.

The point in the integral boundary layer quantities (Figure 9.6) where plasma is applied is clearly noted by the sudden decrease. The persisting difference between the *computed with plasma* and *computed with plasma and correction* is due to imposing the semi-elliptical dC_f offset on the first term on the RHS of the momentum equation. Although the change in quantities is very minor, the C_f -corrected formulations increases the shape factor H slightly. The displacement thickness and momentum thickness are both increased compared with respect to the non-corrected values, where θ shows the largest relative increase. The presence of the DBD plasma body force energizes the lower part of the boundary layer near the wall. This part can then also dissipate more energy at the wall increasing the momentum thickness.

The solver overestimates the integral boundary layer thicknesses and underestimates the shape factor compared to the experimental case. Making use of the $C_f = f(H, Re_\theta)$ leading to the offset between the computed and experimental values. The order of magnitude of the offset between the experimental OFF and on case is also seen between the computed OFF and computed with correction ON case, showing that the above described technique can approximate the skin friction on a local point.

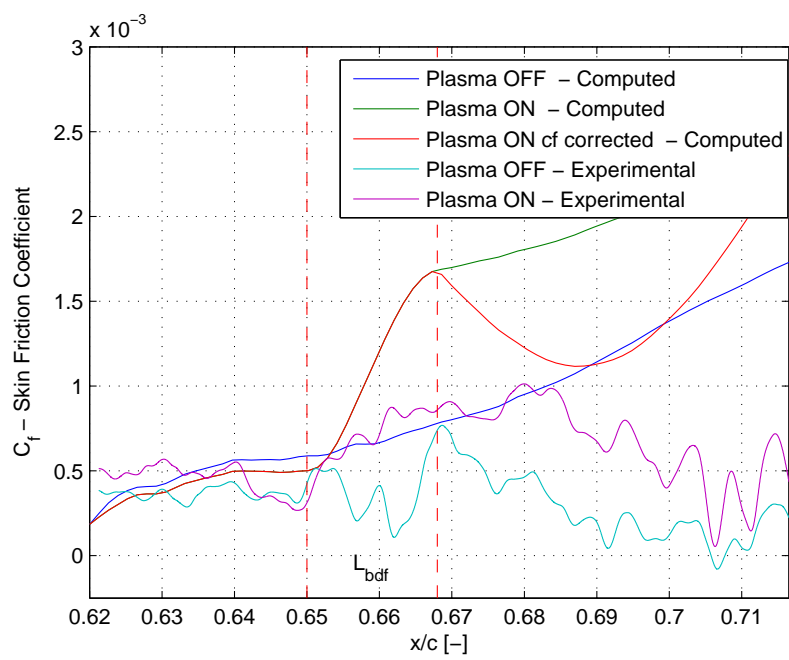


Figure 9.5: Comparison between computed and experimental skin friction coefficients for the case of A7U16.

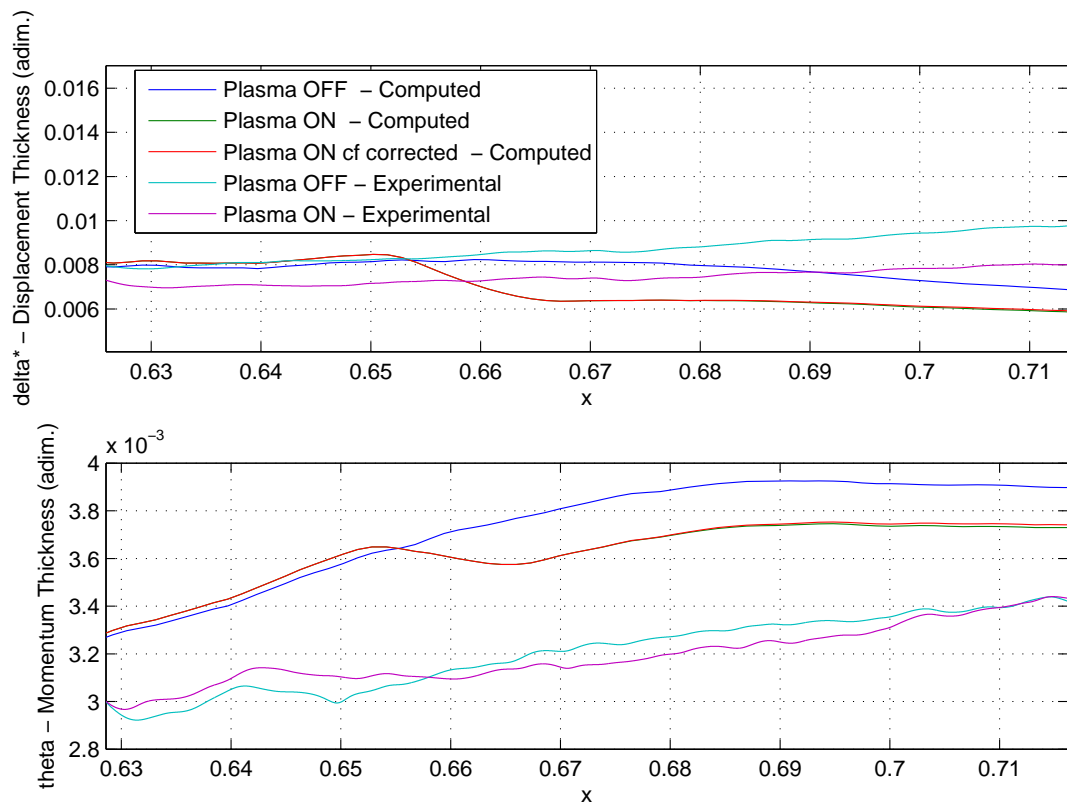


Figure 9.6: Comparison between computed and experimental displacement and momentum thickness for the case of A7U16.

Conclusions & Recommendations

The work in this thesis report frames in the larger project of implementing the effect of DBD plasma actuators in the integral boundary layer equations. This allows the effect of the actuators to be included in rapid-analysis, computationally inexpensive flow solvers such as X/Rfoil. Ultimately the present approach may enable the design of airfoils tailored for DBD plasma flow control, which allows to maximize the potential performance gain this technique has to offer. Having a better understanding of the effect of DBD plasma actuators on skin friction helps to increase the accuracy of the method.

10.1 Conclusions

An experimental campaign was designed and conducted at the open jet facility to acquire high resolution PIV of the turbulent boundary layer during various states of boundary layer development, for both actuated and non-actuated cases. The velocity fields were post-processed to extract the skin friction from the constant stress layer near the wall. To obtain the required resolution, the magnification and resolution of the camera are critical due to the inherent difficulty of the small scales involved. The variation in skin friction induced by the DBD plasma for a range of flow conditions is hence obtained. After careful scrutiny of the acquired data, the measurements set of only three of the 24 intended flow cases were deemed satisfactory. This was not enough data to propose a new closure relation to effectively describe the plasma-actuated skin friction, though still interesting insights were obtained:

- The effect of the actuation on the variation in skin friction dC_f is lagged in space compared to the actuation itself. The added momentum by the actuator needs a finite amount of time and space before it penetrates the lowest region of the boundary layer and is felt at the wall. A semi-elliptical fit is employed to model the spatial distribution of the variation in skin friction coefficient. A parallel is made with the plasma body force, for which in previous studies semi-elliptical spatial

distributions have been put forward. The chosen spatial distribution is seen to match better for flows far away from separation.

- The relative value of skin friction variation between actuator on and off case dC_f can be seen to increase rapidly from the flow case of fully attached flow to the point close to separation. Around separation, the adverse pressure gradient becomes strong enough to slow down the flow and reversal occurs. The associated values of skin friction are very low. Actuation steepens the velocity profile and keeps the flow attached for longer. This explains the asymptotic rise of the relative dC_f at shape factors around 3.4 for the measurements of the current campaign. After this point, it is found for the experimental cases of deeply separated flow that a small layer of attached flow is present underneath the free shear layer for the actuated case. The value of skin friction for the actuated cases in that flow regime seems to remain constant and positive, at a value of approximately -150% the non-actuated one. After separation, the velocity profiles of the Swafford family remain self-similar, converging to a value of $2.1 \cdot 10^{-4}$ for the skin friction. The findings for the cases with actuation suggest this type of behaviour might also hold for a plasma-actuated velocity profile, which brings the next point:
- To form adequate new closure relations, a larger experimental data base should be available than the one acquired in this project. A major step to increase accuracy of the computation of the plasma-actuated boundary layers would be to tailor the semi-empirical closures to a plasma dedicated velocity profile family. Besides the skin friction, this would also impact other closures such as the $H^* - H$ relation and shear lag equation. The set should be formed on actuated flows, and introduce new dependencies of current closures. The classical shape factor H for instance loses its conventional value to assess the boundary layer state when actuation is applied. Closures which subsequently depend on H are therefore all affected (such as the skin friction relation).
- To investigate how a modified velocity profile family (i.e. plasma-specific treatment of the closures) could be implemented in a flow solver based on integral boundary layer formulation, a curve fit of the existing C_f relation to the experimental data was done. Although the influence on the integral boundary layer quantities predictably was limited, it was found that the local skin friction could be approximated better with the proposed correction.

10.2 Recommendations

- The validity of the current modelling effort in representing the variation in skin friction due to DBD plasma actuation is hampered by the small set of experimental data it is based on. The author is fully aware of these limitations. To more precisely describe the role of the boundary layer state on extent, value and starting point of the dC_f region, additional data points for very low and very high shape factors need to be captured.
- A complication which comes with the small scale of the lowest part of the turbulent boundary layer is the trade-off to be made between magnification and field-of-view.

A trade-off between magnification and field-of-view is required when using PIV to capture the lowest part of the turbulent boundary layer. For deeply separated flows, this might entail the obligation to use multiple cameras in order to acquire the entire boundary layer.

- Validation with data from other experiments, and actuators operating at different settings should be done to prove that modelling the spatial distribution of the skin friction variation with semi-ellipses holds indeed true. This would allow the approach to be generalized more, and the relation to the plasma body force density to be better understood.
- When the proposed extended skin friction treatment is implemented in the integral boundary layer formulation based codes such as Rfoil, the effect on the overall lift and drag coefficients of the airfoil can be calculated. This is the ultimate goal of the project, as it allows for a numerical assessment of the DBD plasma actuator technique in airfoil design.

References

- [1] I. Pineda, S. Azau, J. Moccia, and J. Wilkes, “Wind in Power: 2013 European Statistics,” Tech. Rep. February, European Wind Energy Association, 2014.
- [2] C. L. Enloe, T. E. McLaughlin, R. D. Van Dyken, K. D. Kachner, E. J. Jumper, T. C. Corke, M. Post, and O. Haddad, “Mechanisms and Responses of a Dielectric Barrier Plasma Actuator: Geometric Effects,” *AIAA Journal*, vol. 42, no. 3, pp. 595–604, 2004.
- [3] M. Forte, J. Jolibois, J. Pons, E. Moreau, G. Touchard, and M. Cazalens, “Optimization of a dielectric barrier discharge actuator by stationary and non-stationary measurements of the induced flow velocity: Application to airflow control,” in *Experiments in Fluids*, vol. 43, pp. 917–928, 2007.
- [4] E. Moreau, “Airflow control by non-thermal plasma actuators,” *Journal of Physics D: Applied Physics*, vol. 40, pp. 605–636, feb 2007.
- [5] M. Kotsonis, P. Boon, and L. Veldhuis, “Plasmas for transition delay,” in *Flucome*, 10th International Conference on Fluid control, Measurements and Visualization, 2009.
- [6] R. C. Nelson, T. C. Corke, H. Othman, M. P. Patel, and S. Vasudevan, “A Smart Wind Turbine Blade Using Distributed Plasma Actuators for Improved Performance,” in *46th Aerospace Sciences Meeting*, AIAA, 2008.
- [7] F. O. Thomas, T. C. Corke, M. Iqbal, A. Kozlov, and D. Schatzman, “Optimization of Dielectric Barrier Discharge Plasma Actuators for Active Aerodynamic Flow Control,” *AIAA Journal*, vol. 47, pp. 2169–2178, sep 2009.
- [8] R. Pereira, D. Ragni, and M. Kotsonis, “The effect of external flow velocity on the momentum transfer of DBD plasma actuators,” *Journal of Applied Physics*, vol. 106, 2014.
- [9] H. O. Orlov, Dmitriy M, Thomas Apker, Chuan He and T. C. Corke, “Modeling and Experiment of Leading Edge Separation Control Using SDBD Plasma Actuators,” in *AIAA 45th Aerospace Sciences Meeting*, no. January, 2007.

- [10] M. Kotsonis, S. Ghaemi, L. Veldhuis, and F. Scarano, "Measurement of the body force field of plasma actuators," *Journal of Physics D: Applied Physics*, vol. 44, p. 045204, 2011.
- [11] I. Maden, K. Barckmann, J. Kriegseis, and S. Jakirli, "Evaluating Force Field induced by a Plasma Actuator using the Reynolds-Averaged Navier Stokes Equation," in *52nd Aerospace Sciences Meeting*, no. January, AIAA SciTech, 2014.
- [12] T. Fletcher, J. Altringham, J. Peakall, P. Wignall, and R. Dorrell, "Hydrodynamics of fossil fishes," in *Proceedings of the Royal Society B: Biological Sciences*, vol. 281 of 1804, pp. 20140703–20140703, The Royal Society Publishing, 2014.
- [13] National Programme on Technology Enhanced Learning, "Turbulent Flow: Laminar-Turbulent Transition," tech. rep., Ministry of HRD Government of India, 2012.
- [14] E. P. Veldman, "Boundary layers in fluid dynamics," tech. rep., University of Groningen, 2012.
- [15] M. Drela, *Flight Vehicle Aerodynamics*. No. May, The MIT Press, 2014.
- [16] L. L. M. Veldhuis, "Aircraft Aerodynamics Primer," tech. rep., Delft University of Technology, 2010.
- [17] G. de Oliveira and R. Pereira, "Modelling the effect of DBD plasma actuators on Boundary Layer Development (Draft Version)." 2014.
- [18] Europa, "Summaries of European Union legislation: Promotion of the use of energy from renewable sources," tech. rep., apr 2009.
- [19] T. C. Corke and M. L. Post, "Overview of Plasma Flow Control : Concepts , Optimization , and Applications," in *43rd AIAA Aerospace Sciences Meeting and Exhibit*, no. January, 2005.
- [20] S. Grundmann and C. Tropea, "Active cancellation of artificially introduced Tollmien-Schlichting waves using plasma actuators," *Experiments in Fluids*, vol. 44, no. 5, pp. 795–806, 2008.
- [21] T. N. Jukes and K. S. Choi, "Dielectric-barrier-discharge vortex generators: Characterisation and optimisation for flow separation control," *Experiments in Fluids*, vol. 52, no. 2, pp. 329–345, 2012.
- [22] M. Tanaka, K. Amemori, H. Matsuda, N. Shimura, H. Yasiu, and T. Osako, "Field Test of Plasma Aerodynamic Controlled Wind Turbine Motofumi," tech. rep., Mie University, Japan, Toshiba-cho, Fuchu-Shi, Tokyo, 2013.
- [23] M. Drela and M. B. Giles, "Viscous-inviscid analysis of transonic and low Reynolds number airfoils," *AIAA Journal*, vol. 25, no. 10, pp. 1347–1355, 1987.
- [24] R. van Rooij, "Modification of the boundary layer calculation in RFOIL for improved airfoil stall prediction," Tech. Rep. Report IW-96087R, Delft University of Technology, Institute for Wind Energy, 1996.

- [25] N. Ramos-García, J. N. Sørensen, and W. Z. Shen, “A strong viscous-inviscid interaction model for rotating airfoils,” *Wind Energy*, vol. 17, pp. 1957–1984, dec 2014.
- [26] G. de Oliveira, R. Pereira, D. Ragni, and M. Kotsonis, “Modeling DBD Plasma Actuators in Integral Boundary Layer Formulation for Application in Panel Methods,” in *46th AIAA Plasmadynamics and Lasers Conference*, (Dallas, Texas), 2015.
- [27] M. Gad-El-Hak, *Flow Control: Passive, Active, and Reactive Flow Management*. Cambridge University Press, 2006.
- [28] L. Leger, E. Moreau, G. Artana, and G. Touchard, “Influence of a DC corona discharge on the air flow along an inclined flat plate,” in *Journal of Electrostatics*, vol. 52, pp. 300–306, Institute of Physics Conference, Bristol: Institute of Physics Publishing, 2001.
- [29] A. Dialoupis, “Active Flow Control Using Plasma Actuators - Application on Wind Turbines,” Master’s thesis, Delft University of Technology, Faculty of Aerospace Engineering, aug 2014.
- [30] J. Kriegseis, A. Duchmann, C. Tropea, and S. Grundmann, “On the classification of dielectric barrier discharge plasma actuators : A comprehensive performance evaluation study On the classification of dielectric barrier discharge plasma actuators : A comprehensive performance evaluation study,” *Journal of Applied Physics*, vol. 053301, 2013.
- [31] A. P. Kuryachii, D. A. Rusyanov, V. V. Skvortsov, and S. L. Chernyshev, “Modeling the system of electrodynamic final-control elements,” *Fluid Dynamics*, vol. 46, no. 5, pp. 764–774, 2011.
- [32] Y. B. Golubovskii, V. A. Maiorov, J. Behnke, and J. F. Behnke, “Influence of interaction between charged particles and dielectric surface over a homogeneous barrier discharge in nitrogen,” *Journal of Physics D: Applied Physics*, vol. 35, no. 8, pp. 751–761, 2002.
- [33] K. P. Singh and S. Roy, “Force approximation for a plasma actuator operating in atmospheric air,” *Journal of Applied Physics*, vol. 103, 2008.
- [34] M. Kotsonis and S. Ghaemi, “Experimental and numerical characterization of a plasma actuator in continuous and pulsed actuation,” *Sensors and Actuators A: Physical*, vol. 187, pp. 84–94, 2012.
- [35] S. Kenjereš and K. Hanjalić, “On the implementation of effects of Lorentz force in turbulence closure models,” *International Journal of Heat and Fluid Flow*, vol. 21, no. 3, pp. 329–337, 2000.
- [36] K. Hall, E. Jumper, T. Corke, and T. McLaughlin, “Potential flow model for plasma actuation as a lift enhancement device,” in *43rd AIAA Aerospace Sciences Meeting and Exhibit*, vol. 43, AIAA, 2004.
- [37] A. V. Likhanskii, M. N. Shneider, S. O. MacHeret, and R. B. Miles, “Modeling of dielectric barrier discharge plasma actuator in air,” *Journal of Applied Physics*, vol. 103, 2008.

-
- [38] A. Young, *Boundary Layers*. BSP Professional Books, 1989.
- [39] M. H. Keegan, D. H. Nash, and M. M. Stack, “On erosion issues associated with the leading edge of wind turbine blades,” *Journal of Physics D: Applied Physics*, vol. 46, no. 38, p. 383001, 2013.
- [40] J. Nash, “A note on skin-friction laws for the incompressible turbulent boundary layer,” Tech. Rep. 862, Ministry of Aviation Aeronautical Research Council, 1964.
- [41] A. P. Silva-Freire, “An asymptotic solution for transpired incompressible turbulent boundary layers,” *International Journal of Heat and Mass Transfer*, vol. 31, no. , pp. 1011–1021, 1988.
- [42] G. D. Oliveira, “A novel approach to Wind Turbine Airfoil design with Boundary Layer Suction,” , Delft University of Technology, , 2011.

